A THEORETICAL AND EXPERIMENTAL STUDY OF THE INTERACTION BETWEEN A FOCUSED LASER BEAM AND A CONDUCTING CONE WITH A SPHERICAL TIP

Gengying Gao

B.Sc., Nankai University, Tianjin, China, 1983
M.S., Electronic Material Research Institute, Tianjin, China, 1987

A thesis submitted to the faculty
of the Oregon Graduate Institute of Science & Technology
in partial fulfillment of the
requirements for the degree
Doctor of Philosophy
in
Applied Physics

April, 1992

The thesis "A Theoretical and Experimental Study of the Interaction between a Focused Laser Beam and a Conducting Cone with a Spherical Cap" by Gengying Gao has been examined and approved by the following Examination Committee:

J. Fred Holmes, Advisor
Professor

Rao V. Gudimetla
Assistant Professor

Anthony Bell
Associate Professor

Reinhart Engelmann
Professor

M. Aslam K. Khalil
Professor
Atmosphere Institute, OGI

ACKNOWLEDGMENTS

I would like to express my sincere appreciation to my Thesis Research Advisor Dr. J. Fred Holmes and the other members of my Thesis Committee: Dr. Anthony Bell, Dr. Reinhart Engelmann, and Dr. M. Aslam. K. Khalil. They read and edited my dissertation carefully in theory, experiment and gave me a lot of wonderful suggestions in writing style.

Dr. J. Fred Holmes, in particular is owed a debt of gratitude for his guidance, understanding, assist and patience when I was working on my thesis, and for his vast knowledge and physical insight in science from which I have been greatly benefited. It has been proved to be the most valuable thing to my life.

I would like to thank Dr. Rao Gudimetla's advice and suggestions in mathematics. Thanks to Mr. John Hunt for his help in computer and many experimental techniques, to Mr. Jeff Schilling's great video work. I am also very thankful to those who gave me a lot of assistant and made this thesis possible: Dr. Richard DeFreez, Li Zhou, Badih Rask, Marc Felisky, Geoffery Wilson and so on.

Thanks are also due my grandfather -- A Physicist Dr. Y.Q. Gao for his teaching and training in my carrer, and my parents for their encouragement and love. The final note of grateful is sounded to my husband, Ming Li, who plays a very important role in this work. He is a constant supporter and the source of wisdom.

DEDICATION

To My Grandparents

Table of Contents

List of Figures

List of Tables

ABSTRACT

A THEORETICAL AND EXPERIMENTAL STUDY OF THE INTERACTION BETWEEN A FOCUSED LASER BEAM AND A CONDUCTING CONE WITH A SPHERICAL TIP

Gengying Gao, Ph.D.

Oregon Graduate Institute of Science and Technology, 1991

Supervising Professor: J. Fred Holmes

This dissertation is a study of the electric and magnetic fields of a laser beam focused on the tip of a perfectly conducting cone with a spherical cap. A solution of Helmholtz equation, in spherical coordinates, was developed using Hertz potentials for the boundary value problem appropriate to fitting the laser field over the spherical tipped cone. The solution involves associated Legendre functions of integer order but noninteger degree. The basis functions comprise two infinite sets, within each of which the functions are mutually orthogonal. The series for the expansion of the Hertz potentials can be differentiated term by term to yield uniformly convergent series for the field components. Using the boundary conditions of each associated Legendre function and its derivative at the surface of the conductors, the order and degree are generated.

The motivation and application of this work is concerned with the currently very interesting problem in the surface physics area, concerning laser modulation of a liquid metal ion source (LMIS). The LMIS can be modeled as a cone with a small protrusion at the tip. Since the protrusion is very small, the actual shape is probably not very important. Consequently, a spherical tip was used since its use is mathematically convenient. The results at our mathematical model allows the field distribution on the surface of the tip from which heating of the tip can be calculated as well as the electric field enhancement which maybe useful for laser modulation of the LMIS by influencing the field emission rate.

CHAPTER 1. INTRODUCTION

1.1 A Review of the Precedent Work

In the late 1950's, many scientists began to study the properties of electromagnetic waves in regions bounded by rigid and perfectly conducting surfaces which can be described in terms of a single coordinate in a spherical coordinate system[1-5]. These surfaces, represent spheres, cones, and planes or the region bounded by any combination of these. Diffraction and scattering problems in such regions may be solved by expressing the desired field solution in terms of modes (eigenfunctions) expressed in terms of the angular coordinates and modal coefficients which depend on the radial coordinate and take into account the source of the fields[6].

L. B. Felsen and N. Marcuvitz in their book " Radiation and Scattering of waves" give the detail solutions for the distribution of the electric field[7]. In particular, they investigated in detail the effect of waveguide walls whose location could be described simply in terms of the circular-cylindrical or spherical coordinate system. Included therein were the important configurations of the circular cylinder, the wedge, the sphere and the cone[1].

The interaction of a focused laser beam with a spherical particle is a topic of current research interest with application occurring in a variety of areas of study including particle size determination, optical levitation and laser modulation of liquid metal ion sources[8,9]. Previous work includes theoretical expressions for the internal and external electromagnetic fields for an arbitrary electromagnetic beam incident upon a homogeneous spherical particle[10]. Previously, Dusel, Kerker, and Cooke[11] and Green[12] *et al.* have presented internal electric field magnitude (source function) distributions for a plane electromagnetic wave incident upon a homogeneous spherical particle. But such a plane-wave assumption would be appropriate only if the sphere diameter is much less than the local beam diameter, and this is often not the situation when a focused laser beam is used for illumination. Morita[13] *et al.*, Tsai and Pogorzelski[14], Tam and Corriveiu[15], Kim and Lee[16], and Gouesbet, Greham, and Maheu[17] have all considered the problem of a fundamental Gaussian beam incident upon a homogeneous spherical particle, but these works appear primarily concerned with far-field scattering and no internal or near-surface electromagnetic field distributions are presented. However, it appears that no work has been done on the interaction of a laser beam with a cone. The electromagnetic fields that result from a focused laser beam incident upon a metal body is a function of the properties of the beam (wavelength, power, mode, beam waist diameter), the properties of the body (size, shape, complex index of refraction), and the relative focal point positioning. Our work is a theoretical development that permits the determination of the electromagnetic fields for a focused laser beam incident upon a homogeneous perfectly conducting cone with a spherical tip as a function of these parameters.

As the theoretical work went on, meanwhile, more and more people started their experimental work and paid attention to the applications of above theory. In 1960's, Sir G. Taylor [18] concluded that a balance between electrostatic stress and surface tension on a liquid surface led to the formation of a cone shape with a semi-angle of 49.3^0 . Mahoney[19] *et al.* experimentally generated ions from liquid cesium metal and Krohn and Ringo[20] found that gallium metal as a high brightness ion source was much superior than cesium and mercury in 1975. At the end of 1970's, the focused ion beam technology, inspired by the development of the field ionization source, was realized[21-27]. Through the past decade the development of the liquid metal ion source (LMIS)[28-31], the liquid alloy ion source (LAIS)[32-48] and the focused ion beam (FIB)[49-53] techniques have permeated through almost every aspect of semiconductor industry[24, 54-65], including semiconductor optical device fabrication[66-68], micromachining[69-76], integrated circuit device modification and fabrication[77-83], resist exposure[84-86], photomask repair[87], maskless ion-implantation of semiconductor dopants88-100 , ion beam assisted etching and deposition[101-113] and others.

In Figure 1.1, there is a picture of a typical LMIS configuration which was taken by a SEM. In Chapter 5, we will introduce its mechanism and show the cone-shape at the very end of the tip. Figure 1.2 shows a workstation of focused ion beam micromachining (FIBM) system. It is used for micromachining, mirrors, gratings and other miniature optical components on laser diodes. The FIBM would greatly benefit if the beam intensity could be modulated rapidly. This was the incentive for the work that follows.

1.2 Our Specific Work

The problem under consideration in this thesis is the electromagnetic interaction between a laser beam and a perfectly conducting cone with a spherical tip. In the theoretical part, formulations have been derived for the electric and magnetic fields generated near the tip of the cone by a focused laser beam. The Hertz potential method[114] was used to obtain the electromagnetic fields. The cone and spherical tip were assumed to be perfectly conducting with the tangent electric field equal to zero on the surface of the cone and tip as the boundary condition. The main purpose of the study is to determine how much the fields from the focused laser beam are enhanced near the cone tip.

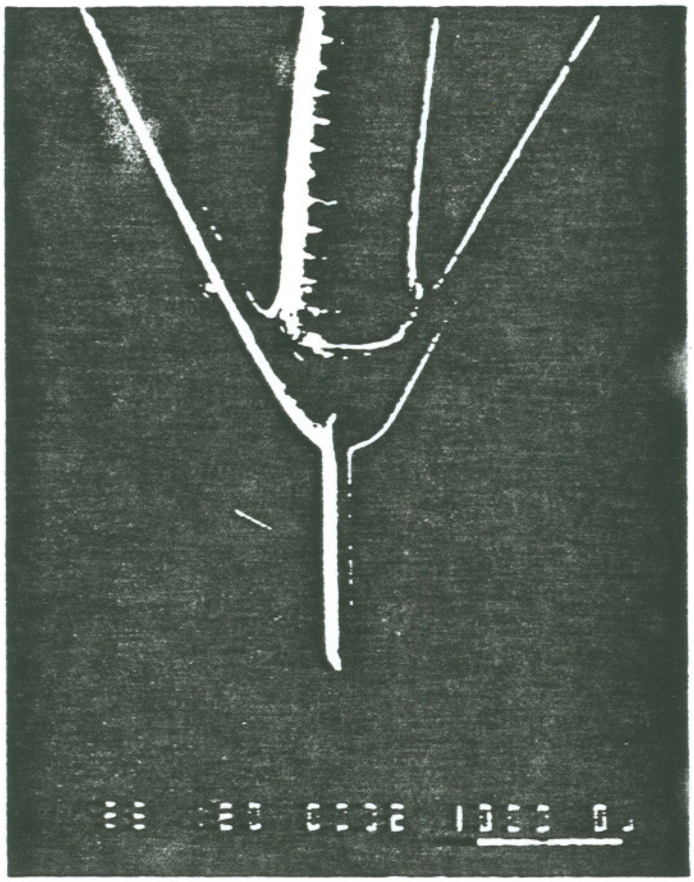

Figure 1.1 SEM micrograph of a typical Ga liquid metal ion source configuration

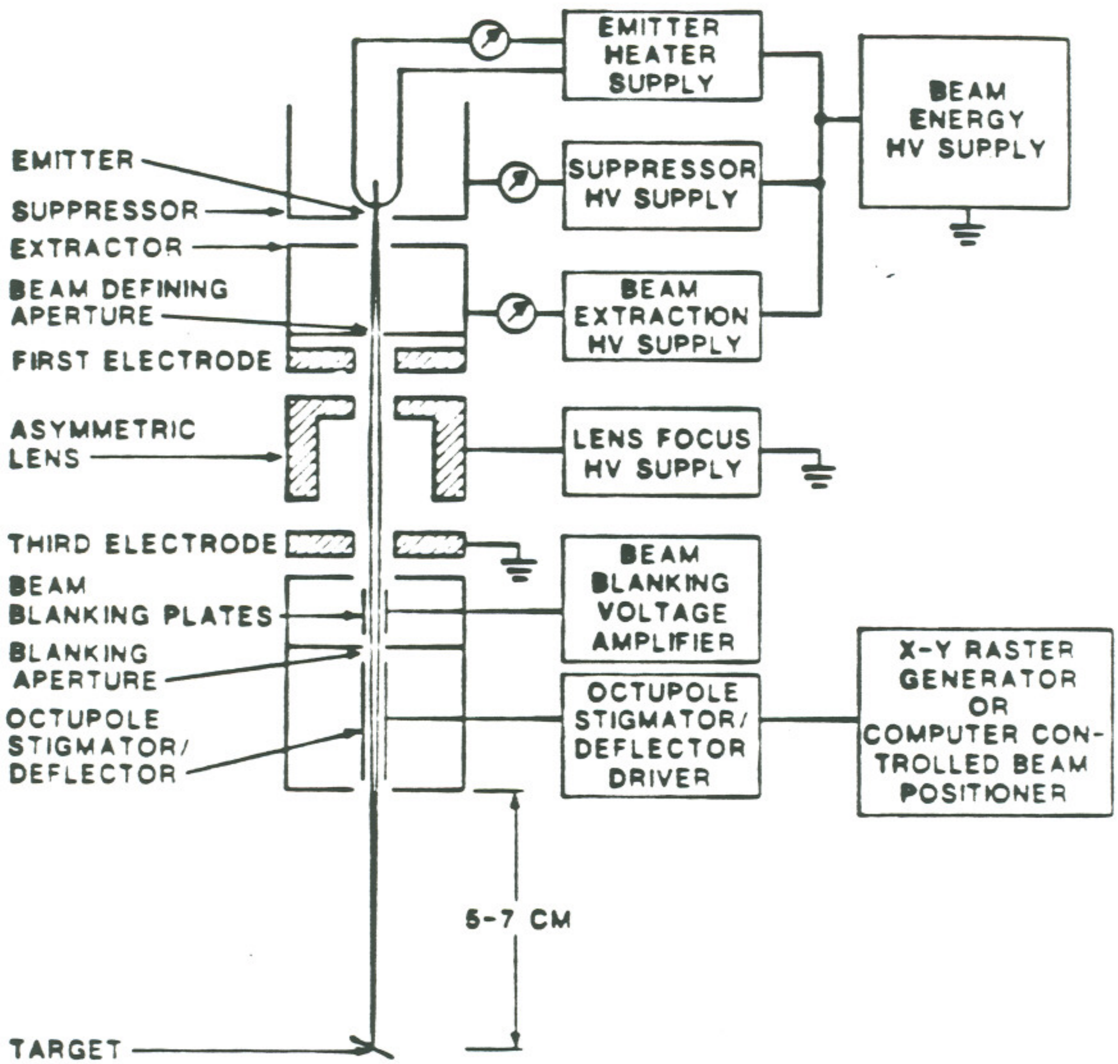

Figure 1.2 Schematic diagram of an FIBM workstation consisting of a liquid metal ion source, a three-element asymmetric einzel lens, and an octopole stigmator/defector, for which an ion beam can be focused and deflected by computer controlled DAC's or raster generators.

The specific situation discussed here is that of a focused polarized Gaussian beam coming from the left and scattered by a sphere tipped, perfectly conducting cone. It is illustrated in Figure 1.3 . The incident laser beam, travels through a lens, which was focused onto that small sphere. The cone is a perfect conductor with a tip angle of θ_0 degrees. A spherical coordinate system with the origin at the center of the sphere is chosen as shown in Figure 1.4 .

Close to the tip of the cone, obviously, the laser field is different from the incident one. The purpose of our study is to learn how the field of laser beam changes due to the presence of the cone and sphere and what are the characteristics of its near field and far field. N. K. Kang and L. Swanson did a numerical calculation of the ion frequency electric field and current density distribution for a liquid metal ion source[115]. D. R. Kingham did some experimental work also. [116] But no one has investigated the interaction of the LMIS with a focused laser beam. Our solution is of interest in its own right because many practical waveguide tubes are mounted on conical structures. It is of interest also because it is possible to take care of the transition from the cone to the sphere and cylinder and thereby to confirm the validity of this more general results by reduction to a special case. Currently, the application of the work is the laser modulation of liquid metal ion sources. [117]

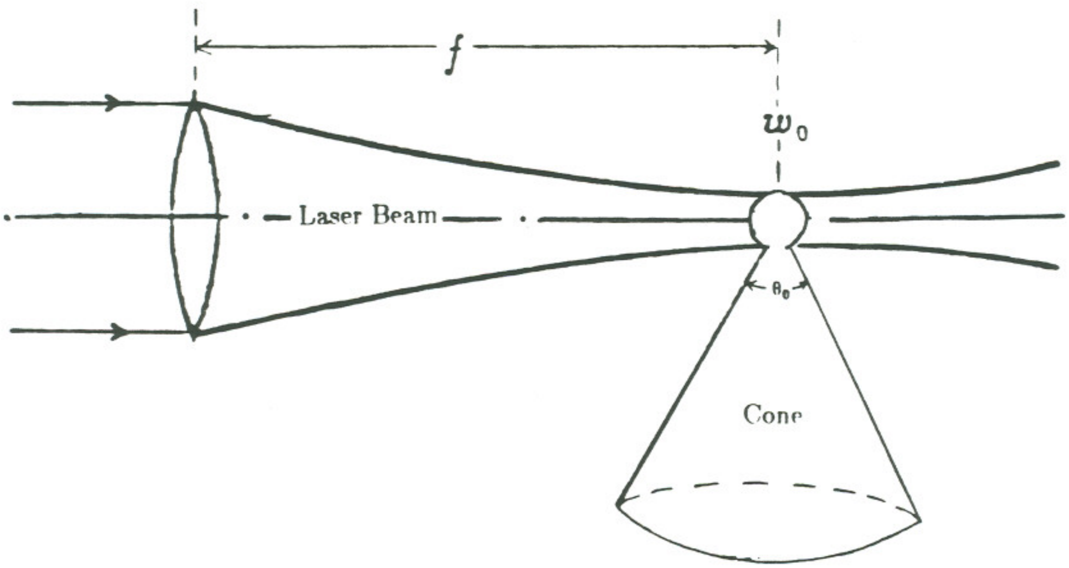

Figure 1.3 A laser beam focused by a lens with focal length f and scattered by a perfectly conducting cone with a small spherical tip

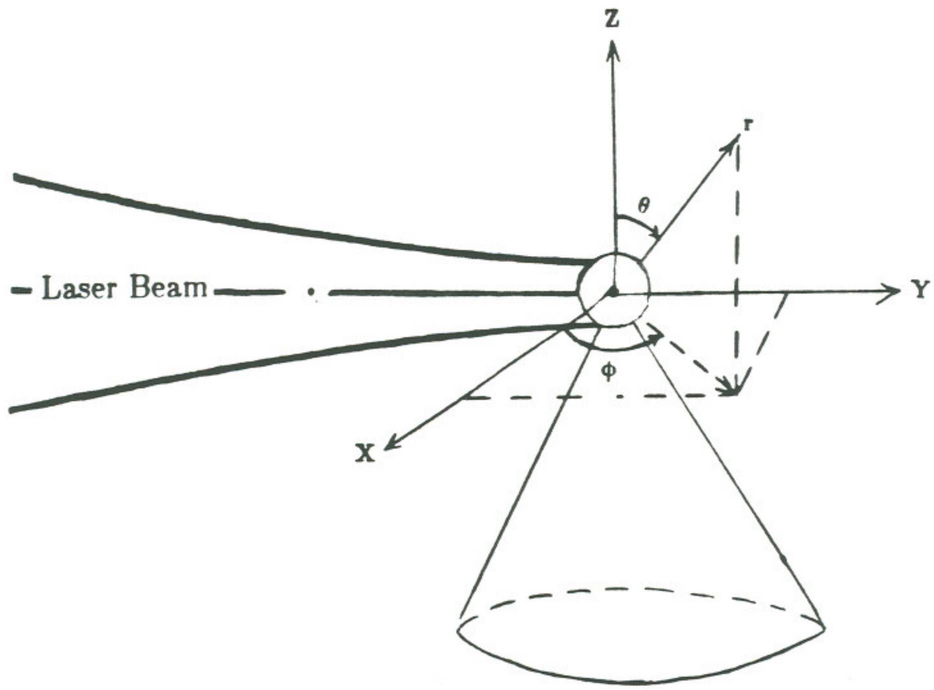

Figure 1.4 Chosen spherical coordinate system

The field distribution around the tip of the cone is determined by the incident field pattern of the laser beam and the boundary conditions on the surface of the cone ($E_{tangential} = 0$) The solution will be obtained with the laser beam polarized in the **z** direction and also in the **x** direction in order to determine the effect of polarization on the results. The method that will be used to solve this problem is the use of Hertz Potentials[114] derived from a modal solution to the wave equation in spherical coordinates. The relationships that are needed will be derived in the next chapter.

CHAPTER 2. HERTZ POTENTIAL

2.1 Electric Hertz Potential

The Hertz potentials can be derived from the well-known Maxwell's equations[118]:

$$\nabla\times \mathbf{E} = - j\,\omega\,\mu\,\mathbf{H} \tag{2.1}$$

$$\nabla\times \mathbf{H} = j\,\omega\,\epsilon\,\mathbf{E} + \mathbf{J} \tag{2.2}$$

$$\nabla\cdot\mathbf{D} = \rho \tag{2.3}$$

$$\nabla\cdot\mathbf{B} = 0 \tag{2.4}$$

Maxwell's equations are a set of four coupled first-order partial differential equations that relate the sources to the various components of the electromagnetic fields. In practice, they can be solved directly only in simple situations. It is often convenient to introduce scalar potential functions from which the field equations can be derived after solving the differential equation for these scalar potentials.

The Hertz Potentials can be used in this manner to determine the electromagnetic fields. In view of equation (2.1), a vector function exists $\mathbf{F}$ such that

$$\mathbf{H} = j\ \omega\ \epsilon\ \nabla \times \mathbf{F} \tag{2.5}$$

It follows then that

$$\begin{aligned} \nabla\times\mathbf{E} &= -j\ \omega\ \mu\ (j\ \omega\ \epsilon\ \nabla \times\mathbf{F}\ ) \\ &= \omega^2\ \epsilon\ \mu\ \nabla\times\mathbf{F} \end{aligned} \tag{2.6}$$

which can be written as:

$$\nabla\times(\mathbf{E}-\ k^2\mathbf{F}\ ) = 0 \tag{2.7}$$

where we have used $k^2 = \omega^2\epsilon\mu$.

According to equation (2.7), the quality in brackets can be expressed as the gradient of a scalar field as follow:

$$\mathbf{E} - k^2\ \mathbf{F} = \nabla\Phi \tag{2.8}$$

Now using equation (2.8), in equation (2.2), it can be written as:

$$\nabla\times\nabla\times\mathbf{F}-k^2\mathbf{F} = \frac{\mathbf{J}}{j\omega\epsilon} + \nabla\Phi \tag{2.9}$$

When $\mathbf{J} = 0$ (sourceless), let $\mathbf{F} = F_r\mathbf{r_0}$, where $\mathbf{r_0}$ is a unit vector in the r- direction. Expanding (2.9), we find that:

In $\mathbf{r_0}$ direction:

$$-\frac{1}{r^2\sin\theta}\left(\frac{\partial}{\partial\theta}\sin\theta\frac{\partial F_r}{\partial\theta}+\frac{1}{\sin\theta}\frac{\partial^2 F_r}{\partial\phi^2}\right) = k^2F_r+\frac{\partial\Phi}{\partial r} \tag{2.10}$$

In $\boldsymbol{\theta_0}$ direction:

$$\frac{1}{r}\frac{\partial^2 F_r}{\partial r\partial\theta} = \frac{1}{r}\frac{\partial\Phi}{\partial\theta} \tag{2.11}$$

In $\boldsymbol{\phi_0}$ direction:

$$\frac{1}{r\sin\theta}\frac{\partial^2 F_r}{\partial r\partial\phi} = \frac{1}{r\sin\theta}\frac{\partial\Phi}{\partial\phi} \tag{2.12}$$

If we choose

$$\frac{\partial F_r}{\partial r} = \Phi \tag{2.13}$$

Instead of the usual Lorentz condition[119], then equations (2.11) and (2.12) are identically satisfied and substituting (2.13) back into (2.10), we get:

$$\frac{1}{r^2 \sin\theta} \left(\frac{\partial^2}{\partial r^2} + \frac{\partial}{\partial \theta} \sin\theta \frac{\partial}{\partial \theta} + \frac{1}{\sin\theta} \frac{\partial^2}{\partial \phi^2} + k^2 \right) F_r = 0 \tag{2.14}$$

Now, let

$$F_r = r\,\Pi \tag{2.15}$$

where Π is the electric Hertz Potential. Substituting equation (2.15) into (2.14), we find that Π satisfies the Helmholtz equation[120]

$$(\nabla^2 + k^2)\, \Pi = 0 \tag{2.16}$$

and the fields can be expressed as:

$$\mathbf{E} = \nabla \times \nabla \times (r\, \Pi \mathbf{r_0}) \tag{2.17}$$

$$\mathbf{H} = j\, \omega\, \epsilon\, \nabla \times (r\, \Pi \mathbf{r_0}) \tag{2.18}$$

2.2 Magnetic Hertz Potential

Using the same method, we can find the magnetic Hertz Potential. In view of equation (2.2), there exists another vector function $\mathbf{G}$, such that:

$$\mathbf{E} = - j\, \omega\, \mu \times \mathbf{G} \tag{2.19}$$

it follows that:

$$\nabla \times \mathbf{H} = j\,\omega\,\epsilon\,(-j\,\omega\,\mu\,\nabla \times \mathbf{G})$$

$$= \omega^2 \epsilon\,\mu\,\nabla \times \mathbf{G} \tag{2.20}$$

which can be written as:

$$\nabla \times (\mathbf{H} - k^2 \mathbf{G}) = 0 \tag{2.21}$$

where we have again used $k^2 = \omega^2 \epsilon \mu$.

In equation (2.21), the quality in brackets can be expressed as the gradient of another scalar field as:

$$\mathbf{H} - k^2 \mathbf{G} = \nabla \Psi \tag{2.22}$$

Using equation (2.22) in (2.1), we have:

$$\nabla \times \nabla \times \mathbf{G} - k^2 \mathbf{G} = \nabla \Psi \tag{2.23}$$

Let

$$\mathbf{G} = G_r\,\mathbf{r_0} \tag{2.24}$$

where $\mathbf{r_0}$ is a unit vector in the r- direction. Expanding equation (2.23), we get:

In $\mathbf{r_0}$ direction:

$$-\frac{1}{r^2\sin\theta}\left(\frac{\partial}{\partial\theta}\sin\theta\frac{\partial G_r}{\partial\theta}+\frac{1}{\sin\theta}\frac{\partial^2 G_r}{\partial\phi^2}\right) = k^2 G_r+\frac{\partial\Psi}{\partial r} \tag{2.25}$$

In $\boldsymbol{\theta_0}$ direction:

$$\frac{1}{r}\frac{\partial^2 G_r}{\partial r\partial\theta} = \frac{1}{r}\frac{\partial\Psi}{\partial\theta} \tag{2.26}$$

In $\boldsymbol{\phi_0}$ direction:

$$\frac{1}{r\sin\theta}\frac{\partial^2 G_r}{\partial r\partial\phi} = \frac{1}{r\sin\theta}\frac{\partial\Psi}{\partial\phi} \tag{2.27}$$

Choosing

$$\frac{\partial G_r}{\partial r} = \Psi \tag{2.28}$$

and substituting (2.28) into (2.25), we find that:

$$\frac{1}{r^2\sin\theta}\left(\frac{\partial^2}{\partial r^2}+\frac{\partial}{\partial\theta}\sin\theta\frac{\partial}{\partial\theta}+\frac{1}{\sin\theta}\frac{\partial^2}{\partial\phi^2}+k^2\right)G_r = 0 \tag{2.29}$$

Let

$$G_r = r\,\Pi^* \tag{2.30}$$

where Π^* is the magnetic Hertz Potential. Substituting equation (2.30) into (2.29), we find that Π^* satisfies the Helmholtz equation

$$(\nabla^2 + k^2) \Pi^* = 0 \tag{2.31}$$

and the fields should be expressed as:

$$\mathbf{E} = - j \omega \mu \nabla \times (r\mathbf{\Pi}^* \mathbf{r_0}) \tag{2.32}$$

$$\mathbf{H} = \nabla \times \nabla \times (r\mathbf{\Pi}^* \mathbf{r_0}) \tag{2.33}$$

In Chapter 3, we will develop the explicit representations of Π and Π^* according to the modal solutions of the Helmholtz equation in spherical coordinates[121].

CHAPTER 3. THEORY

3.1 The Incident Laser Fields

We have the incident laser field (See Fig 1.2) which is propagating along the y axis and with the electrical field polarized in the **x** or **z** directions. The fields can be written as[10,122]:

Polarized in **x** direction:

$$E_{i,x}=-\frac{j}{\omega_0}\frac{2\sqrt{z_0 P}}{\sqrt{\pi}}\Psi_0 e^{-jky} \tag{3.1}$$

$$E_{i,y}=-\frac{2Qx}{l}E_{i,x} \tag{3.2}$$

$$E_{i,z}=0 \tag{3.3}$$

$$H_{i,x}=0 \tag{3.4}$$

$$H_{i,y}=-\frac{2Qz}{l}H_{i,z} \tag{3.5}$$

$$H_{i,z}=\sqrt{\epsilon/\mu}E_{i,x} \tag{3.6}$$

Where ω_0 is the radius of the beam waist; $Q = 1/(j + 2 \zeta)$; $\zeta = y/l$; $\Psi_0 = j\ Q \exp(-j\ Q\ \rho^2\ )$; $\rho^2 = (\ x^2+z^2\ )\ /\ \omega_0^2$, $l = k\ \omega_0^2$, $z_0 = (\mu/\epsilon)^{1/2}$, the characteristic impedance of the medium and P is the total laser power.

If the incident laser beam has **z** polarization, the fields are:

$$E_{i,x}=0 \tag{3.7}$$

$$E_{i,y}=-\frac{2Qz}{l}E_{i,z} \tag{3.8}$$

$$E_{i,z}=-\frac{j}{\omega_0}\frac{2\sqrt{z_0P}}{\sqrt{\pi}}\Psi_0e^{-jky} \tag{3.9}$$

$$H_{i,x}=\sqrt{\epsilon/\mu}E_{i,z} \tag{3.10}$$

$$H_{i,y}=-\frac{2Qx}{l}H_{i,x} \tag{3.11}$$

$$H_{i,z}=0 \tag{3.12}$$

The derivation of the above is in Appendix A.

According to the above, we express the incident laser field as:

$$\mathbf{E}_i=E_{i,x}\mathbf{i} + E_{i,y}\mathbf{j} + E_{i,z}\mathbf{k} \tag{3.13a}$$

$$\mathbf{H}_i = H_{i,x}\mathbf{i} + H_{i,y}\mathbf{j} + H_{i,z}\mathbf{k} \tag{3.14a}$$

In the spherical coordinate system, we have:

$$x = r\sin\theta\cos\phi$$

$$y = r\sin\theta\sin\phi \tag{3.15}$$

$$z = r\cos\theta$$

and[121]

$$\mathbf{i} = \mathbf{r_0}\sin\theta\cos\phi + \boldsymbol{\theta_0}\cos\theta\cos\phi - \boldsymbol{\phi_0}\sin\phi$$

$$\mathbf{j} = \mathbf{r_0}\sin\theta\sin\phi + \boldsymbol{\theta_0}\cos\theta\sin\phi + \boldsymbol{\phi_0}\cos\phi \tag{3.16}$$

$$\mathbf{k} = \mathbf{r_0}\cos\theta - \boldsymbol{\theta_0}\sin\theta$$

so that the incident laser field can be expressed in spherical coordinate system as:

$$\mathbf{E}_i(r,\theta,\phi) = E_r\mathbf{r_0} + E_\theta\boldsymbol{\theta_0} + E_\phi\boldsymbol{\phi_0} \tag{3.13b}$$

$$\mathbf{H}_i(r,\theta,\phi) = H_r\mathbf{r_0} + H_\theta\boldsymbol{\theta_0} + H_\phi\boldsymbol{\phi_0} \tag{3.14b}$$

For **x** polarization,

$$\mathbf{E}_i(r,\theta,\phi)=E_{i,x}\left[(\sin\theta\cos\phi-\frac{2Qx}{l}\sin\theta\sin\phi)\mathbf{r_0}+(\cos\theta\cos\phi+\frac{2Qx}{l}\cos\theta\sin\phi)\boldsymbol{\theta_0}\right.$$

$$\left.-(\sin\phi+\frac{2Qx}{l}\cos\phi)\boldsymbol{\phi_0}\right] \tag{3.17a}$$

$$\mathbf{H}_i(r,\theta,\phi)=\sqrt{\epsilon/\mu}E_{i,x}\left[(\frac{2Qz}{l}\sin\theta\sin\phi-\cos\theta)\mathbf{r_0}+\right.$$

$$\left.(\frac{2Qz}{l}\cos\theta\sin\phi+\sin\theta)\boldsymbol{\theta_0}+\frac{2Qz}{l}\cos\phi\boldsymbol{\phi_0}\right] \tag{3.17b}$$

For **z** polarization,

$$\mathbf{E}_i(r,\theta,\phi)=E_{i,z}\left[(\cos\theta-\frac{2Qz}{l}\sin\theta\sin\phi)\mathbf{r_0}-(\sin\theta+\frac{2Qz}{l}\cos\theta\sin\phi)\boldsymbol{\theta_0}\right.$$

$$\left.-\frac{2Qz}{l}\cos\phi\boldsymbol{\phi_0}\right] \tag{3.18a}$$

$$\mathbf{H}_i(r,\theta,\phi)=\sqrt{\epsilon/\mu}E_{i,z}\left[(\sin\theta\cos\phi+\frac{2Qx}{l}\sin\theta\sin\phi)\mathbf{r_0}+\right.$$

$$\left.(\cos\theta\cos\phi+\frac{2Qx}{l}\cos\theta\sin\phi)\boldsymbol{\theta_0}+\frac{2Qx}{l}(\cos\phi-\sin\phi)\boldsymbol{\phi_0}\right] \tag{3.18b}$$

3.2 Field Components

Considering the fields around the tip of the cone, we can assume that it is the sum of the incident and scattered fields. As is well known, the general electromagnetic fields solution can be obtained by expressing the field as a sum of two subfields[10]: the electric wave field (designated by the subscript e) which is assumed to have a zero radial magnetic field component ($H_r = 0$) and a magnetic wave field (designated by the subscript m) which is assumed to have a zero radial electric field component ($E_r = 0$) i.e.,

$$\mathbf{E}=\mathbf{E}_e+\mathbf{E}_m \tag{3.19}$$

$$\mathbf{H}=\mathbf{H}_e+\mathbf{H}_m \tag{3.20}$$

The advantage of doing this is that each subfield can be expressed solely as a function of a single respective scalar potential, i.e., Hertz Potential Π and Π^* like:

$$\mathbf{E}_e=\nabla\times\nabla\times[r\mathbf{r_0}\Pi]=k^2 r\Pi\mathbf{r_0}+\nabla\left[\frac{\partial}{\partial r}(r\Pi)\right] \tag{3.21}$$

$$\mathbf{E}_m=-j\omega\mu\nabla\times[r\mathbf{r_0}\Pi^*] \tag{3.22}$$

$$\mathbf{H}_e = j\omega\epsilon\nabla\times[r\mathbf{r}_0\Pi] \tag{3.23}$$

$$\mathbf{H}_m = \nabla\times\nabla\times[r\mathbf{r}_0\Pi^*] = k^2 r\Pi^*\mathbf{r}_0 + \nabla\left[\frac{\partial}{\partial r}(r\Pi^*)\right] \tag{3.24}$$

In a spherical coordinate system, in terms of the scalar potential associated with the electric Hertz Potential (Π) and the scalar potential associated with magnetic Hertz Potential (Π^*) the electromagnetic field components (in M.K.S.E. unit) are[10]:

$$E_r = \frac{\partial^2(r\Pi)}{\partial r^2} + k^2 r\Pi \tag{3.25}$$

$$E_\theta = \frac{1}{r}\frac{\partial^2(r\Pi)}{\partial\theta\partial r} - \frac{j\omega\mu}{r\sin\theta}\frac{\partial(r\Pi^*)}{\partial\phi} \tag{3.26}$$

$$E_\phi = \frac{1}{r\sin\theta}\frac{\partial^2(r\Pi)}{\partial r\partial\phi} + \frac{j\omega\mu}{r}\frac{\partial(r\Pi^*)}{\partial\theta} \tag{3.27}$$

and

$$H_r = \frac{\partial^2(r\Pi^*)}{\partial r^2} + k^2 r\Pi^* \tag{3.28}$$

$$H_\theta = \frac{j\omega\epsilon}{r\sin\theta}\frac{\partial(r\Pi)}{\partial\phi} + \frac{1}{r}\frac{\partial^2(r\Pi^*)}{\partial r\partial\theta} \tag{3.29}$$

$$H_\phi = -\frac{j\omega\epsilon}{r}\frac{\partial(r\Pi)}{\partial\theta} + \frac{1}{r\sin\theta}\frac{\partial^2(r\Pi^*)}{\partial r\partial\phi} \tag{3.30}$$

In the above, the introduced Hertz Potentials Π and Π^* were proved in part II to satisfy the Helmholtz equation as follows[123]:

$$(\nabla^2+k^2)\Pi(\mathbf{r})=0 \qquad (3.31)$$

$$(\nabla^2+k^2)\Pi^*(\mathbf{r})=0 \qquad (3.32)$$

Considering we need to solve the equations (3.31) and (3.32), we would like to employ the modal solution of the Helmholtz equation[10] and use the boundary conditions on the surfaces of the spherical tip and cone[2] and the incident field distribution to get the representations of Π and Π^*.

It is at this point that the derivation of an arbitrary incident beam differs from the traditional derivation for an incident plane wave. Instead of choosing a series solution with a form corresponding to that for a polarized plane wave propagating alone the **y** axis, the most general separation of variables solution of the Holmholtz equation is used[3]:

$$r\Pi=\sum_{l}\sum_{m=0}^{\infty}\left[\, A_{lm}\, r\, j_l(kr) + B_{lm}\, r\, n_l(kr)\,\right] P_l^m(\cos\theta)e^{jm\phi} \qquad (3.33)$$

where A_{lm} and B_{lm} are arbitrary constants, j_l (kr) and n_l (kr) are the spherical Bessel functions of the first and second kind corresponding to standing waves[124]. $P_l^m(\cos\theta)$ is the Associated Legendre function of the first kind[125]. Its second kind $Q_l^m(\cos\theta)$ is not used because of its divergency in the range of $-1 < \cos\theta < +1$. On the other hand, its end points $\theta = 0°$ or $180°$ are not included in $Q_l^m(\cos\theta)$. These made the second kind of associated Legendre function is usefuless when dealing with our problems.

The electric wave and magnetic wave scalar potentials for the incident fields (designated by the subscript i) and scattered field (designated by the subscript s) are now expressed in a form consistent with equation (3.33). For the incident field,

$$r\Pi_i = \sum_{p} \sum_{m=0}^{\infty} A_{pm}\ r\ j_p(kr)\ P_p^m(\cos\theta) e^{jm\phi} \tag{3.34}$$

and

$$r\Pi_i^* = \sum_{q} \sum_{n=0}^{\infty} B_{qn}\ r\ j_q(kr)\ P_q^n(\cos\theta) e^{jn\phi} \tag{3.35}$$

where the $n_l(kr)$ functions have been excluded since this function is unbounded at the origin and the incident field should be describable everywhere, including the origin. For the scattered field,

$$r\Pi_s = \sum_{p} \sum_{m=0}^{\infty} a_{pm}\ r\ h_p^{(2)}(kr)\ P_p^m(\cos\theta) e^{jm\phi} \tag{3.36}$$

$$r\Pi_s^* = \sum_q \sum_{n=0}^{\infty} b_{qn}\ r\ h_q^{(2)}(kr)\ P_q^n(\cos\theta)e^{jn\phi} \tag{3.37}$$

where $h_p^{(2)}(kr)$ or $h_q^{(2)}$ (kr) are the spherical Hankel function chosen because their functions[126], in the limit of large r, correspond to outward traveling waves, appropriate for the scattered field.

Substituting equations (3.34) -- (3.37) into (3.25) -- (3.30) provides expressions of the incident and scattered electromagnetic fields. For brevity, only the expressions for the electric field components are given here. The magnetic field components are given in Appendix B.

According to equations (3.25) -- (3.27), here we still like to express the electric field (both incident and scattered fields) as their three components (r, θ , ϕ). Substituting Π and Π^* into equations (3.25), (3.26) and (3.27), after simplifying, we get the incident and scattered electric fields, expressed in terms of the spherical Bessel function[127, 128] $j_p(kr)$ or $j_q(kr)$ and Associated Legendre function $P_p^m(\cos\theta)$ or $P_q^n(\cos\theta)$, as follows[129, 130]:

The incident electric fields:

$$E_{i,r} = \frac{1}{r}\sum_p \sum_{m=0}^{\infty} \left[p(p+1)A_{pm}j_p(kr)P_p^m(\cos\theta)e^{jm\phi}\right] \tag{3.38}$$

$$E_{i,\theta} = \frac{1}{r}\sum_p \sum_{m=0}^{\infty} A_{pm}\left[j_p(kr)+krj_p'(kr)\right]\frac{dP_p^m(\cos\theta)}{d\theta}e^{jm\phi}$$

$$+\frac{1}{r}\sum_{q}\sum_{n=0}^{\infty}\frac{n\omega\mu}{\sin\theta}B_{qn}\ r\ j_q(kr)P_q^n(\cos\theta)e^{jn\phi} \tag{3.39}$$

and

$$E_{i,\phi}=\frac{1}{r}\sum_{p}\sum_{m=0}^{\infty}jmA_{pm}\left[j_p(kr)+krj_p^{'}(kr)\right]\frac{P_p^m(\cos\theta)}{\sin\theta}e^{jm\phi}$$

$$+\frac{1}{r}\sum_{q}\sum_{n=0}^{\infty}j\omega\mu B_{qn}\ r\ j_q(kr)\frac{dP_q^n(\cos\theta)}{d\theta}e^{jn\phi} \tag{3.40}$$

The scattered electric fields:

$$E_{s,r}=\frac{1}{r}\sum_{p}\sum_{m=0}^{\infty}\left[p(p+1)a_{pm}h_p^{(2)}(kr)P_p^m(\cos\theta)\right]e^{jm\phi} \tag{3.41}$$

$$E_{s,\theta}=\frac{1}{r}\sum_{p}\sum_{m=0}^{\infty}a_{pm}\left[h_p^{(2)}(kr)+krh_p^{(2)'}(kr)\right]\frac{dP_p^m(\cos\theta)}{d\theta}e^{jm\phi}$$

$$+\frac{1}{r}\sum_{q}\sum_{n=0}^{\infty}\frac{n\omega\mu}{\sin\theta}b_{qn}\ r\ h_q^{(2)}(kr)P_q^n(\cos\theta)e^{jn\phi} \tag{3.42}$$

and

$$E_{s,\phi}=\frac{1}{r}\sum_{p}\sum_{m=0}^{\infty}jma_{pm}\left[h_p^{(2)}(kr)+krh_p^{(2)'}(kr)\right]\frac{P_p^m(\cos\theta)}{\sin\theta}e^{jm\phi}$$

$$+\frac{1}{r}\sum_{q}\sum_{n=0}^{\infty}j\omega\mu b_{qn}\ r\ h_q^{(2)}(kr)\frac{dP_q^n(\cos\theta)}{d\theta}e^{jn\phi} \tag{3.43}$$

where the superscript prime refers to the derivative of the function with respect to its argument.

The coefficients that describe the scattered field, a_{pm} and b_{qn} , can be related to the coefficients that describe the incident field, A_{pm} and B_{qn} , by application of the boundary conditions on the surface of the cone and its spherical tip.

In Appendix C, we are going to prove that the expanded incident field in Harmonic expression in spherical coordinate is as same as its in Cartesian coordinate system, i.e., equations (3.38) - (3.40) identify with (3.1) - (3.3) and the final solution which satisfying the boundary conditions is also verified.

3.3 Boundary Conditions

On the surface of the cone (See Fig 1.4), $\theta=\theta_0$ and at the surface of the spherical tip, r = a . The boundary conditions are that the tangential electrical fields must be zero on these surfaces. This can be written in terms of the Hertz Potential as: [6,130]

$$\Pi|_{\theta=\theta_0}=0 \tag{3.44}$$

$$\frac{\partial \Pi^*}{\partial \theta}\Big|_{\theta=\theta_0}=0 \tag{3.45}$$

$$\frac{\partial}{\partial r}(r\Pi)\Big|_{r=a}=0 \tag{3.46}$$

$$\Pi^*\Big|_{r=a}=0 \tag{3.47}$$

Note that Π and Π^* here are the sum of the incident fields and the scattered fields. i.e.,

$$\Pi=\Pi_i+\Pi_s \tag{3.48}$$

and

$$\Pi^*=\Pi_i^*+\Pi_s^* \tag{3.49}$$

Using equations (3.34) and (3.36) to substitute into one of the boundary conditions, i.e., into equation (3.46), results in,

$$\sum_p \sum_{m=0}^{\infty} \left\{ A_{pm} \frac{\partial}{\partial r}\left[r j_p(kr) \right] + a_{pm} \frac{\partial}{\partial r}\left[r h_p^{(2)}(kr) \right] \right\} \times$$

$$P_p^m(\cos\theta) e^{jm\phi}\Big|_{r=a}=0 \tag{3.50}$$

Using the orthogonality relations, we know that

$$\int_0^{2\pi} e^{jm\phi} e^{jm'\phi} d\phi = 2\pi\delta_{m,m'} \tag{3.51}$$

where the δ function is defined as:

$$\delta_{i,j} = \begin{cases} 1 & \text{if } i=j \\ 0 & \text{if } i \neq j \end{cases} \tag{3.52}$$

and for the non-integer degree associated Legendre Function, we have[119]:

$$\int_{x_0}^{1} [P_p^m(x)][P_{p'}^m(x)]dx = \frac{x_0^2-1}{2p+1} \left[\frac{\partial P_p^m(x)}{\partial x} \frac{\partial P_p^m(x)}{\partial p} \right]_{x=x_0} \delta_{p,p'} \tag{3.53}$$

Multiplying through by $e^{jm'\phi}$ and $P_{p'}^m(\cos\theta)$ in equation (3.50) and integrating, and using the orthogonality conditions, we get:

$$A_{pm}\left[akj_p'(ka)+j_p(ka)\right]+a_{pm}\left[akh_p^{(2)'}(ka)+h_p^{(2)}(ka)\right]=0 \tag{3.54}$$

so that,

$$a_{pm} = -\frac{A_{pm}[akj_p'(ka)+j_p(ka)]}{akh_p^{(2)'}(ka)+h_p^{(2)}(ka)} \tag{3.55}$$

Now, using equation (3.44), we have [131, 132]

$$\sum_p \sum_{m=0}^{\infty} \left[A_{pm}j_p(kr)+a_{pm}h_p^{(2)}(kr)\right] P_p^m(\cos\theta_0)e^{jm\phi}=0 \tag{3.56}$$

from which we conclude that

$$P_p^m(\cos\theta_0)=0 \tag{3.57}$$

From this equation, we understand that there is a series of values of p depending on m which make (3.57) is true. Using a computer program, we get the calculated results in Table 3.1. The p's are the noninteger degrees which made the Associated Legendre function $P_p^m(\cos\theta_0) = 0$, the m's are the integer orders and the k's mean the k^{th} root of equation (3.57) in assending order of the value of p. The detailed computing process is explained in Appendix D.

In Fig 3.1, the zero points are shown for m=0, m=1 and m=2. This graph verifies our p's which make $P_p^m(\cos\theta_0) = 0$. Fig 3.2 shows the zero points of $P_p^1(\cos\theta_0)$ for $\theta_0 = 20^0, 40^0, \ldots\ldots 180^0$. Using the same procedure, if we use equations (3.35) and (3.37) to substitute into the other boundary condition, i.e., into equation (3.47), that yields:

$$\sum_q \sum_{n=0}^{\infty} \left[B_{qn}j_q(kr)+b_{qn}h_q^{(2)}(kr)\right]P_q^n(\cos\theta)e^{jn\phi}\,|_{\,r=a}=0 \tag{3.58}$$

the orthogonality conditions are given by

$$\int_{x_0}^{1}[P_q^n(x)][P_{q'}^n(x)]dx=\frac{x_0^2-1}{2q+1}\left[\frac{\partial P_q^n(x)}{\partial x}\,\frac{\partial P_q^n}{\partial q}\right]_{x=x_0}\delta_{q,q'} \tag{3.59}$$

Table 3.1

Values of p and m Satisfying $P_p^m(\cos 135^\circ) = 0$

k	1	2	3	4	5	6	7	8
m=0 p	0.495	1.71	3.12	4.40	5.79	7.09	8.48	9.75
m=1 p	1.21	2.49	3.88	5.10	6.48	7.78	9.19	10.45
m=2 p	2.09	3.31	4.65	5.90	7.23	8.55	9.89	11.19
m=3 p	3.09	4.14	5.49	6.74	8.00	9.30	10.63	11.95
m=4 p	5.09	6.30	7.52	8.83	10.09	11.47	12.78	14.06
m=5 p	6.01	7.23	8.40	9.70	10.09	12.23	13.57	
m=6 p	7.08	8.23	9.34	10.59	11.82	13.10		
m=7 p	8.00	9.15	10.25	11.45	12.69	13.93		
m=8 p	8.99	10.09	11.18	12.35	13.55	14.80		

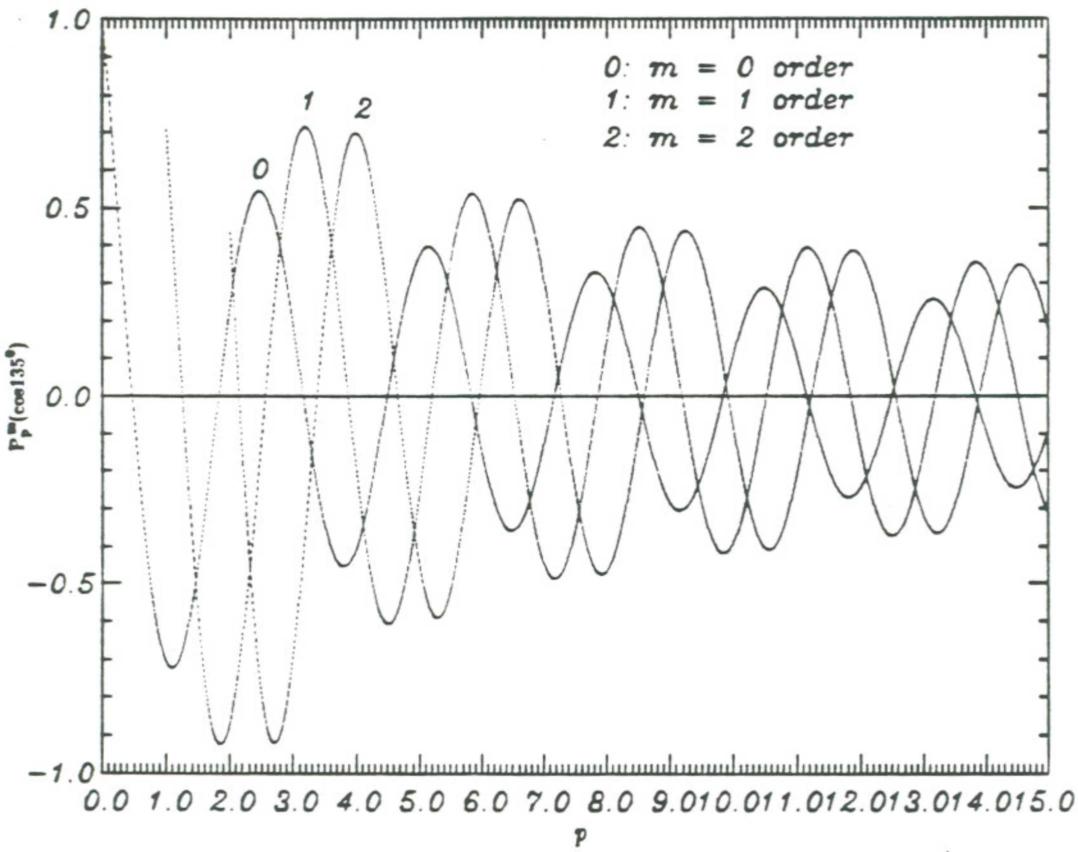

Figure 3.1 The zero points of associated Legendre functions

Table 3.2

Zeros of $P^1_{p_k}$ ($\cos \theta_0$) from $\theta_0 = 20^0$ to 180^0 with step 20^0

k	20	40	60	80	100	120	140	160	180
1	10.49	5.90	3.60	2.30	1.77	1.42	1.20	1.05	1.00
2	19.60	11.10	6.82	4.55	3.56	2.90	2.45	2.14	2.00
3	28.65	15.18	9.53	6.81	5.36	4.40	3.72	3.24	3.00
4	37.67	19.91	13.03	9.06	7.15	5.89	5.00	4.35	4.00
5	46.69	24.35	15.24	11.38	8.95	7.39	6.28	5.46	5.00
6	55.65	30.79	18.24	13.56	10.55	8.89	7.57	6.58	6.00
7	64.72	36.71	22.94	17.56	13.55	10.38	8.84	7.70	7.00
8	82.71	41.51	25.04	19.51	14.35	11.98	10.12	8.82	8.00
9	91.72	46.81	28.56	22.81	16.15	13.38	11.41	9.94	9.00
10	100.72	51.00	31.94	24.61	17.95	14.88	12.69	11.06	10.00

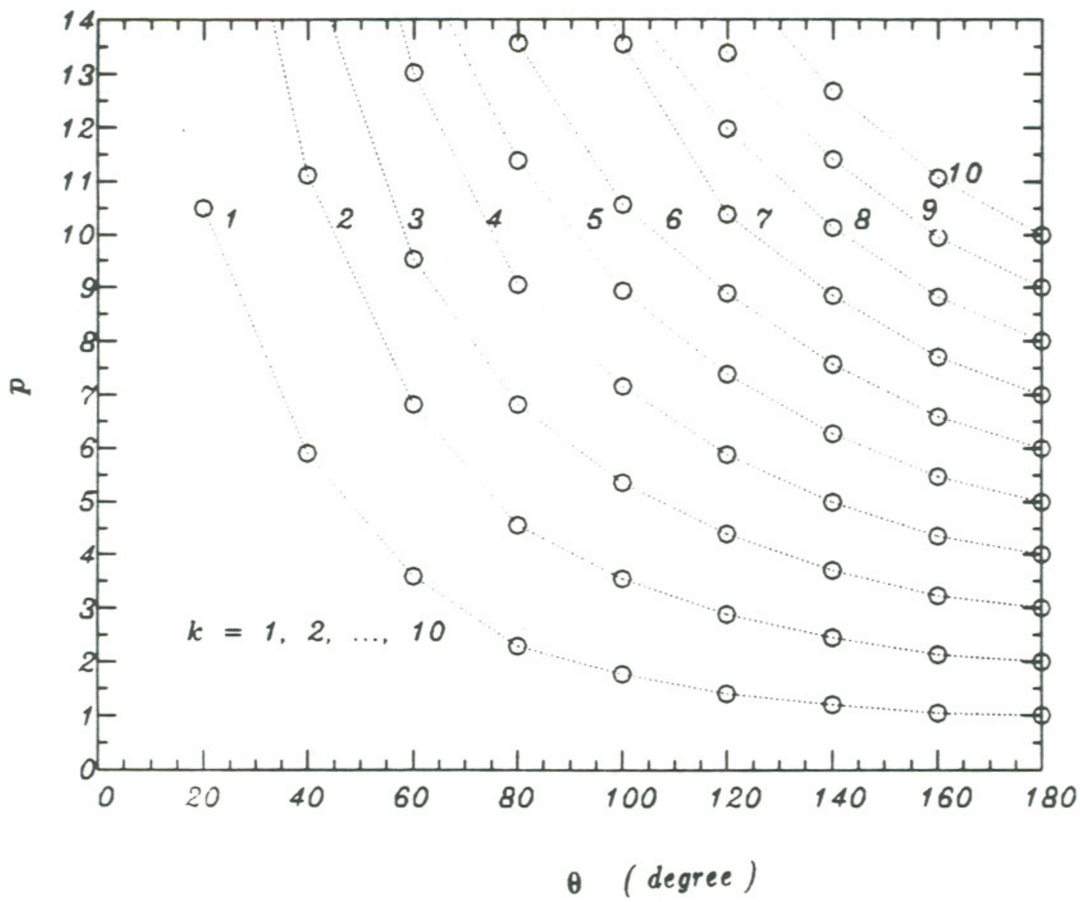

Figure 3.2 The zero points of $P_p^1(\cos\theta)$ from $\theta = 0$ to 180 degree

and equation (3.51). Multiplying through by $P_{q'}^{n}(\cos\theta)$ and $e^{jn'\phi}$ in equation (3.58), using the orthogonality relations (3.51) and (3.53) again, equation (3.58) becomes:

$$B_{qn}j_q(ka)+b_{qn}h_q^{(2)}(ka)=0 \tag{3.60}$$

and

$$b_{qn}=-\frac{B_{qn}j_q(ka)}{h_q^{(2)}(ka)} \tag{3.61}$$

The final boundary condition we have not used is equation (3.55), it is:

$$\frac{\partial\Pi^*}{\partial\theta}\Big|_{\theta=\theta_0}=0 \tag{3.62}$$

Using that in equation (3.58), we can get:

$$\sum_q\sum_{n=0}^{\infty}\left[B_{qn}j_q(kr)+b_{qn}h_q^{(2)}(kr)\right]\frac{\partial P_q^n(\cos\theta)}{\partial\theta}e^{jn\phi}\Big|_{\theta=\theta_0}=0 \tag{3.63}$$

which requires that[132]

$$\frac{\partial P_q^n(\cos\theta_0)}{\partial\theta}=0 \tag{3.64}$$

It can be used to determine the allowable values of q.

Using the program we also can get a series of values of q depending on n which make (3.64) true. Some values of q and n are listed in Table 3.3. The q's are the noninteger degrees which made the derivative of the Associated Legendre functions zero when $\theta=\theta_0$. The n's are the integral orders and the k's are the n^{th} root of equation (3.64) in assending order of the value of q. The detail computing process is explained in Appendix E.

In Fig 3.3, the zero points are showed for m=1 and m=2. This graph verifies our q's which make $\dfrac{dP_q^n(\cos\theta_0)}{d\theta} = 0$.

In accordance with the above discussion, we would like to write the total electrical Hertz Potential and magnetic Hertz Potential in following forms:

$$r\Pi=\sum_{k}\sum_{m=0}^{\infty}\left[A_{p_k,m}\ r\ j_{p_k}(kr) + a_{p_k,m}\ r\ h_{p_k}^{(2)}(kr)\right]P_{p_k}^{m}(\cos\theta)e^{jm\phi} \qquad (3.65)$$

and

$$r\Pi^{*}=\sum_{k}\sum_{n=0}^{\infty}\left[B_{q_k,m}\ r\ j_{q_k}(kr) + b_{q_k,n}\ r\ h_{q_k}^{(2)}(kr)\right]P_{q_k}^{n}(\cos\theta)e^{jn\phi} \qquad (3.66)$$

where $a_{p_k,m}$ and $b_{q_k,n}$ are given by equations (3.55) and (3.61) and $A_{p_k,m}$ and $B_{q_k,n}$ will be obtained from the incident fields as discussed below.

Table 3.3

Values of q and n Satisfying $\frac{dP_q^n(\cos 135^0)}{d\theta} = 0$

k	1	2	3	4	5	6	7	8
n=0								
q	1.20	2.55	3.81	5.20	6.48	7.88	9.11	10.45
n=1								
q	1.91	3.20	4.53	5.88	7.20	8.52	9.80	11.21
n=2								
q	2.80	4.05	5.31	6.61	7.90	9.19	10.55	11.89
n=3								
q	3.82	4.95	6.21	7.46	8.70	10.01	11.30	12.65
n=4								
q	4.80	5.85	7.00	8.30	9.48	10.85	12.10	13.40
n=5								
q	5.85	6.87	7.90	9.13	10.35	11.60	12.88	13.90
n=6								
q	6.82	7.80	8.85	10.08	11.20	12.47	13.70	
n=7								
q	7.90	8.84	9.87	10.96	12.08	13.34	14.48	
n=8								
q	8.92	9.90	10.80	11.90	13.00	14.25		

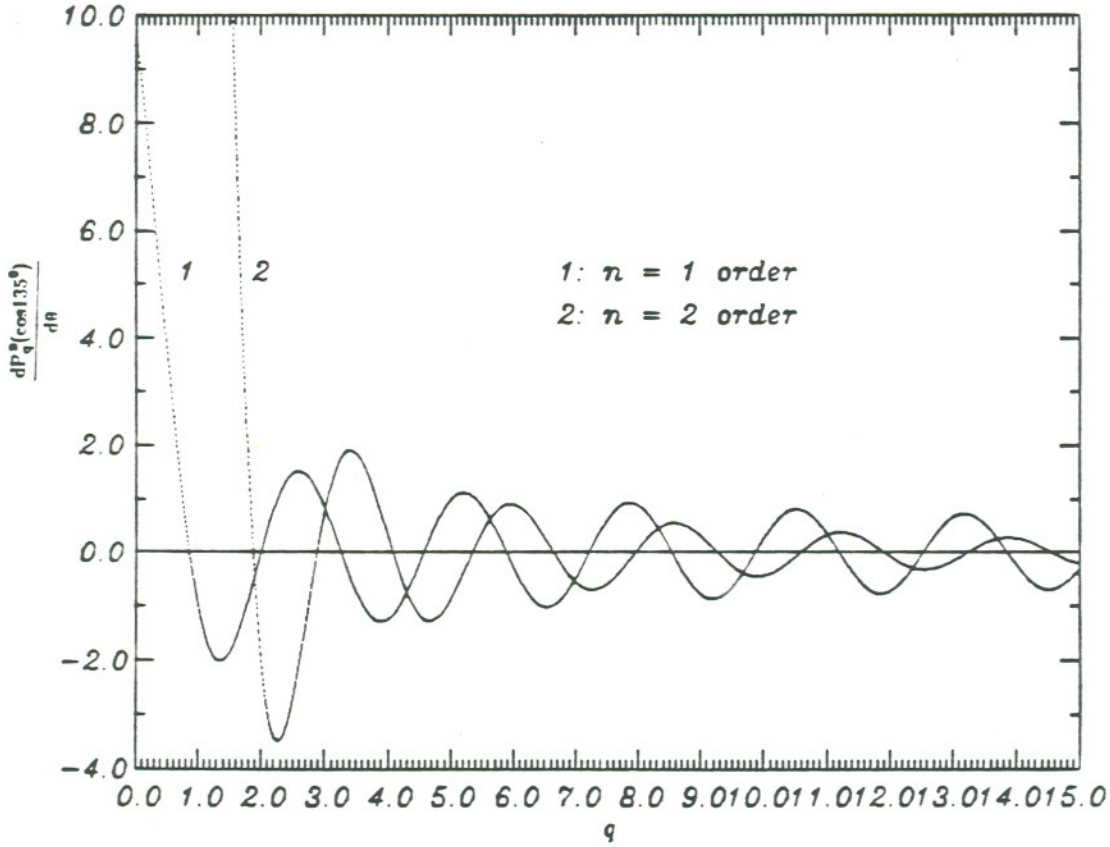

Figure 3.3 The zero points of derivative associated Legendre functions

3.4 Incident Field Expansion Coefficients

3.4.1 x Polarized Field

The final step of this chapter is to determine the coefficients $A_{p_k,m}$ and $B_{q_k,n}$ that describe the incident electromagnetic field. This can be done by expanding the incident field into a series of spherical harmonics at r = a.

Equation (3.17a) can be written as:

$$E_{i,r}(a,\theta,\phi)=(\sin\theta\cos\phi-\frac{2Qx}{l}\sin\theta\sin\phi)E_{i,x}(a,\theta,\phi) \tag{3.67}$$

This function of θ and ϕ only can be expanded in a series of spherical harmonics[133] i.e.,

$$E_{i,r}(a,\theta,\phi)=\sum_{k}\sum_{m=0} e_{p_k,m}P^{m}_{p_k}(\cos\theta)\, e^{jm\phi} \tag{3.68}$$

Using the orthogonality principle, multiplying it through by $e^{jm\phi}$ and $P^{m}_{p_k}(\cos\theta)$ and integrating , we get[134, 135]:

$$\int_0^{2\pi}\int_0^{\theta_0}E_{i,r}(a,\theta,\phi)P^{m}_{p_k}(\cos\theta)e^{jm\phi}\sin\theta d\theta d\phi=$$

$$e_{p_k,m}\frac{2\pi\sin\theta_0}{2p_k+1}\left[\frac{\partial P^{m}_{p_k}(\cos\theta_0)}{\partial\theta}\frac{\partial P^{m}_{p_k}(\cos\theta_0)}{\partial p}\right] \tag{3.69}$$

so that

$$e_{p_k m} = \frac{2p_k+1}{2\pi\sin\theta_0}\left[\frac{\partial P_{p_k}^{m}(\cos\theta_0)}{\partial\theta}\frac{\partial P_{p_k}^{m}(\cos\theta_0)}{\partial p}\right]^{-1}\times$$

$$\int_0^{2\pi}\int_0^{\theta_0} E_{i,r}(a,\theta,\phi)P_{p_k}^{m}(\cos\theta)e^{jm\phi}\sin\theta d\theta d\phi \tag{3.70}$$

Now evaluating equation (3.38) at r = a and using equation (3.68) shows that:

$$\frac{1}{a}\sum_k\sum_{m=0}\left[p_k(p_k+1)\ A_{p_k,m}\ j_{p_k}(ka)\ P_{p_k}^{m}(\cos\theta)e^{jm\phi}\right]=$$

$$=\sum_k\sum_{m=0} e_{p_k,m}P_{p_k}^{m}(\cos\theta)e^{jm\phi} \tag{3.71}$$

so that

$$\frac{p_k(p_k+1)}{a}A_{p_k,m}j_{p_k}(ka)=e_{p_k m} \tag{3.72}$$

and

$$A_{p_k,m}=\frac{a}{p_k(p_k+1)j_{p_k}(ka)}e_{p_k,m} \tag{3.73}$$

Substituting equation (3.70) into (3.73), leads to[136, 137]

$$A_{p_k,m}=\frac{a}{p_k(p_k+1)j_{p_k}(ka)}\frac{2p_k+1}{2\pi\sin\theta_0}\left[\frac{\partial P_{p_k}^{m}(\cos\theta_0)}{\partial\theta}\frac{\partial P_{p_k}^{m}(\cos\theta_0)}{\partial p}\right]^{-1}\times$$

$$\int_0^{2\pi}\int_0^{\theta_0} E_{i,r}(a,\theta,\phi)P_{p_k}^{m}(\cos\theta)e^{jm\phi}\sin\theta d\theta d\phi \tag{3.74}$$

A similar procedure can be used for the magnetic field of laser beam. From equation (3.17b) the incident magnetic field in radial direction is:

$$H_{i,r}(a,\theta,\phi)=\sqrt{\epsilon/\mu}(\frac{2Qz}{l}\sin\theta\sin\phi-\cos\theta)E_{i,x}(a,\theta,\phi) \tag{3.75}$$

We can expand the function of θ and ϕ in a series of spherical harmonics as:

$$H_{i,r}(a,\theta,\phi)=\sum_k\sum_n e_{q_k,n}P_{q_k}^{n}(\cos\theta)e^{jn\phi} \tag{3.76}$$

and it follows that

$$B_{q_k,n}=\frac{a}{q_k(q_k+1)j_{q_k}(ka)}\frac{2q_k+1}{2\pi\sin\theta_0}\left[\frac{\partial P_{q_k}^{n}(\cos\theta_0)}{\partial\theta}\frac{\partial P_{q_k}^{n}(\cos\theta_0)}{\partial q}\right]^{-1}\times$$

$$\int_0^{2\pi}\int_0^{\theta_0} H_{i,r}(a,\theta,\phi)P_{q_k}^{n}(\cos\theta)e^{jn\phi}\sin\theta d\theta d\phi \tag{3.77}$$

All of the unknown coefficients in the series expansions for the field are now known in terms of the incident laser beam fields.

3.4.2 z Polarized Field

Equations (3.18a) and (3.18b) give the expansion for the z polarized electric and magnetic fields. Their radial components are:

$$E_{i,r}(a,\theta,\phi)=(\cos\theta-\frac{2Qz}{l}\sin\theta\sin\phi)E_{i,z}(a,\theta,\phi) \tag{3.78}$$

$$H_{i,r}(a,\theta,\phi)=(\sin\theta\cos\phi+\frac{2Qx}{l}\sin\theta\sin\phi)\sqrt{\epsilon/\mu}E_{i,z}(a,\theta,\phi) \tag{3.79}$$

Using equation (3.78) and (3.79) in (3.74) and (3.77), the incident field coefficients can be evaluated.

In summary, the $A_{p_k,m}$ and $B_{q_k,n}$ coefficients that describe the incident laser field are generated by computing the surface integrals of equations (3.74) and (3.77). Equations (3.55) and (3.61) are then used to determine the coefficients $a_{p_k m}$ and $b_{q_k n}$ that respectively describe the scattered fields[138]. Finally, equations (3.38) and (3.43) are then used to evaluated the electrical field distribution. The magnetic field distribution can be evaluated using the equations presented in Appendix B. In the next section, a numerical example will be presented.

CHAPTER 4. NUMERICAL APPROACH

4.1 The Coefficients of Incident and Scattered Laser Field

In order to numerically evaluate the field distributions, the computer programs have been written incorporating the aforementioned theory of the incident laser beam fields , the scattered fields and the whole field distributions. The required Bessel functions have been evaluated using the recursion technique presented by Ross[138] *et al.* and the required spherical harmonic functions are evaluated using derived recursion formulas based on the associated Legendre function recursion relationships presented by Press[139] *et al.* The surface integrals of equations (3.74), (3.77), (3.80) and (3.81) are determined using standard numerical integration procedures contained in the Numerical Algorithm Group (NAG) library. The assumed known incident laser field components are provided by a subroutine independent from the main computer program. In this way, the same main computer program could be used for different incident electromagnetic fields.

The expressions for the coefficients A_{pm} and B_{qn} which describe the incident laser field were developed in part III. Here we will evaluate them. For convenience, they are repeated here.

$$A_{p_k m} = \frac{a}{p_k(p_k+1)j_{p_k}(ka)} \frac{2p_k+1}{2\pi\sin\theta_0} \left[\frac{\partial P^m_{p_k}(\cos\theta_0)}{\partial\theta} \frac{\partial P^m_{p_k}(\cos\theta_0)}{\partial p} \right]^{-1} \times$$

$$\int_0^{2\pi}\int_0^{\theta_0} E_{i,r}(a,\theta,\phi) P^m_{p_k}(\cos\theta) e^{jm\phi} \sin\theta d\theta d\phi \tag{4.1}$$

$$B_{q_k n} = \frac{a}{q_k(q_k+1)j_{q_k}(ka)} \frac{2q_k+1}{2\pi\sin\theta_0} \left[\frac{\partial P^n_{q_k}(\cos\theta_0)}{\partial\theta} \frac{\partial P^n_{q_k}(\cos\theta_0)}{\partial q} \right]^{-1} \times$$

$$\int_0^{2\pi}\int_0^{\theta_0} H_{i,r}(a,\theta,\phi) P^n_{q_k}(\cos\theta) e^{jn\phi} \sin\theta d\theta d\phi \tag{4.2}$$

These equations are suitable for both **x** polarized and **z** polarized. As long as the incident fields $E_{i,r}(a,\theta,\phi)$ and $H_{i,r}(a,\theta,\phi)$ correspond to the **x** polarized or **z** case. The detail calculation of $\frac{\partial P^m_{p_k}(\cos\theta_0)}{\partial\theta} \frac{\partial P^m_{p_k}(\cos\theta_0)}{\partial p}$ in equation (4.1) and $\frac{\partial P^n_{q_n}(\cos\theta_0)}{\partial\theta} \frac{\partial P^n_{q_n}(\cos\theta_0)}{\partial q}$ in equation (4.2) are shown in Appendix E.

Once the incident field coefficients have been calculated, the scattered field coefficients will be calculated from

$$a_{p_k m} = -\frac{akj'_{p_k}(ka)+j_{p_k}(ka)}{akh^{(2)'}_{p_k}(ka)+h^{(2)}_{p_k}(ka)} A_{p_k m} \tag{4.3}$$

and

$$b_{q_k n} = -\frac{j_{q_k}(ka)}{h_{q_k}^{(2)}(ka)} B_{q_k n} \tag{4.4}$$

In this chapter, We are going to discuss the **z** polarized and **x** polarized field distributions separately in sections 4.2 and 4.3 .

4.2 z Polarized Field Distribution

A reasonable approximation to the entire series solution is to take just enough p_k' s and q_k' s to get a reasonable values of the accurate incident laser field coefficients $A_{p_k m}$, $B_{q_k n}$ and scattered laser field coefficients $a_{p_k m}$ and $b_{q_k n}$. All parameters we used for coefficients computation is listed in Table 4.0.

In Table 4.1 and 4.2, we have listed the first four coefficients of the **z** polarized incident electric and magnetic fields which corresponding to their p's and m's. In Table 4.3 and Table 4.4 , the scattered coefficients are listed, respectively. Since the coefficients are complex so that we write their real parts and imaginary parts separately. Using the equations (4.3) and (4.4), we can calculate the scattered coefficients $a_{p_k m}$ and $b_{q_k n}$. They are listed in Table 4.3 and Table 4.4 .

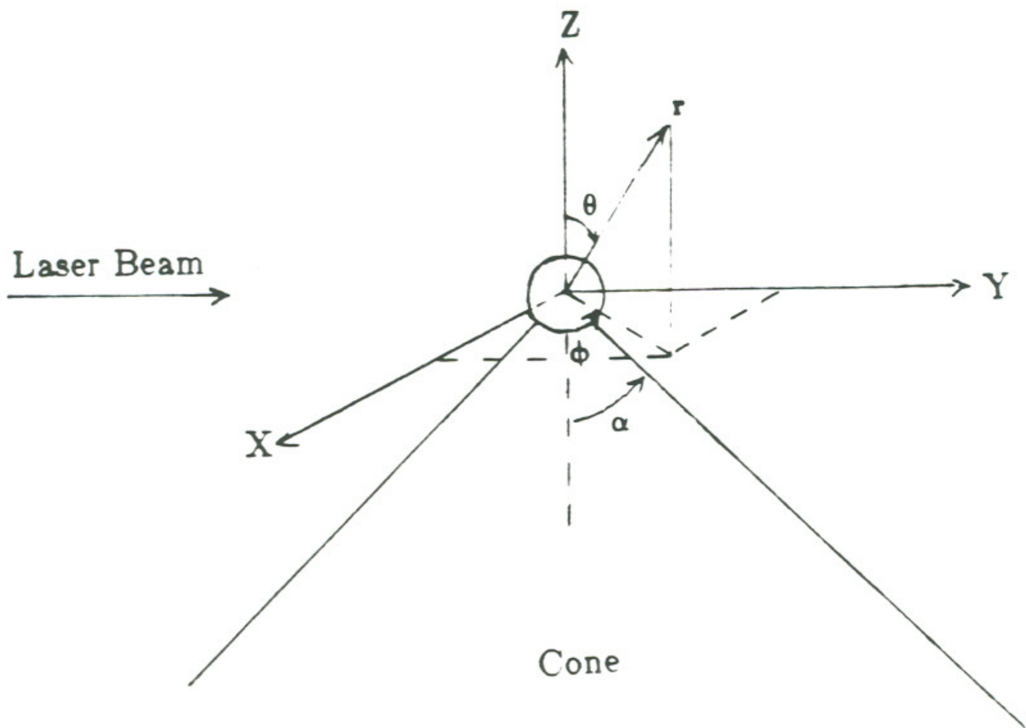

Table 4.0

Parameters Used in Numerical Evaluation

the half angle of the cone	$\alpha = 45^\circ$
the diameter of the sphere	a = 0.02 micron
the wavelength of the laser beam	λ = 0.5 micron
the waist of the focused laser beam	ω_0 = 2 micron

Table 4.1

Electric Field Coefficients of Incident Laser Beam A_{pm}

(z Polarization)

k	1	2	3	4
p/(m=0)	0.495	1.71	3.12	4.40
Apm(real)	-0.8294d-02	-0.2477d-03	-0.7048d-05	-0.5777d-06
Apm(imag.)	-0.1132d+03	-0.3379d+01	-0.9615d-01	-0.7882d-02
p/(m=1)	1.21	2.49	3.88	5.10
Apm(real)	-0.6434d-02	0.1673d-02	0.2947d-04	0.3710d-06
Apm(imag.)	0.2090d+09	-0.5440d+08	-0.9583d+06	-0.1205d+05
p/(m=2)	2.09	3.31	4.65	5.90
Apm(real)	-0.7098d-01	-0.3349d-01	-0.4338d-03	0.9389d-05
Apm(imag.)	0.6211d+08	0.2930d+08	0.3798d+06	-0.8206d+04
p/(m=3)	3.09	4.14	5.49	6.74
Apm(real)	-0.1327d+00	-0.1143d+00	-0.1843d-03	0.5030d-04
Apm(imag.)	0.2269d+07	0.1955d+07	0.3151d+04	-0.8601d+03

Table 4.1 continued

p/(m=4)	5.09	6.30	7.52	8.83
Apm(real)	-0.5585d+00	-0.2870d-01	-0.4701d-02	-0.2792d-03
Apm(imag.)	0.1069d+06	0.5494d+04	0.8995d+03	0.5342d+02
p/(m=5)	6.01	7.23	8.40	9.70
Apm(real)	-0.3218d+05	-0.9007d+03	-0.1778d+03	-0.5690d+01
Apm(imag.)	0.1495d+05	0.4429d+03	0.8742d+02	0.2798d+01
p/(m=6)	7.08	8.23	9.34	10.59
Apm(real)	-0.1068d+05	0.9042d+02	-0.7568d+01	-0.2333d+01
Apm(imag.)	-0.3999d+05	0.3385d+03	-0.2833d+02	-0.8733d+01
p/(m=7)	8.00	9.15	10.25	11.45
Apm(real)	-0.2276d+04	-0.1853d+03	0.1365d+03	-0.3446d+01
Apm(imag.)	0.1011d+04	0.8232d+02	-0.2361d+02	0.5959d+00
p/(m=8)	8.99	10.09	11.18	12.35
Apm(real)	0.1117d+03	0.1163d+02	0.6577d+01	0.1450d+00
Apm(imag.)	0.1823d+03	0.1899d+02	0.1074d+02	0.2367d+00

Table 4.2

Magnetic Field Coefficients of Incident Laser Beam B_{qn}

(z Polarization)

k	1	2	3	4
q/(n=0)	1.20	2.55	3.81	5.20
Bqn(real)	0.1880d+04	-0.2766d+02	0.5175d+01	-0.3624d-02
Bqn(imag.)	-0.1064d+11	0.1565d+09	-0.2928d+08	0.2050d+05
q/(n=1)	1.91	3.20	4.53	5.88
Bqn(real)	0.4626d+00	0.1113d-01	0.1611d-02	0.2511d-03
Bqn(imag.)	-0.1277d+08	-0.3075d+06	-0.4449d+05	-0.6933d+04
q/(n=2)	2.80	4.05	5.31	6.61
Bqn(real)	0.1001d+04	0.1171d+03	0.1539d+02	0.4255d+00
Bqn(imag.)	-0.4322d+06	-0.5054d+05	-0.6642d+04	-0.1836d+03
q/(n=3)	3.82	4.95	6.21	7.46
Bqn(real)	0.4288d+04	0.2358d+03	-0.4851d+02	-0.1444d+01
Bqn(imag.)	0.7654d+05	0.4210d+04	-0.8659d+03	-0.2577d+02

Table 4.2 continued

q/(n=4)	4.80	5.85	7.00	8.30
Bqn(real)	0.1249d+03	-0.3890d+01	-0.1600d+01	-0.5348d+00
Bqn(imag.)	0.1211d+04	-0.3773d+02	-0.5186d+01	-0.2306d+00
q/(n=5)	5.85	6.87	7.90	9.13
Bqn(real)	-0.4569d+04	-0.1603d+03	0.4919d+02	-0.2485d+01
Bqn(imag.)	-0.4892d+02	-0.1712d+01	0.5262d+00	-0.2661d-01
q/(n=6)	6.82	7.80	8.85	10.08
Bqn(real)	-0.1015d+04	0.8900d+02	0.7715d+01	0.1975d+00
Bqn(imag.)	0.5583d+01	-0.4873d+00	-0.4237d-01	-0.1086d-02
q/(n=7)	7.90	8.84	9.87	10.96
Bqn(real)	0.1316d+05	0.8687d+02	-0.8247d+01	-0.2318d+00
Bqn(imag.)	0.3946d+02	0.2589d+00	-0.2462d-01	-0.6964d-03
q/(n=8)	8.92	9.90	10.80	11.90
Bqn(real)	-0.1762d+04	0.5393d+03	0.9235d+01	-0.3520d+01
Bqn(imag.)	0.2992d+01	-0.9160d+00	-0.1567d-01	0.5974d-02

Table 4.3

Electric Field Coefficients of Scattered Laser Beam a_{pm}

($z-$ Polarization)

k	1	2	3	4
p/(m=0)	0.495	1.71	3.12	4.40
apm(real)	0.2991d-05	0.1526d-05	0.2013d-07	0.1582d-10
apm(imag.)	0.1837d-09	-0.1262d-09	-0.1475d-11	-0.1160d-14
p/(m=1)	1.21	2.49	3.88	5.10
apm(real)	-0.7065d+01	0.3597d-01	0.6028d-03	-0.6750d-07
apm(imag.)	0.4140d-02	0.1351d-08	0.2522d-13	-0.2078d-17
p/(m=2)	2.09	3.31	4.65	5.90
apm(real)	0.4318d-01	-0.4990d-03	-0.1024d-05	-0.7253d-11
apm(imag.)	0.2272d-06	-0.1226d-11	-0.1170d-14	-0.8289d-20
p/(m=3)	3.09	4.14	5.49	6.74
apm(real)	0.6531d-05	-0.4000d-08	-0.2288d-10	-0.2062d-15
apm(imag.)	0.4315d-12	-0.2340d-15	-0.1338d-17	-0.1206d-22

Table 4.3 continued

p/(m=4)	5.09	6.30	7.52	8.83
apm(real)	-0.1883d-13	-0.5683d-17	-0.3571d-21	-0.1984d-25
apm(imag.)	-0.9850d-19	-0.2970d-22	-0.1866d-28	0.0d+00
p/(m=5)	6.01	7.23	8.40	9.70
apm(real)	-0.2538d-18	-0.9050d-22	-0.5683d-27	0.0d+00
apm(imag.)	-0.5163d-18	-0.1841d-21	-0.1156d-27	0.0d+00
p/(m=6)	7.08	8.23	9.34	10.59
apm(real)	0.3750d-22	0.1917d-29	0.0d+00	0.0d+00
apm(imag.)	-0.1002d-22	-0.5122d-30	0.0d+00	0.0d+00
p/(m=7)	8.00	9.15	10.25	11.45
apm(real)	-0.3782d-29	0.0d+00	0.0d+00	0.0d+00
apm(imag.)	-0.2187d-30	0.0d+00	0.0d+00	0.0d+00
p/(m=8)	8.99	10.09	11.18	12.35
apm(real)	0.0d+00	0.0d+00	0.0d+00	0.0d+00
apm(imag.)	0.0d+00	0.0d+00	0.0d+00	0.0d+00

Table 4.4

Magnetic Field Coefficients of Scattered Laser Beam b_{qn}

($\mathbf{z}$ Polarization)

k	1	2	3	4
q/(n=0)	1.20	2.55	3.81	5.20
bqn(real)	-0.3736d+01	0.3195d+00	-0.6175d-04	0.2217d-07
bqn(imag.)	-0.6815d-03	0.5996d-07	-0.1091d-10	0.3919d-14
q/(n=1)	1.91	3.20	4.53	5.88
bqn(real)	0.9279d-02	0.9676d-05	0.2469d-09	0.5373d-13
bqn(imag.)	0.1276d-07	0.1004d-12	0.8942d-17	0.1946d-20
q/(n=2)	2.80	4.05	5.31	6.61
bqn(real)	0.2832d-06	0.3406d-09	0.3901d-13	0.1978d-17
bqn(imag.)	0.6561d-09	0.7891d-12	0.9039d-16	0.4582d-20
q/(n=3)	3.82	4.95	6.21	7.46
bqn(real)	0.9344d-11	0.1697d-13	-0.8263d-18	-0.1028d-21
bqn(imag.)	-0.5234d-12	-0.9509d-15	0.4629d-19	0.5757d-23

Table 4.4 continued

q/(n=4)	4.80	5.85	7.00	8.30
bqn(real)	0.1715d-16	0.2878d-19	0.4234d-23	-0.4387d-27
bqn(imag.)	0.1191d-15	-0.2968d-20	-0.4366d-24	0.4524d-28
q/(n=5)	5.85	6.87	7.90	9.13
bqn(real)	0.1476d-21	-0.2042d-24	0.3171d-29	0.0d+00
bqn(imag.)	-0.1379d-19	0.1909d-22	-0.2968d-27	0.0d+00
q/(n=6)	6.82	7.80	8.85	10.08
bqn(real)	0.6785d-27	0.7361d-32	0.0d+00	0.0d+00
bqn(imag.)	0.1234d-25	0.5719d-29	0.0d+00	0.0d+00
q/(n=7)	7.90	8.84	9.87	10.96
bqn(real)	0.4871d-30	0.0d+00	0.0d+00	0.0d+00
bqn(imag.)	0.8572d-29	0.0d+00	0.0d+00	0.0d+00
q/(n=8)	8.92	9.90	10.80	11.90
bqn(real)	0.0d+00	0.0d+00	0.0d+00	0.0d+00
bqn(imag.)	0.0d+00	0.0d+00	0.0d+00	0.0d+00

Now, using all coefficients in Table 4.1, 4.2, 4.3 and 4.4, substituting them into equations (3.38) -- (3.43) and expansion them depending on the coefficients, i.e.,

$$E_{i,r}=\frac{1}{r}\sum_{k}\sum_{m}\left[p_k(p_k+1)A_{p_k m}j_{p_k}(kr)P_{p_k}^{m}(\cos\theta)\right]e^{jm\phi} \tag{4.5}$$

$$E_{s,r}=\frac{1}{r}\sum_{k}\sum_{m}\left[p_k(p_k+1)a_{p_k m}h_{p_k}^{(2)}(kr)P_{p_k}^{m}(\cos\theta)\right]e^{jm\phi} \tag{4.6}$$

So the total electric field in the $\mathbf{r_0}$ direction is:

$$E_r=E_{i,r}+E_{s,r}$$

$$=\frac{1}{r}\sum_{k}p(p+1)\sum_{m}\left[A_{pm}j_p(kr)+a_{pm}h_p^{(2)}(kr)\right]P_p^{m}(\cos\theta)e^{jm\phi}$$

$$=\frac{1}{r}\left\{p_1(p_1+1)\left[A_{p_1m_1}j_{p_1}(kr)+a_{p_1m_1}h_{p_1}^{(2)}(kr)\right]P_{p_1}^{m_1}(\cos\theta)e^{jm_1\phi}+\right.$$

$$p_2(p_2+1)\left[A_{p_2m_2}j_{p_2}(kr)+a_{p_2m_2}h_{p_2}^{(2)}(kr)\right]P_{p_2}^{m_2}(\cos\theta)e^{jm_2\phi}+\ldots\ldots$$

$$\left.+p_k(p_k+1)\left[A_{p_km_k}j_{p_k}(kr)+a_{p_km_k}h_{p_k}^{(2)}(kr)\right]P_{p_k}^{m_k}(\cos\theta)e^{jm_k\phi}\right\} \tag{4.7}$$

Using the same procedure, we get the total electric field in the $\boldsymbol{\theta_0}$ direction as:

$$E_\theta=E_{i,\theta}+E_{s,\theta}$$

$$=\frac{1}{r}\sum_{p_k}\sum_{m}\left\{A_{p_km}\left[j_{p_k}(kr)+krj_{p_k}^{'}(kr)\right]+a_{p_km}\left[h_{p_k}^{(2)}(kr)+krh_{p_k}^{(2)'}(kr)\right]\right\}\frac{dP_{p_k}^{m}(\cos\theta)}{d\theta}e^{jm\phi}+$$

$$\sum_{q_k}\sum_{n}\frac{n\omega\mu}{\sin\theta}\left[B_{q_kn}j_{q_k}(kr)+b_{q_kn}h_{q_k}^{(2)}(kr)\right]P_{q_k}^{n}(\cos\theta)e^{jn\phi}$$

$$=\frac{1}{r}\left\{A_{p_1m_1}\left[j_{p_1}(kr)+krj_{p_1}^{'}(kr)\right]+a_{p_1m_1}\left[h_{p_1}^{(2)}(kr)+krh_{p_1}^{(2)'}(kr)\right]\right\}\frac{dP_{p_1}^{m_1}(\cos\theta)}{d\theta}e^{jm_1\phi}+$$

$$\frac{n_1\omega\mu}{\sin\theta}\left[B_{q_1n_1}j_{q_1}(kr)+b_{q_1n_1}h_{q_1}^{(2)'}(kr)\right]P_{q_1}^{n_1}(\cos\theta)e^{jn_1\phi}+\ldots\ldots$$

$$+\frac{1}{r}\left\{A_{p_km_k}\left[j_{p_k}(kr)+krj_{p_k}^{'}(kr)\right]+a_{p_km_k}\left[h_{p_k}^{(2)}(kr)+krh_{p_k}^{(2)'}(kr)\right]\right\}\frac{dP_{p_k}^{m_k}(\cos\theta)}{d\theta}e^{jm_k\phi}+$$

$$\frac{n_k\omega\mu}{\sin\theta}\left[B_{q_kn_k}j_{q_k}(kr)+b_{q_kn_k}h_{q_k}^{(2)'}(kr)\right]P_{q_k}^{n_k}(\cos\theta)e^{jn_k\phi} \tag{4.8}$$

and in $\boldsymbol{\phi_0}$ direction:

$$E_{\phi}=E_{i,\phi}+E_{s,\phi}$$

$$=\frac{j}{r}\sum_{p_k}\sum_{m}m\left\{A_{p_km}\left[j_{p_k}(kr)+krj_{p_k}^{'}(kr)\right]+a_{p_km}\left[h_{p_k}^{(2)}(kr)+krh_{p_k}^{(2)'}(kr)\right]\right\}\frac{P_{p_k}^{m}(\cos\theta)}{\sin\theta}e^{jm\phi}+$$

$$j\omega\mu\sum_{q_k}\sum_{n}\left[B_{q_kn}j_{q_k}(kr)+b_{q_kn}h_{q}^{(2)}(kr)\right]\frac{dP_{q_k}^{n}(\cos\theta)}{d\theta}e^{jn\phi}$$

$$=\frac{j}{r}\left\{m_1 A_{p_1 m_1}\left[j_{p_1}(kr)+krj_{p_1}'(kr)\right]+m_1 a_{p_1 m_1}\left[h_{p_1}^{(2)}(kr)+krh_{p_1}^{(2)'}(kr)\right]\right\}\frac{P_{p_1}^{m_1}(\cos\theta)}{\sin\theta}e^{jm_1\phi}+$$

$$j\omega\mu\left[B_{q_1 n_1} j_{q_1}(kr)+b_{q_1 n_1} h_{q_1}^{(2)}(kr)\right]\frac{dP_{q_1}^{m_1}(\cos\theta)}{d\theta}e^{jn_1\phi}+\ldots\ldots$$

$$+\frac{j}{r}\left\{m_k A_{p_k m_k}\left[j_{p_k}(kr)+krj_{p_k}'(kr)\right]+m_k a_{p_k m_k}\left[h_{p_k}^{(2)}(kr)+krh_{p_k}^{(2)'}(kr)\right]\right\}\frac{P_{p_k}^{m_k}(\cos\theta)}{\sin\theta}e^{jm_k\phi}+$$

$$j\omega\mu\left[B_{q_k n_k} j_{q_k}(kr)+b_{q_k n_k} h_{q_k}^{(2)}(kr)\right]\frac{dP_{q_k}^{m_k}(\cos\theta)}{d\theta}e^{jn_k\phi} \qquad (4.9)$$

The total electric field then is given by:

$$\mathbf{E}_{\text{total}}=E_r\mathbf{r_0}+E_\theta\boldsymbol{\theta_0}+E_\phi\boldsymbol{\phi_0} \qquad (4.10)$$

and its magnitude is:

$$|E|_{\text{total}}=\sqrt{E_r^2+E_\theta^2+E_\phi^2} \qquad (4.11)$$

The problem that we are most interested in is how the incident field is enhanced by the tip of the cone. Since the field is z polarized, we expect the enhancement to be maximum in the **z** direction, this leads us to make the approximation $\theta \to 0$ before computing the fields E_r , E_θ and E_ϕ . Figure 4.1a through 4.1d show the ratio of the magnitude of the total electric field to the magnitude of the incident electric field as a function of the radial distance r. As expected, the electric field is enhanced by a factor of about 14 on the surface of the sphere (radius = 0.01 micron). As the radial distance increases, the enhancement rapidly decreases to unity.

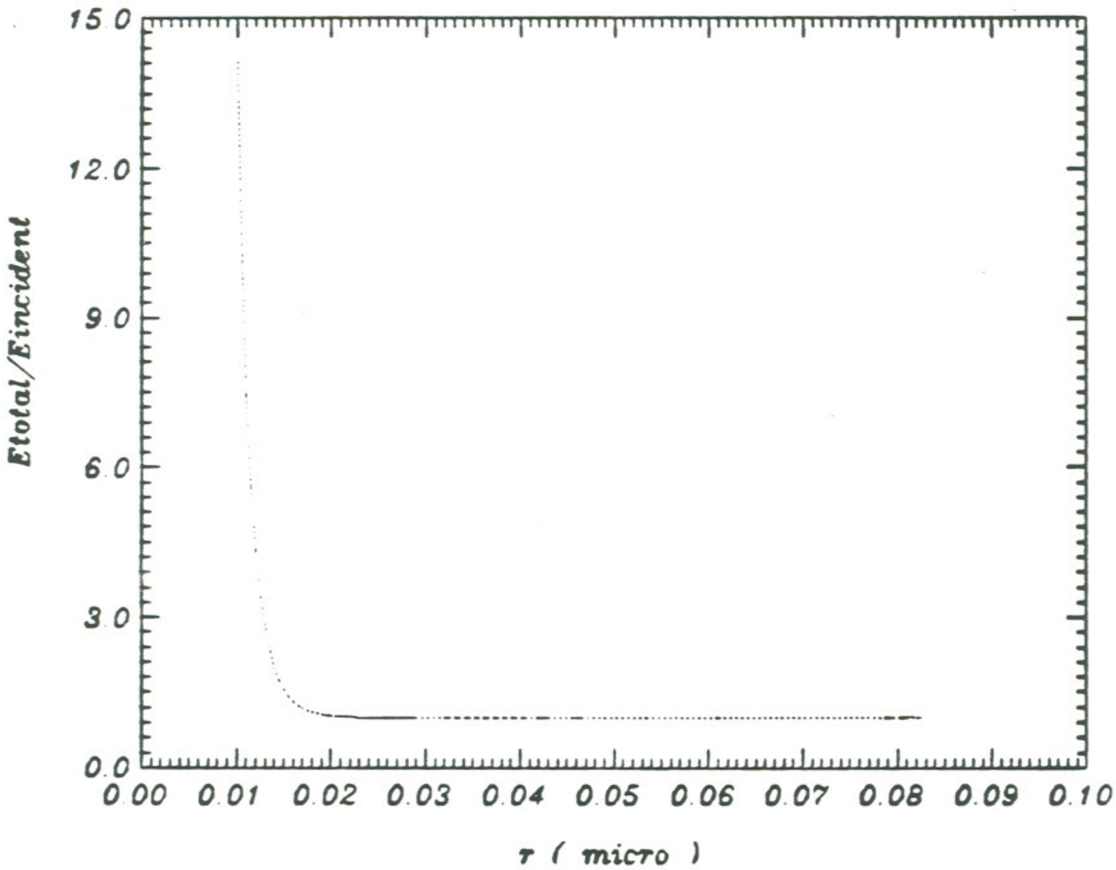

Figure 4.1(a) z polarized field distribution along +x axis

($\theta = 0^0$, $\phi = 0^0$)

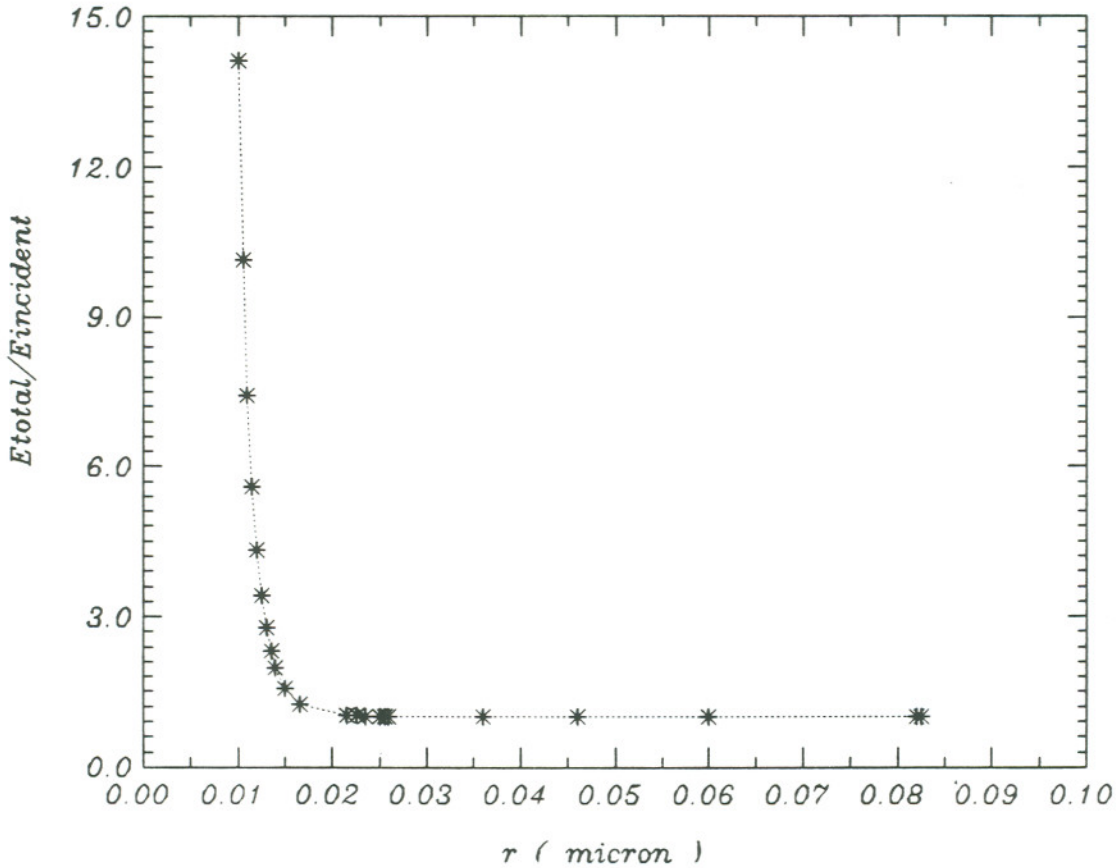

Figure 4.1(b) z polarized field distribution along +y axis

($\theta = 90^0$, $\phi = 90^0$)

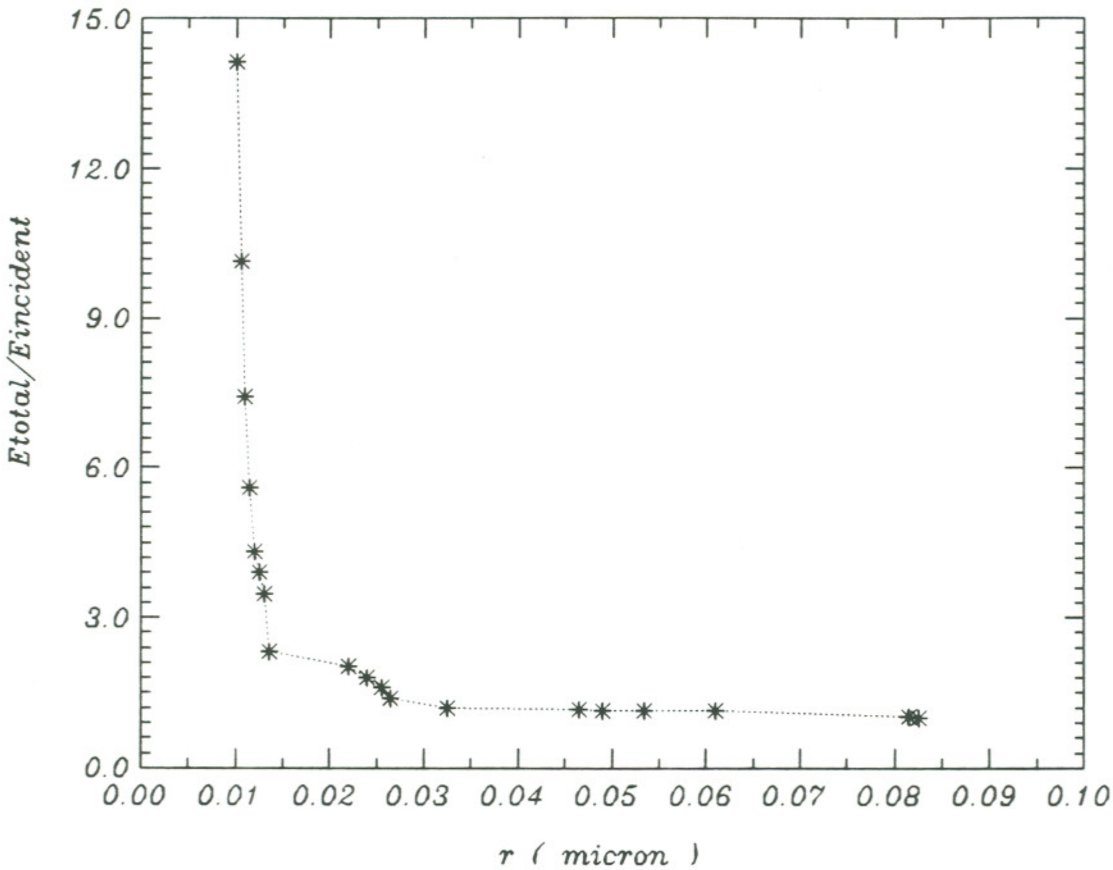

Figure 4.1(c) z polarized field distribution along +x axis
($\theta = 90^0$, $\phi = 0^0$)

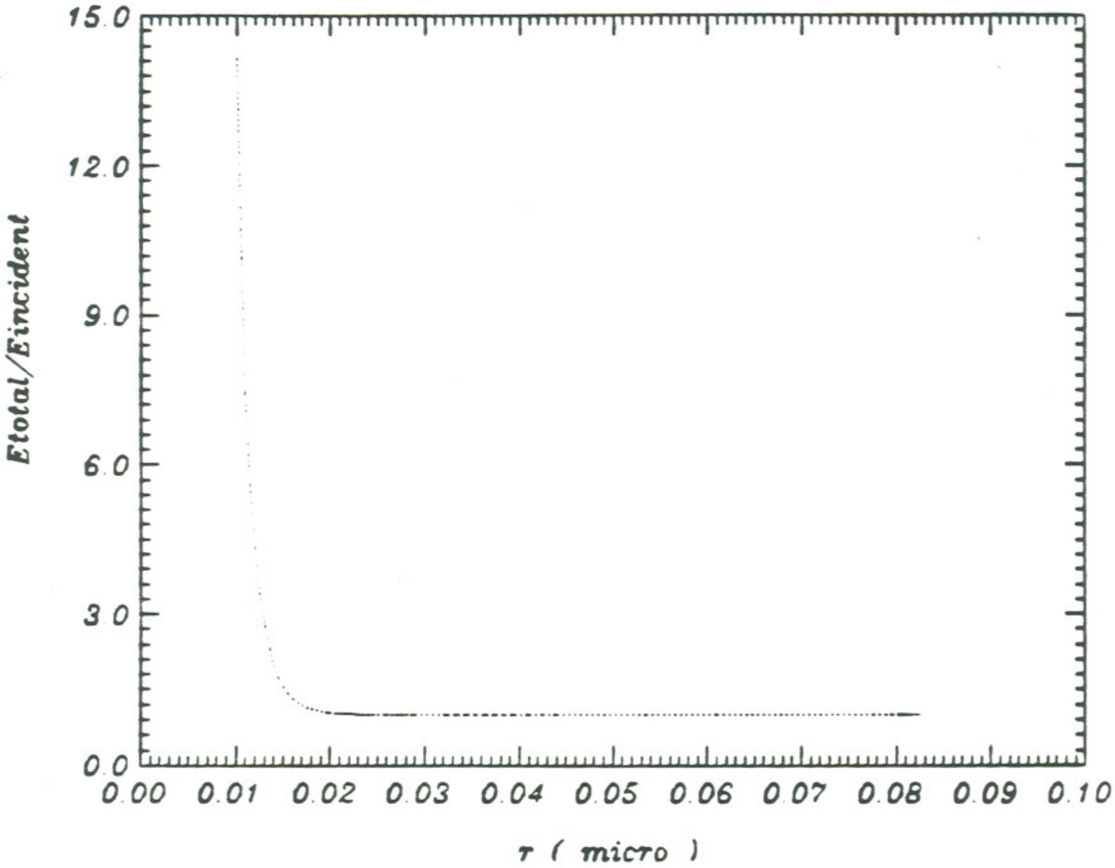

Figure 4.1(d) z polarized field distribution along -y axis
($\theta = 90^0$, $\phi = 270^0$)

Another method to study the distribution of the laser field around the spherical tip of the cone is to compute the fields for various as a function of θ on the surface of the spherical tip. The radius used is $r = 0.01\ \mu$ m, The values of ϕ used were 0^0 , 90^0 , 180^0 and 270^0 and θ ranged from 0^0 to where the surface of the cone and the spherical tip intersect at $\theta = 135^0$. Figure 4.2 shows the E_{total} versus θ for the different ϕ 's. It can be seen that when the θ is close to 135^0 , the field has an unusual manifestation bump at about $\theta = 60^0$. This may be caused by a standing wave generated by the intersection of the spherical tip and cone. It is observed that there is not much difference between the results fro different ϕ 's. This is expected because of the small size of the spherical tip. The total laser power used for the incident beam was 10 μ W.

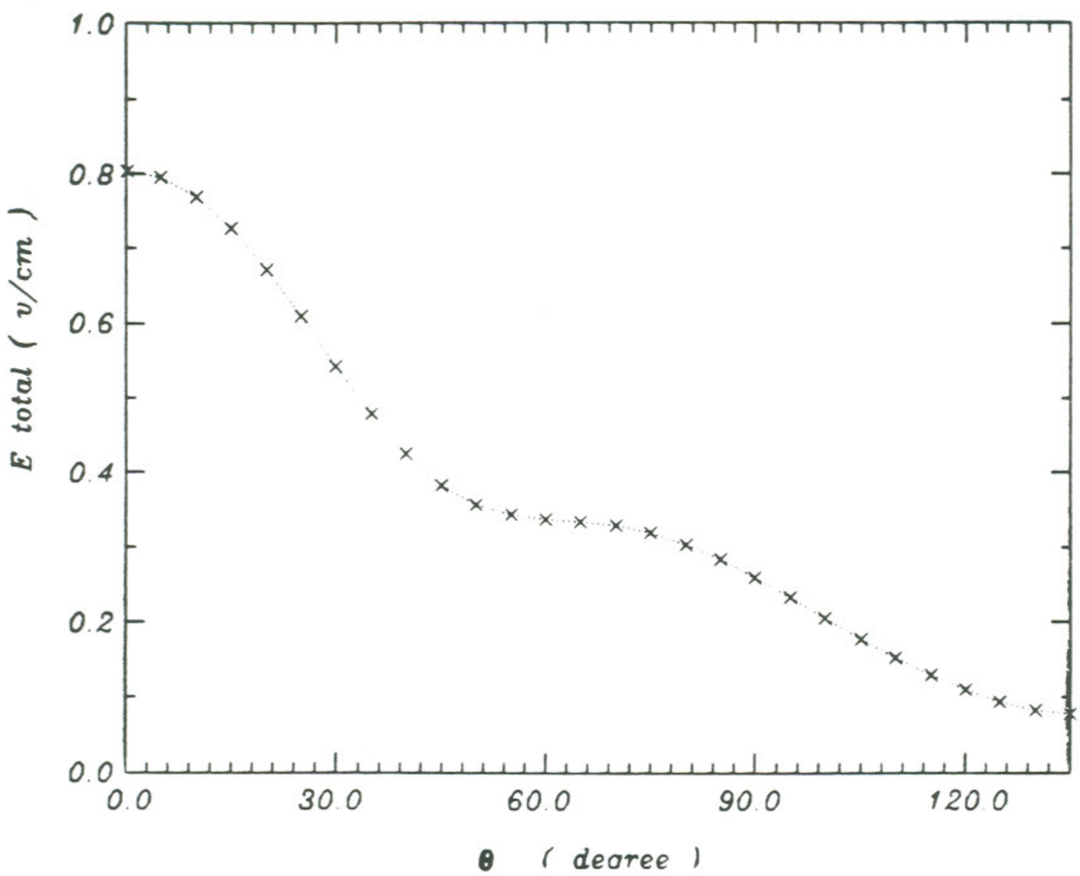

Figure 4.2(a) z polarized field distribution along θ ($\phi=0^0$)

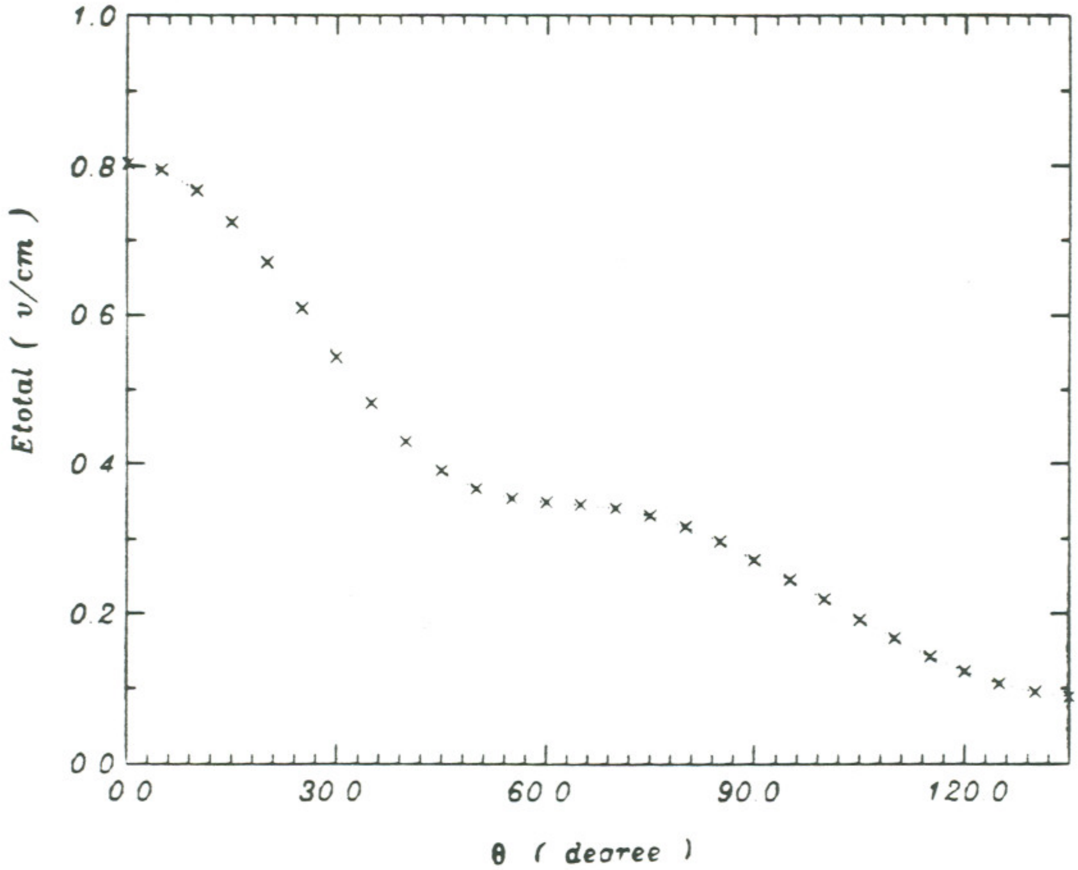

Figure 4.2(b) z polarized field distribution along θ ($\phi=90^0$)

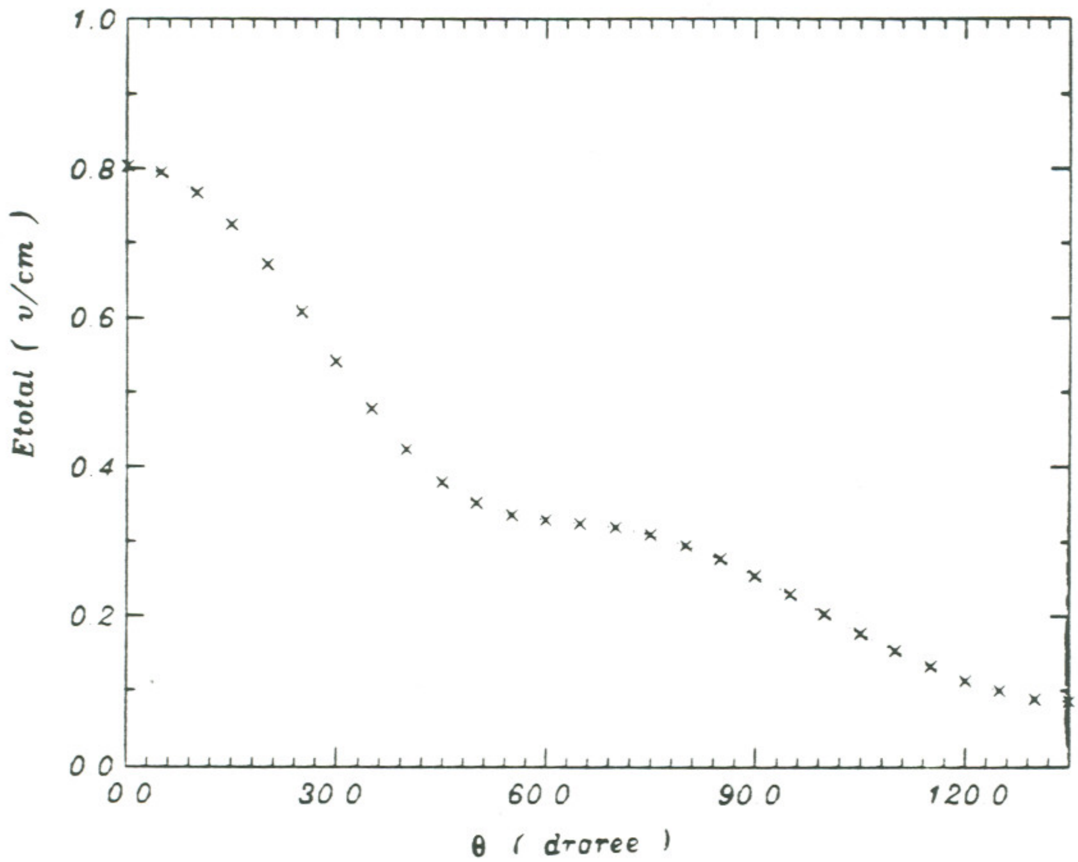

Figure 4.2(c) z polarized field distribution along θ ($\phi=180^0$)

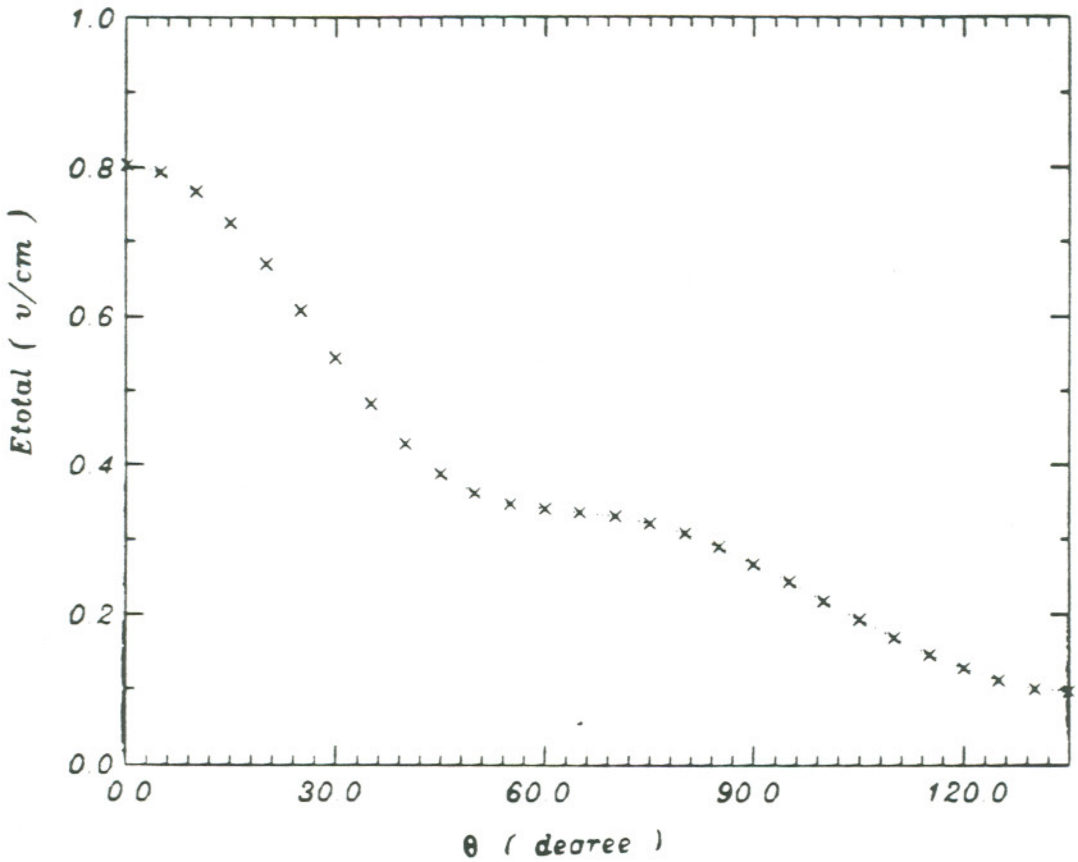

Figure 4.2(d) z polarized field distribution along θ ($\phi=270^{0}$)

Finally, we would like to study the relation between E_{total} and ϕ . Figure 4.3 (a) shows E_{total} versus ϕ . For more clearity, the data shown in Figure 4.3 was redrawn in polar coordinates using ϕ as the polar angle and E_{total} as the radial size in Figure 4.3 (b) .

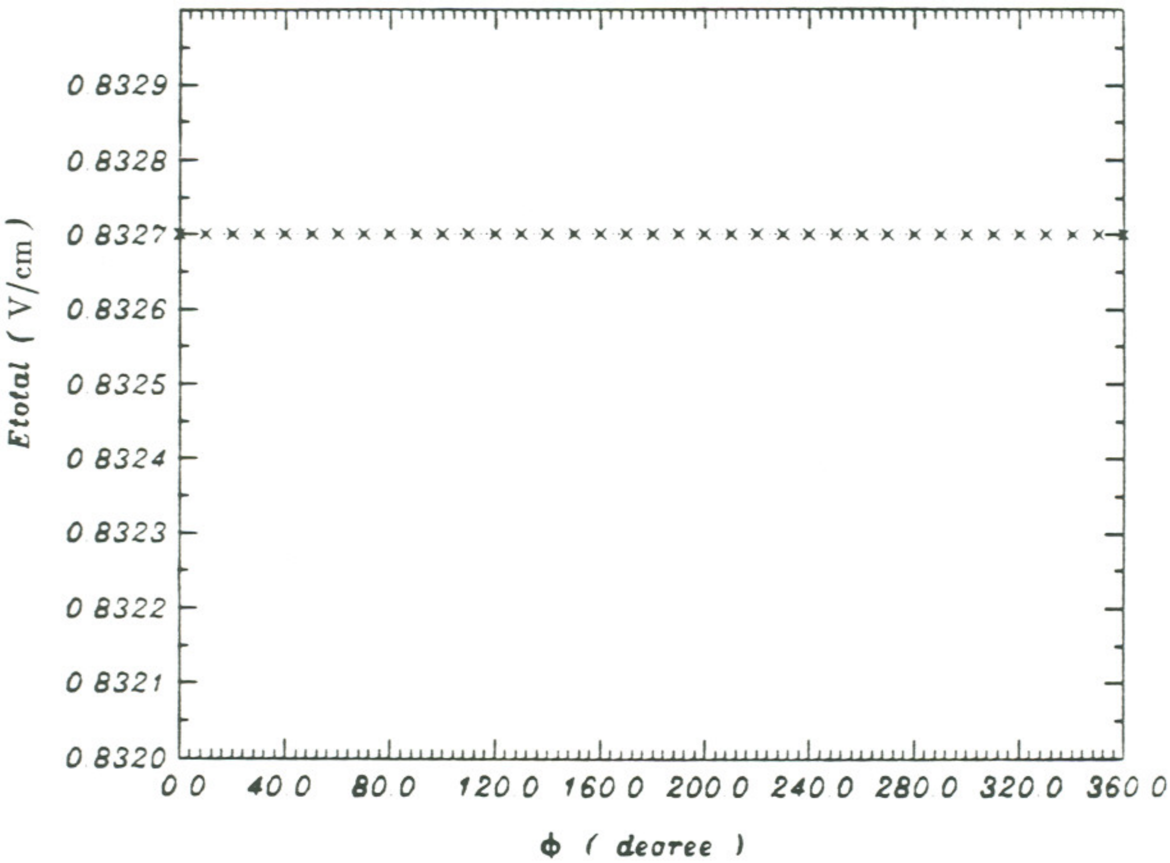

Figure 4.3(a) z polarized field distribution along ϕ (θ=90^0)

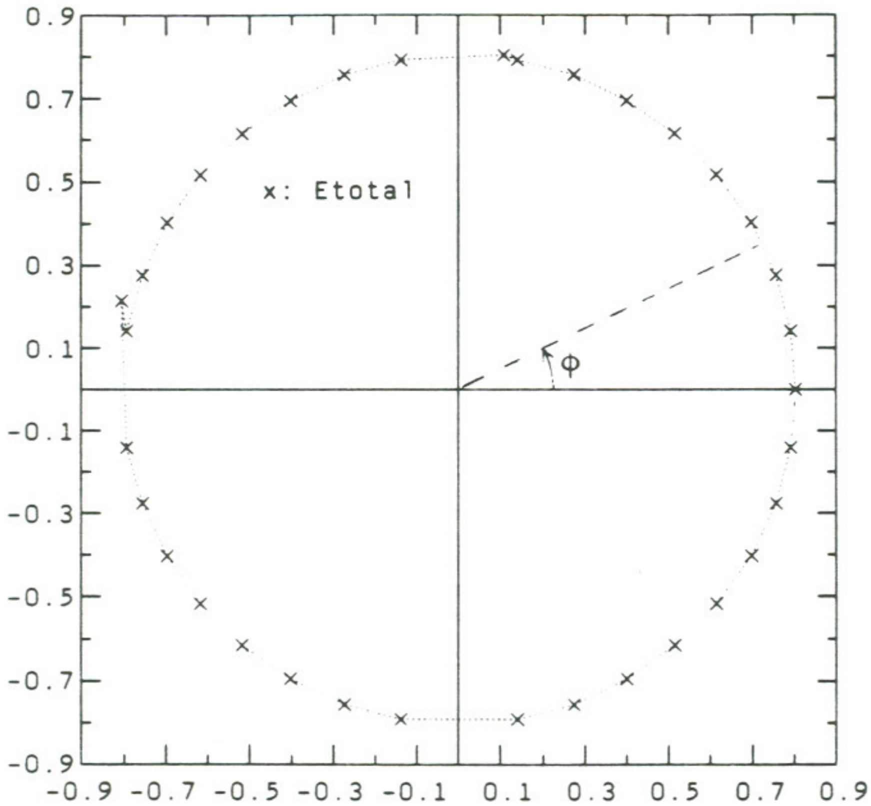

Figure 4.3(b) z polarized field distribution in polar coordinate

(ϕ from 0^0 to 360^0 and $\theta = 90^0$)

4.3 x Polarized Field Distribution

This section repeats for the **x** polarized incident laser beam case. The work done in the previous section for the **z** polarized case. All the coefficients for the incident and scattered fields were computed and are listed in Table 4.5, 4.6, 4.7 and 4.8. They were then used to generate the electric field patterns shown in Figures 4.4 - 4.6 . The results for the **x** polarization are quite similar to those for the **z** polarization though the enhancement appears to be greater for the **x** polarization. The tip radius was again chosen to be 0.01 micron.

Table 4.5

Electric Field Coefficients of Incident Laser Beam A_{pm}

(**x** Polarization)

k	1	2	3	4
p/(m=0)	0.495	1.71	3.12	4.40
Apm(real)	-0.2027d-01	-0.6054d-03	-0.1723d-04	-0.1412d-05
Apm(imag.)	-0.6817d+02	-9.2036d+01	-0.5792d-01	-0.4748d-02
p/(m=1)	1.21	2.49	3.88	5.10
Apm(real)	-0.5686d-02	0.1479d-02	0.2605d-04	0.3279d-06
Apm(imag.)	0.1838d+09	-0.4784d+08	-0.8428d+06	-0.1060d+05
p/(m=2)	2.09	3.31	4.65	5.90
Apm(real)	-0.3105d-01	-0.6582d-01	-0.4022d-03	0.8697d-05
Apm(imag.)	0.2680d+08	0.5681d+08	0.3474d+06	-0.7505d+04
p/(m=3)	3.09	4.14	5.49	6.74
Apm(real)	-0.5130d-01	-0.5951d-01	-0.8270d-03	0.2256d-03
Apm(imag.)	0.1819d+07	0.2111d+07	0.2932d+04	-0.8003d+03

Table 4.5 continued

p/(m=4)	5.09	6.30	7.52	8.83
Apm(real)	-0.1453d+01	-0.7470d-01	-0.1223d-01	-0.7264d-03
Apm(imag.)	0.1003d+06	0.5153d+04	0.8437d+03	0.5010d+02
p/(m=5)	6.01	7.23	8.40	9.70
Apm(real)	-0.3011d+05	-0.8017d+03	-0.1583d+03	-0.5065d+01
Apm(imag.)	0.1401d+05	0.4152d+03	0.8193d+02	0.2622d+01
p/(m=6)	7.08	8.23	9.34	10.59
Apm(real)	-0.7231d+04	0.6120d+02	-0.5123d+01	-0.1579d+01
Apm(imag.)	-0.3771d+05	0.3192d+03	-0.2672d+02	-0.8235d+01
p/(m=7)	8.00	9.15	10.25	11.45
Apm(real)	-0.2068d+04	-0.4365d+03	0.1252d+03	-0.3160d+01
Apm(imag.)	0.9590d+03	0.7807d+02	-0.2239d+02	0.5651d+00
p/(m=8)	8.99	10.09	11.18	12.35
Apm(real)	0.6700d+02	0.6977d+01	0.3847d+01	0.8699d-01
Apm(imag.)	0.1737d+03	0.1809d+02	0.1023d+02	0.2256d+00

Table 4.6

Magnetic Field Coefficients of Incident Laser Beam B_{qn}

(**x** Polarization)

k	1	2	3	4
q/(n=0)	1.20	2.55	3.81	5.20
Bqn(real)	-0.1064d+04	0.1566d+02	-0.2929d+01	0.2051d-02
Bqn(imag.)	0.2258d+11	-0.3321d+09	0.6213d+08	-0.4350d+05
q/(n=1)	1.91	3.20	4.53	5.88
Bqn(real)	0.5710d+00	0.1375d-01	0.1989d-02	0.3100d-03
Bqn(imag.)	0.2257d+08	0.5434d+06	0.7863d+05	0.1255d+05
q/(n=2)	2.80	4.05	5.31	6.61
Bqn(real)	-0.1762d+04	-0.2061d+03	-0.2709d+02	-0.7489d+00
Bqn(imag.)	0.1373d+06	0.1606d+05	0.2110d+04	0.5834d+02
q/(n=3)	3.82	4.95	6.21	7.46
Bqn(real)	-0.7335d+04	-0.4034d+03	0.8298d+02	0.2470d+01
Bqn(imag.)	-0.5186d+04	-0.2852d+03	0.5867d+02	0.1749d+01

Table 4.6 continued

q/(n=4)	4.80	5.85	7.00	8.30
Bqn(real)	-0.2270d+03	0.7074d+01	0.9724d+00	0.4323d-01
Bqn(imag.)	-0.3280d+03	0.1022d+02	0.1406d+01	0.6246d-01
q/(n=5)	5.85	6.87	7.90	9.13
Bqn(real)	0.4810d+04	0.1687d+03	-0.5178d+02	0.2616d+01
Bqn(imag.)	0.6806d+02	0.2387d+01	-0.7327d+00	0.3703d-01
q/(n=6)	6.82	7.80	8.85	10.08
Bqn(real)	0.1016d+04	-0.8910d+02	-0.7723d+01	-0.1977d+00
Bqn(imag.)	-0.8840d+01	0.7752d+00	0.6719d-01	0.1727d-02
q/(n=7)	7.90	8.84	9.87	10.96
Bqn(real)	-0.1339d+05	-0.8837d+02	0.8390d+01	0.2358d+00
Bqn(imag.)	-0.6173d+02	-0.4059d+00	0.3874d-01	0.1089d-02
q/(n=8)	8.92	9.90	10.80	11.90
Bqn(real)	0.1833d+04	-0.9604d+01	0.3661d+01	-0.6217d-01
Bqn(imag.)	-0.4644d+01	0.2430d-01	-0.9262d-02	0.1579d-03

Table 4.7

Electric Field Coefficients of Scattered Laser Beam a_{pm}

(**x** Polarization)

k	1	2	3	4
p/(m=0)	0.495	1.71	3.12	4.40
apm(real)	0.1801d-05	0.9195d-06	0.1213d-07	0.9530d-11
apm(imag.)	-0.4797d-09	-0.9540d-10	-0.3606d-11	-0.2835d-14
p/(m=1)	1.21	2.49	3.88	5.10
apm(real)	-0.6213d+01	0.3163d-01	0.5301d-03	-0.5936d-07
apm(imag.)	0.3641d-02	0.1188d-08	0.2226d-13	-0.1837d-17
p/(m=2)	2.09	3.31	4.65	5.90
apm(real)	0.3949d-01	-0.4564d-03	-0.9362d-06	-0.6634d-11
apm(imag.)	0.2078d-06	-0.1128d-11	-0.1085d-14	-0.7686d-20
p/(m=3)	3.09	4.14	5.49	6.74
apm(real)	0.6077d-05	-0.3722d-08	-0.2129d-10	-0.1918d-15
apm(imag.)	0.2175d-12	-0.1050d-15	-0.6000d-18	-0.5411d-23

Table 4.7 continued

p/(m=4)	5.09	6.30	7.52	8.83
apm(real)	-0.1768d-13	-0.5330d-17	-0.3349d-21	-0.1861d-25
apm(imag.)	-0.2563d-18	-0.7727d-22	-0.4855d-26	0.0d+00
p/(m=5)	6.01	7.23	8.40	9.70
apm(real)	-0.2379d-18	-0.8482d-22	-0.5327d-26	0.0d+00
apm(imag.)	-0.4595d-18	-0.1638d-21	-0.1029d-25	0.0d+00
p/(m=6)	7.08	8.23	9.34	10.59
apm(real)	0.3536d-22	0.1808d-26	0.5032d-30	0.0d+00
apm(imag.)	-0.6781d-23	-0.3476d-27	-0.1025d-31	0.0d+00
p/(m=7)	8.00	9.15	10.25	11.45
apm(real)	-0.3587d-27	-0.2543d-32	0.0d+00	0.0d+00
apm(imag.)	-0.3006d-23	-0.7825d-28	0.0d+00	0.0d+00
p/(m=8)	8.99	10.09	11.18	12.35
apm(real)	0.2503d-28	0.0d+00	0.0d+00	0.0d+00
apm(imag.)	0.2129d-29	0.0d+00	0.0d+00	0.0d+00

Table 4.8

Magnetic Field Coefficients of Scattered Laser Beam b_{qn}

(**x** Polarization)

k	1	2	3	4
q/(n=0)	1.20	2.55	3.81	5.20
bqn(real)	0.7928d+01	-0.6780d+00	0.1310d-03	-0.4705d-07
bqn(imag.)	0.1445d-02	-0.3936d-07	0.6177d-11	-0.2218d-14
q/(n=1)	1.91	3.20	4.53	5.88
bqn(real)	-0.1640d-01	-0.4894d-05	-0.4364d-09	-0.9496d-13
bqn(imag.)	-0.2154d-07	0.1234d-12	0.1104d-16	0.2402d-20
q/(n=2)	2.80	4.05	5.31	6.61
bqn(real)	-0.8996d-07	-0.1082d-09	-0.1239d-13	-0.6283d-18
bqn(imag.)	-0.1155d-08	-0.1389d-11	-0.1591d-15	-0.8065d-20
q/(n=3)	3.82	4.95	6.21	7.46
bqn(real)	-0.6331d-12	-0.1150d-14	0.5599d-19	0.6963d-23
bqn(imag.)	0.8955d-12	0.1627d-14	-0.7918d-19	-0.9849d-23

Table 4.8 continued

q/(n=4)	4.80	5.85	7.00	8.30
bqn(real)	-0.4647d-17	-0.7802d-20	-0.1147d-23	0.1188d-27
bqn(imag.)	0.3216d-17	0.5369d-20	0.7938d-24	-0.8225d-28
q/(n=5)	5.85	6.87	7.90	9.13
bqn(real)	-0.2055d-21	0.2843d-24	-0.4420d-28	0.0d+00
bqn(imag.)	0.1452d-19	-0.2009d-22	0.3124d-26	0.0d+00
q/(n=6)	6.82	7.80	8.85	10.08
bqn(real)	-0.1075d-26	-0.2589d-30	0.0d+00	0.0d+00
bqn(imag.)	-0.1235d-24	-0.3802d-29	0.0d+00	0.0d+00
q/(n=7)	7.90	8.84	9.87	10.96
bqn(real)	0.3759d-29	0.0d+00	0.0d+00	0.0d+00
bqn(imag.)	-0.2947d-28	0.0d+00	0.0d+00	0.0d+00
q/(n=8)	8.92	9.90	10.80	11.90
bqn(real)	0.0d+00	0.0d+00	0.0d+00	0.0d+00
bqn(imag.)	0.0d+00	0.0d+00	0.0d+00	0.0d+00

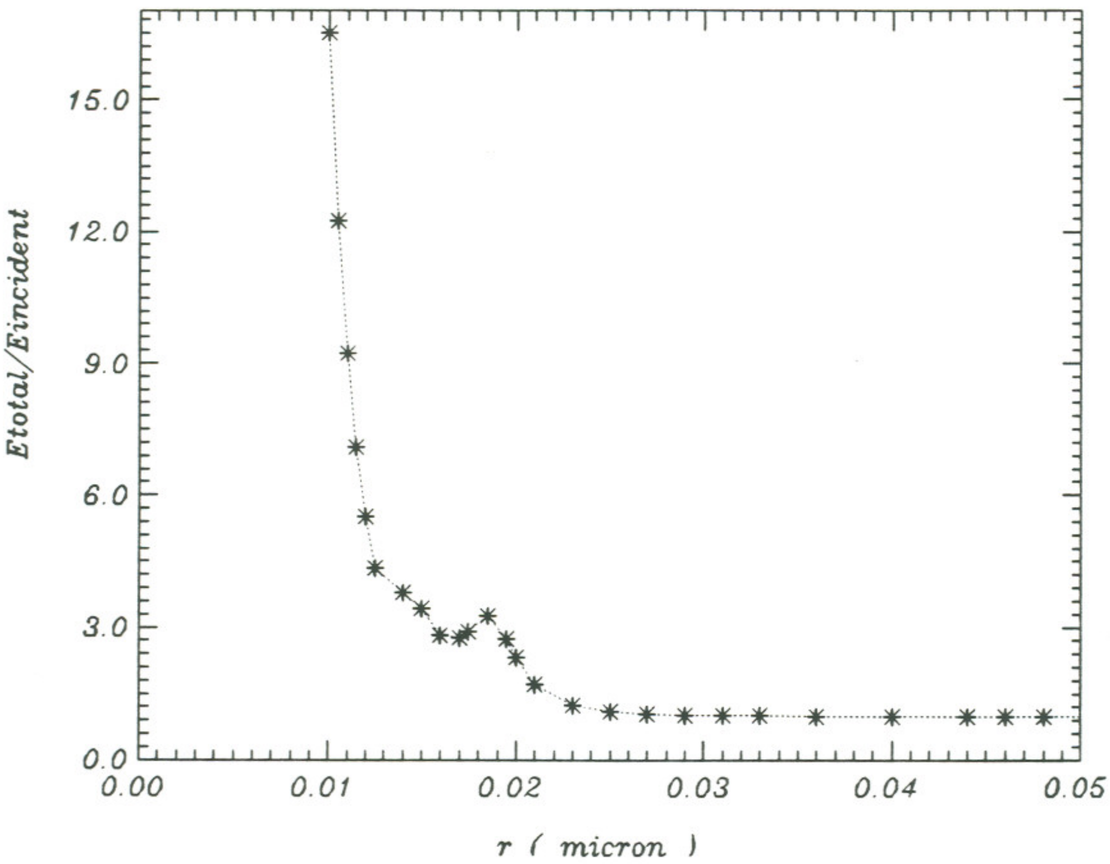

Figure 4.4(a) x polarized field distribution along +x axis

($\theta = 90^0$ and $\phi=0^0$)

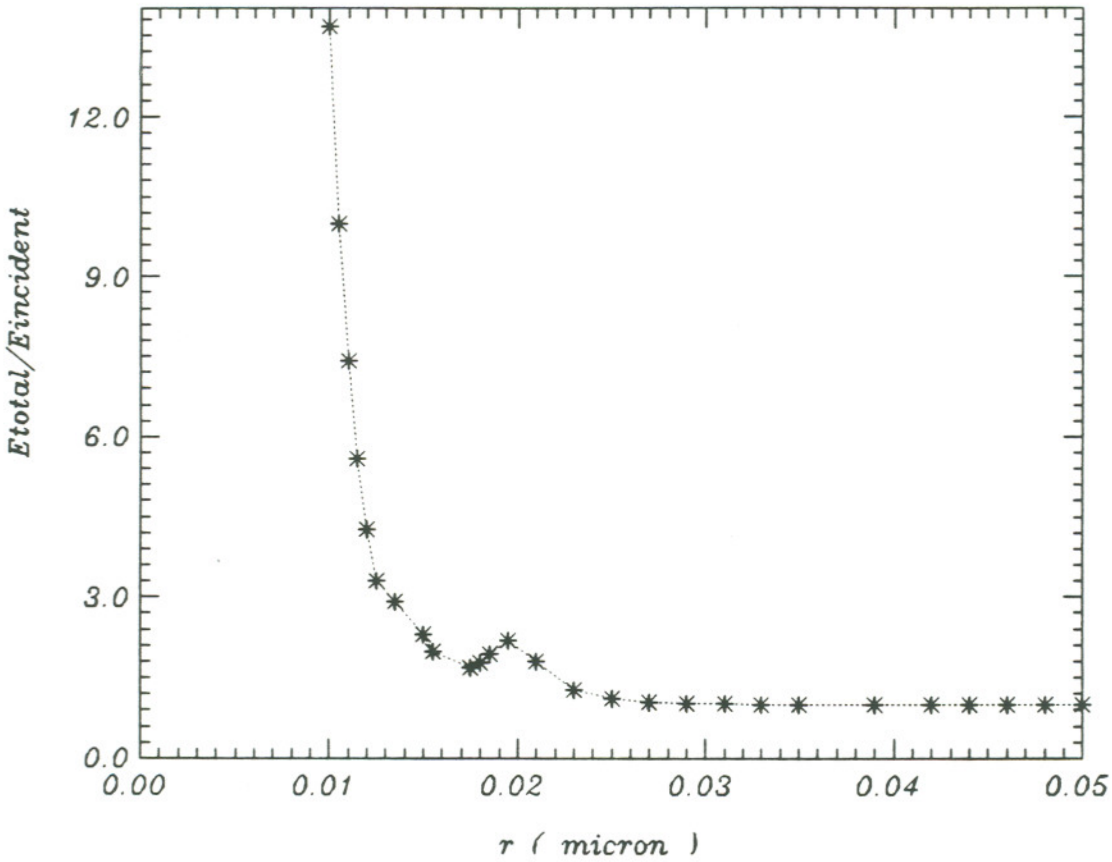

Figure 4.4(b) x polarized field distribution along +y axis

($\theta = 90^0$ and $\phi = 90^0$)

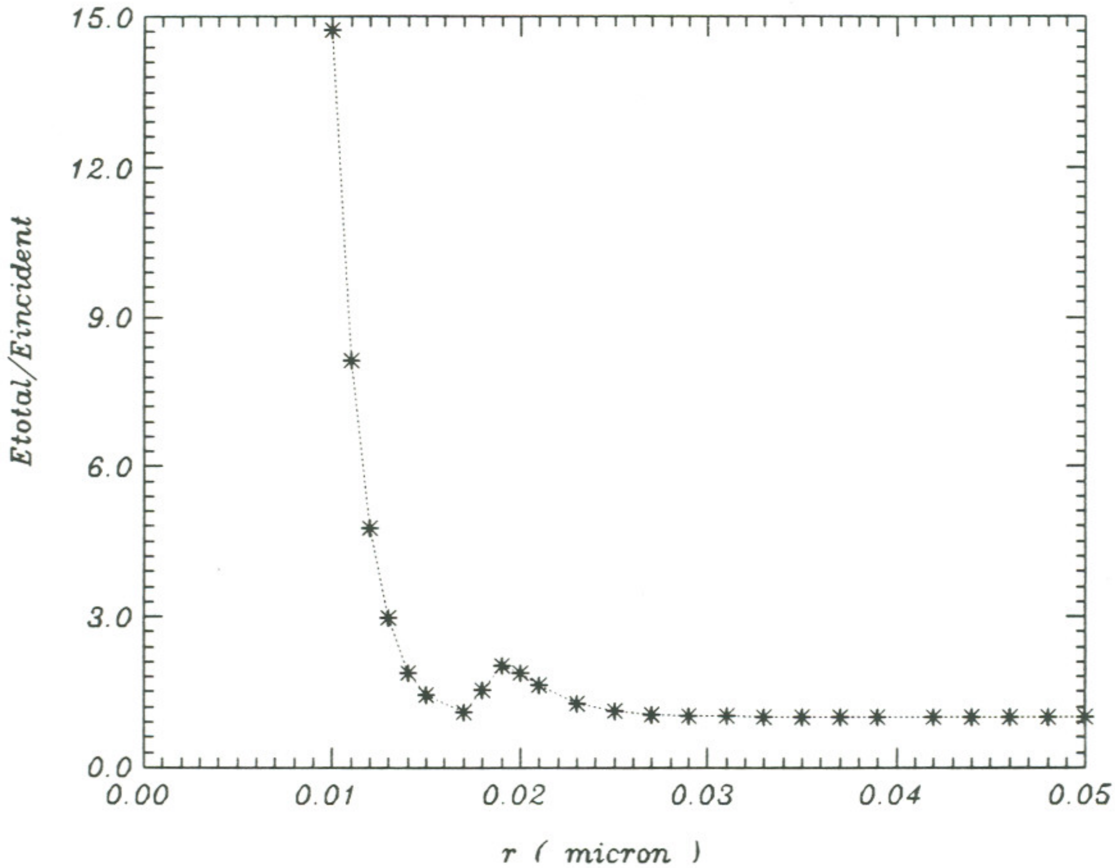

Figure 4.4(c) x polarized field distribution along -x axis

($\theta = 90^0$, $\phi = 180^0$)

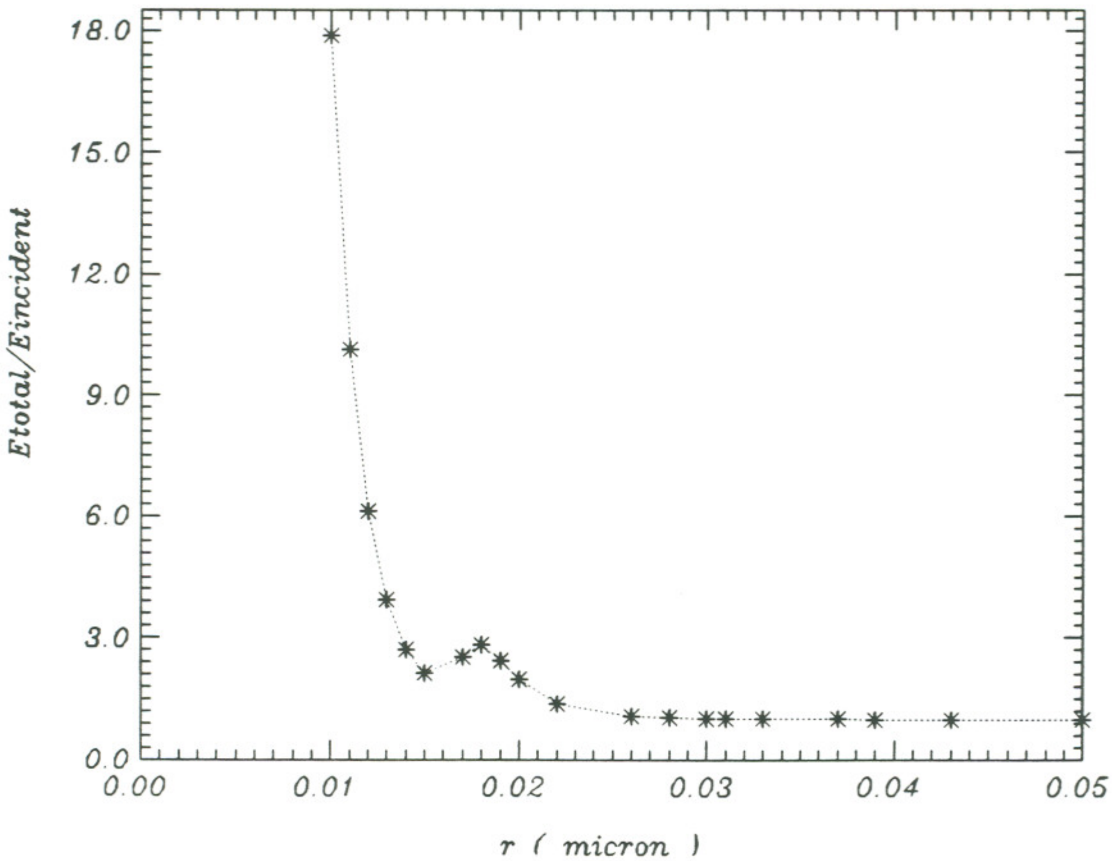

Figure 4.4(d) x polarized field distribution along -y axis

($\theta = 90^0$, $\phi = 270^0$)

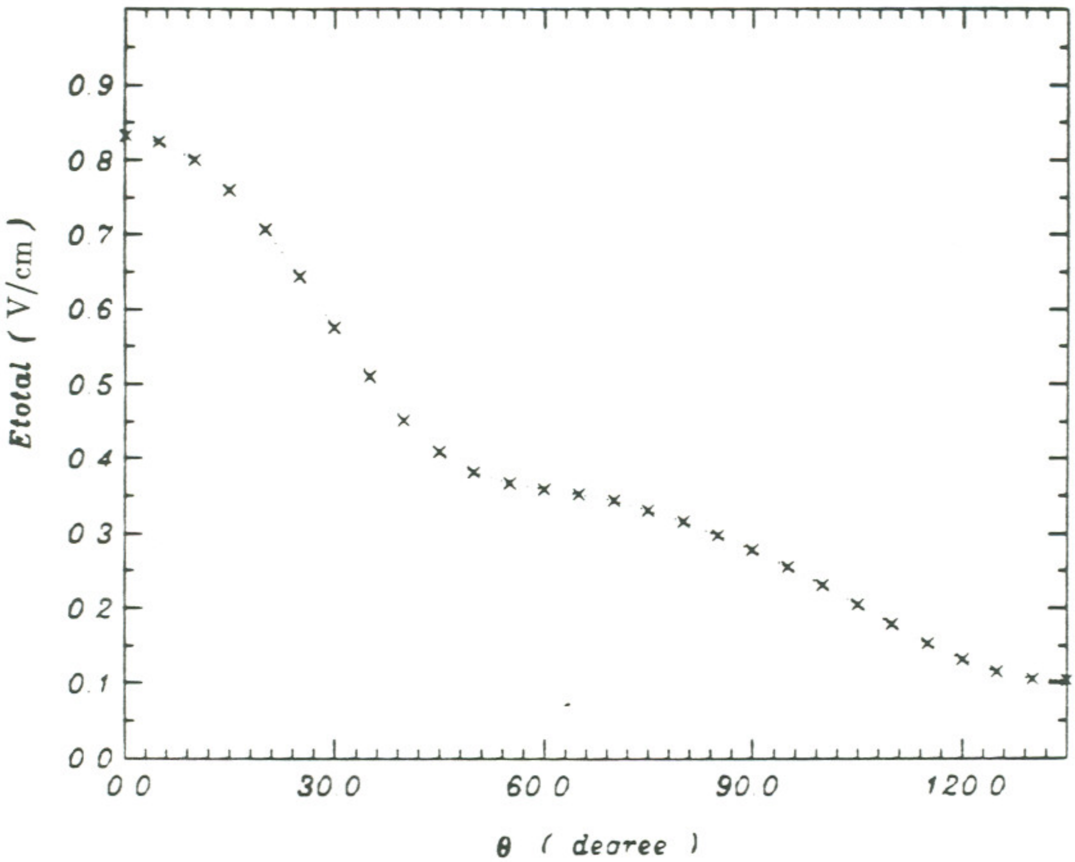

Figure 4.5(a) x polarized field distribution along θ ($\phi=0^0$)

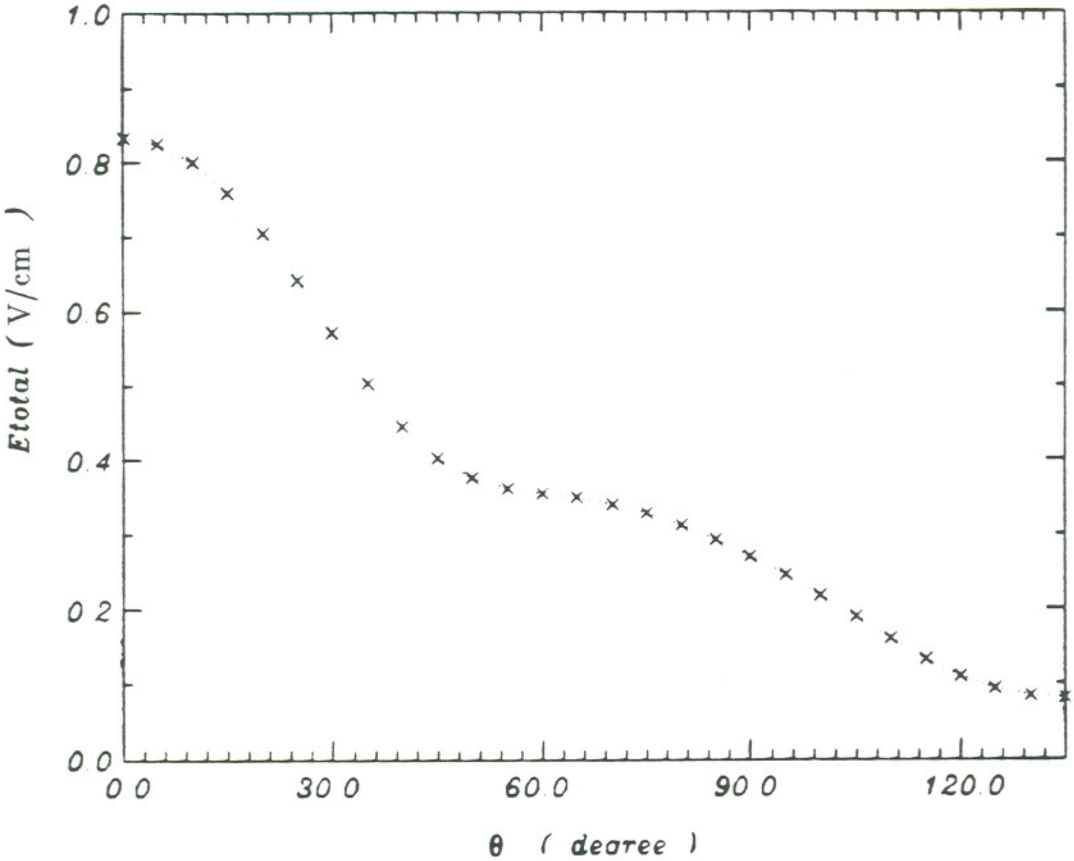

Figure 4.5(b) x polarized field distribution along θ ($\phi=90^0$)

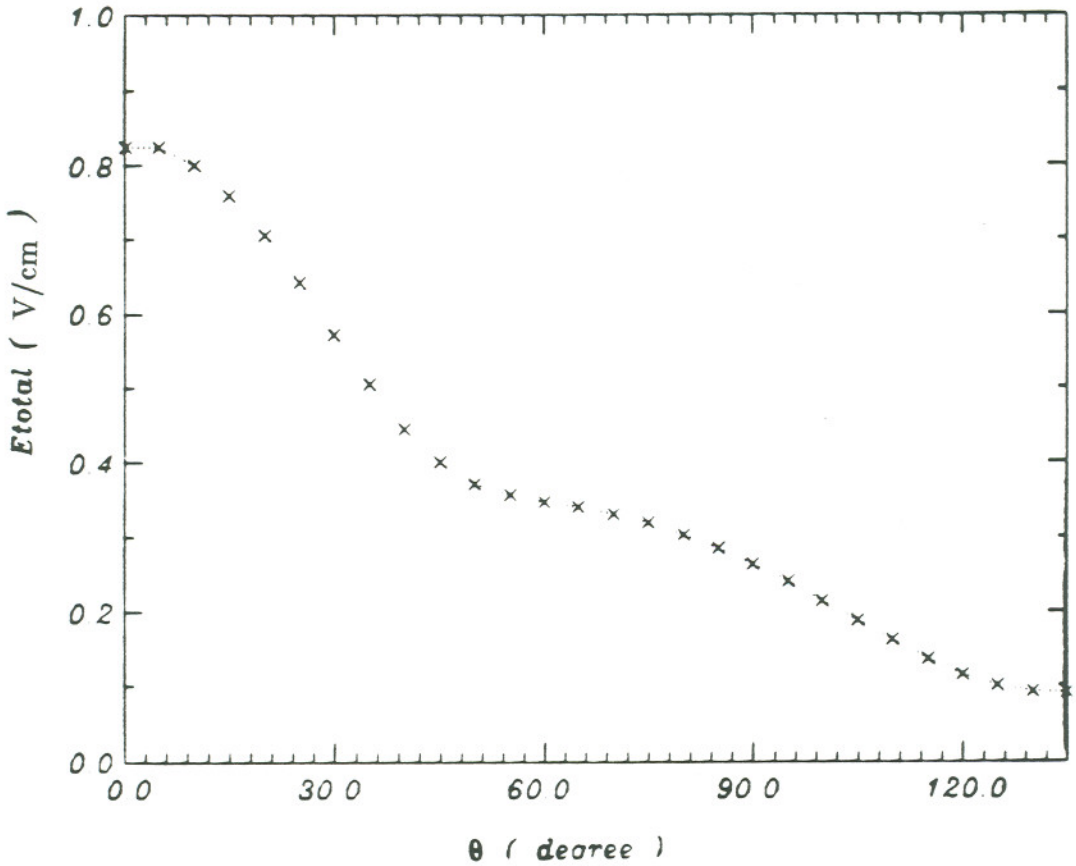

Figure 4.5(c) x polarized field distribution along θ ($\phi=180^0$)

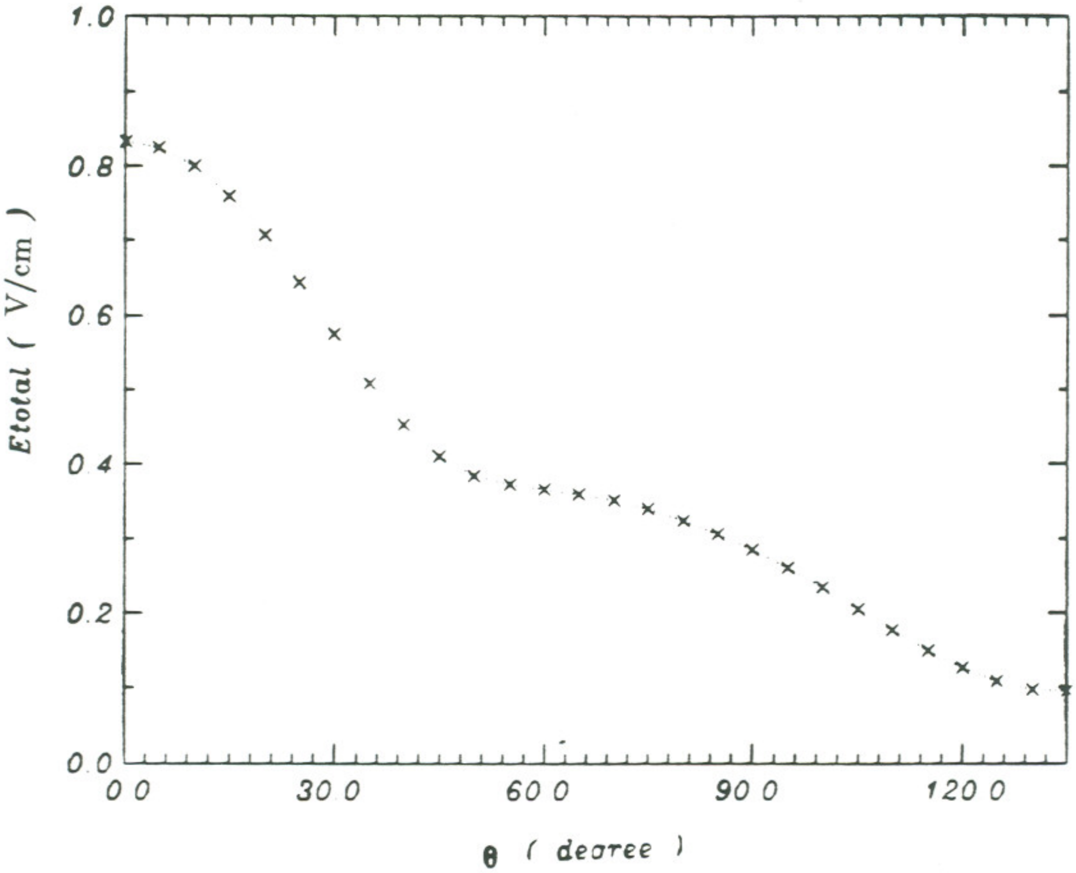

Figure 4.5(d) x polarized field distribution along θ ($\phi=270^0$)

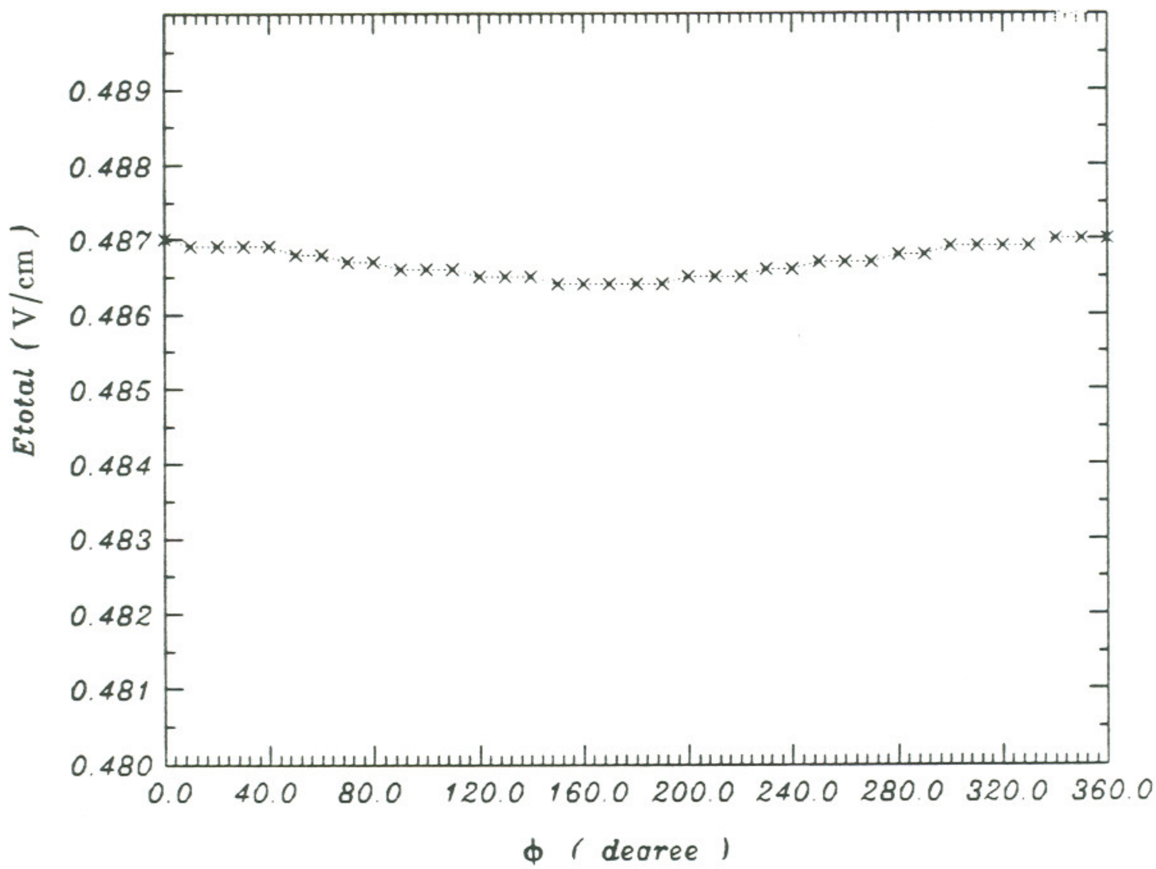

Figure 4.6 x polarized field distribution along ϕ ($\theta = 90°$)

4.4 Near and Far Field Approximations

In the work that follows, we are going to make the approximation that $kr << 1$ for the near field and $kr >> 1$ for the far field. We would like to study the electric field enhancement on the spherical tip surface versus the tip radius r and also the far field intensity pattern versus ϕ for $\theta = 90^0$.

When $\theta = 90^o$, the associated Legendre function is:

$$P_p^m(0)=\frac{2^m\cos[\frac{1}{2}\pi(p+m)]\Gamma(\frac{1}{2}p+\frac{1}{2}m+\frac{1}{2})}{\sqrt{\pi}\Gamma(\frac{1}{2}p-\frac{1}{2}m+1)} \tag{4.12}$$

This will be used for both the near field and far field approximations.

4.4.1 Near Field Approximation

The spherical Bessel functions j_p (kr) and $h_p^{(2)}$ (kr) have their approximate formulae when $kr << 1$. They are[121]:

$$j_p=\frac{(kr)^p}{(2p+1)!!} \tag{4.13}$$

$$h_p^{(2)}=\frac{(kr)^p}{(2p+1)!!}+j\,(2p-1)!!(kr)^{-p-1} \tag{4.14}$$

Using equations (4.12), (4.13) and (4.14), the field components (4.7), (4.8), and (4.9), for lowest order, can be simplied as:

$$E_r = \frac{1}{r} p(p+1) \times \left[A_p j_p(kr) + a_p h_p^{(2)}(kr) \right] P_p(0) e^{j\phi} \tag{4.15}$$

$$E_\theta = \frac{\omega\mu}{\sin\theta} \times \left[B_q j_q(kr) + b_q h_q^{(2)}(kr) \right] P_q(0) e^{j\phi} \tag{4.16}$$

$$E_\phi = \frac{j}{r} \left\{ A_p \left[j_p(kr) + krj_p'(kr) \right] + a_p \left[h_p^{(2)}(kr) + krh_p^{(2)'}(kr) \right] \right\} \times \frac{P_p(0)}{\sin\theta} e^{j\phi} \tag{4.17}$$

where A_p , B_q , a_p and b_q can be taken from Table 4.5, 4.6, 4.7 and 4.8 using the $m = 0$ values.

We next will find the electric field enhancement as a function of the radius "a" of the spherical tip. Taking a from 0.0016 to 0.0080 micron, i.e., $kr = 1/50$ to $1/10$ and using equations (4.15) and (4.11), the electric field enhancement was generated as shown in Figure 4.7 as a function of tip radius. Only equation (4.15) is needed because E_θ and E_ϕ are zero on the surface of the sphere.

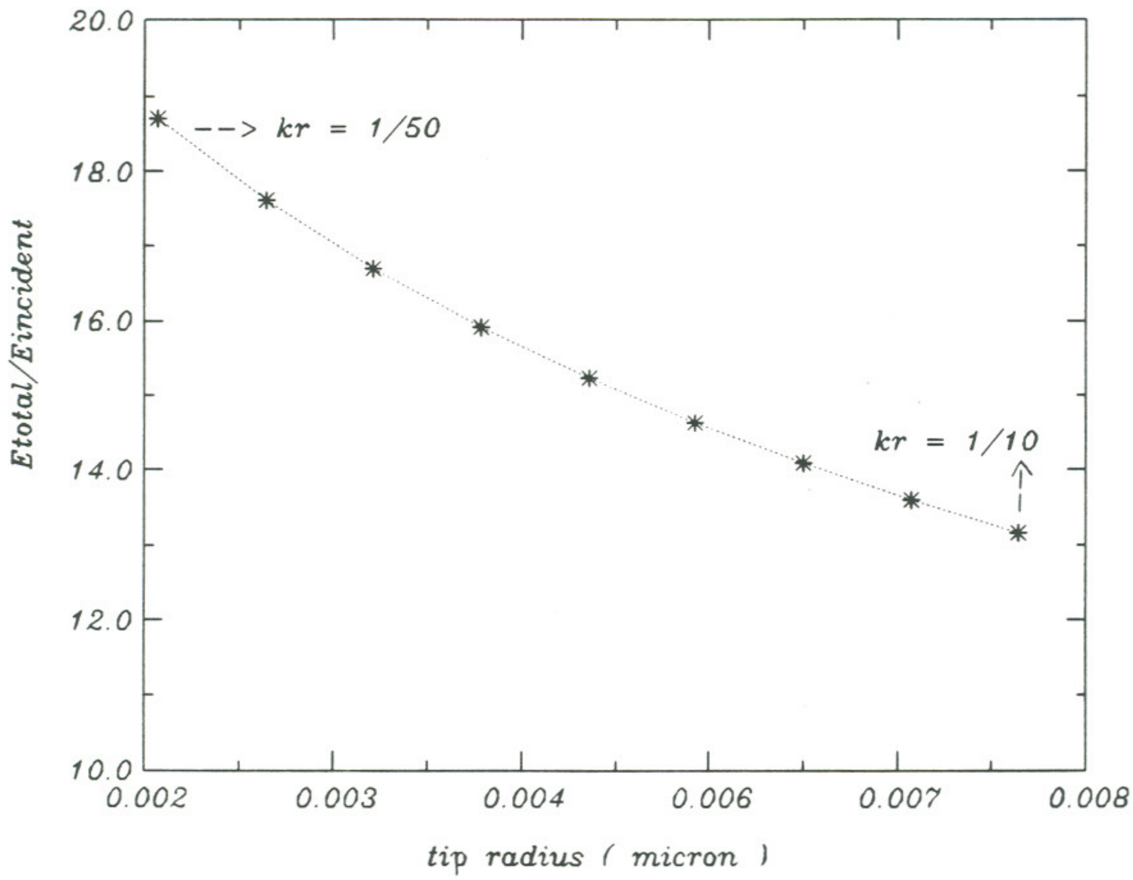

Figure 4.7 Near field enhancement

4.4.2 Far Field Approximation

For kr >> 1, we can take the spherical Bessel functions as[121]:

$$j_p(kr)=\frac{1}{kr}\ \sin(kr - \frac{p\pi}{2}) \tag{4.18}$$

$$h_p^{(2)}=\frac{j}{kr}\times\left[\cos(kr-\frac{p\pi}{2}) - j\sin(kr-\frac{p\pi}{2})\right] \tag{4.19}$$

These two formulae and equation (4.12) can be used to make approximation in equations (4.7), (4.8) and (4.9) . Remember that we have the relation between the field to intensity as[118]:

$$I=\frac{c\epsilon_0}{2}\ \mathbf{E}\cdot\mathbf{E}^* \tag{4.20}$$

so we can get the intensity of the far field distributions.

We chose kr = 10, 50, 100, 1000 and generated the plots of intensity I versus polar angle ϕ shown in Figures 4.8(a), (b), (c) and (d). For the smaller values of kr, there is diffraction around the tip. However for larger values of kr, the cone-sphere procedures a shadow. These results will be compared to some experimental results in Chapter 5.

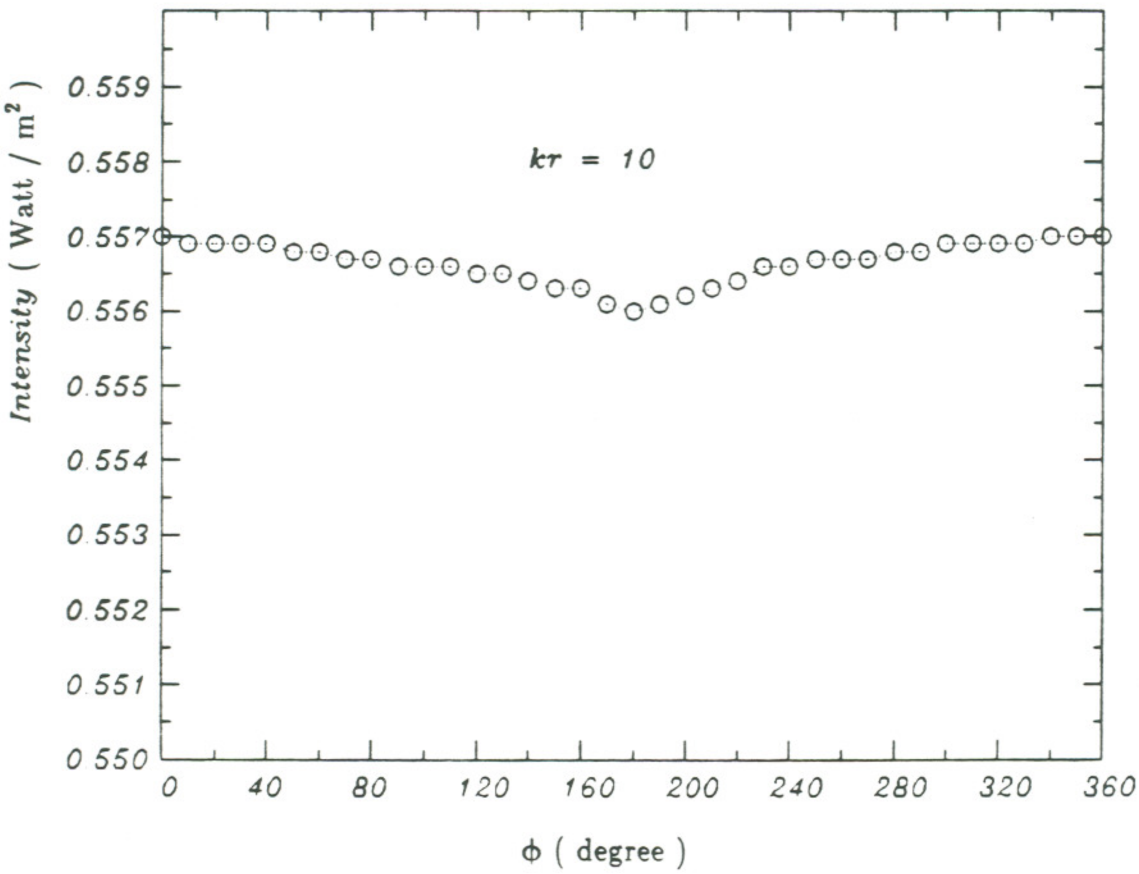

fig 4.8(a) The far field intensity distribution (kr = 10)

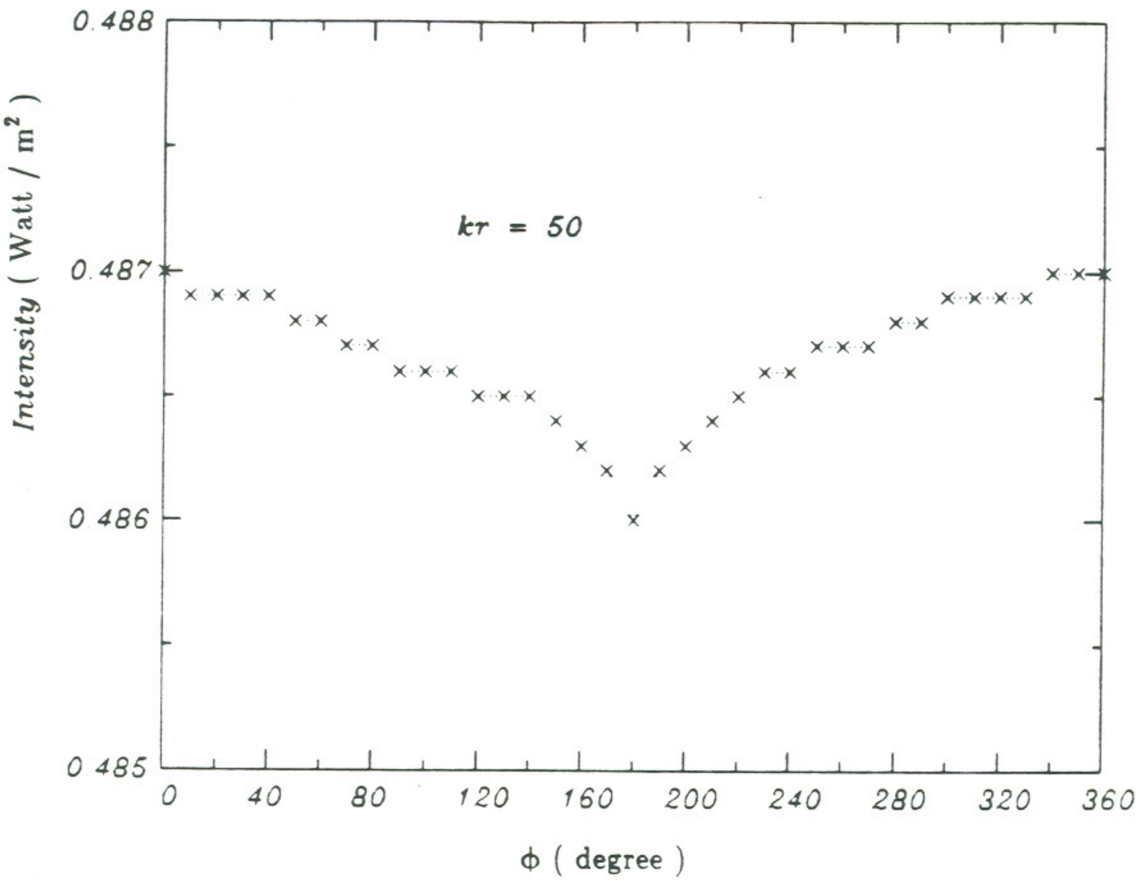

Figure 4.8(b) The far field intensity distribution (kr = 50)

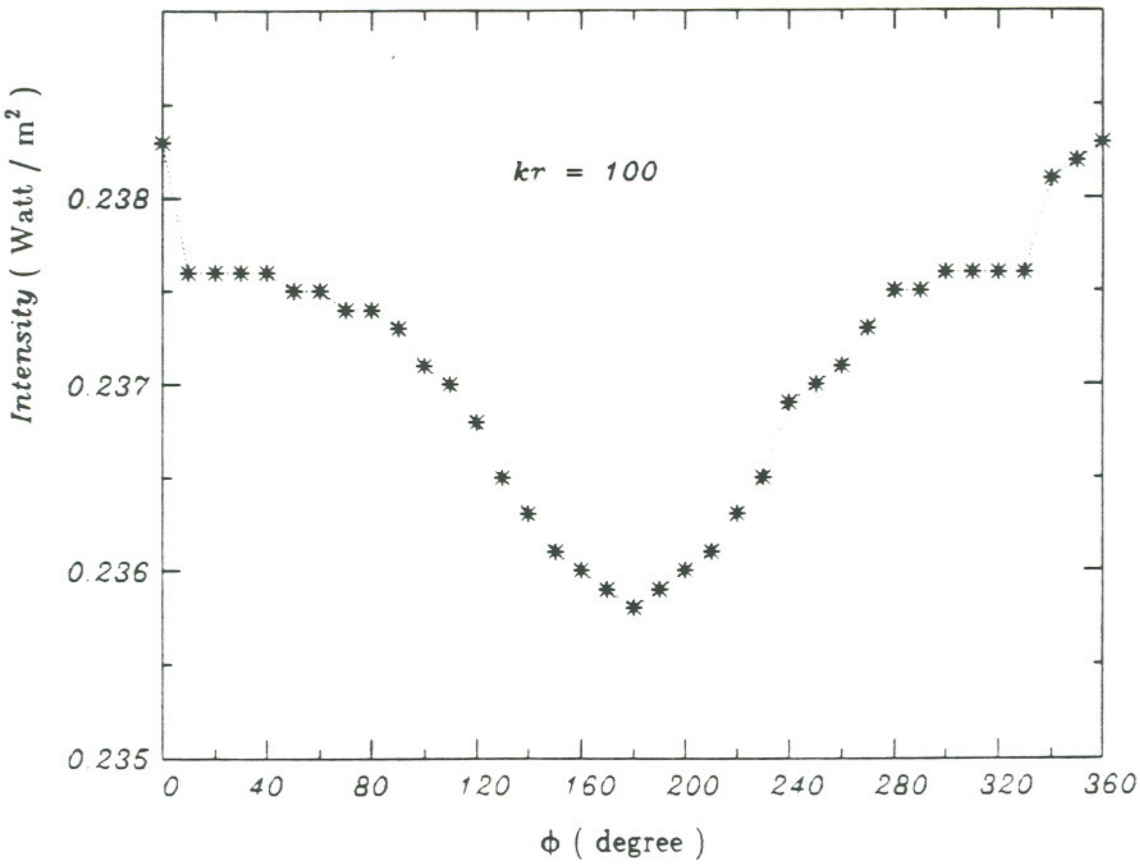

Figure 4.8(c) The far field intensity distribution (kr = 100)

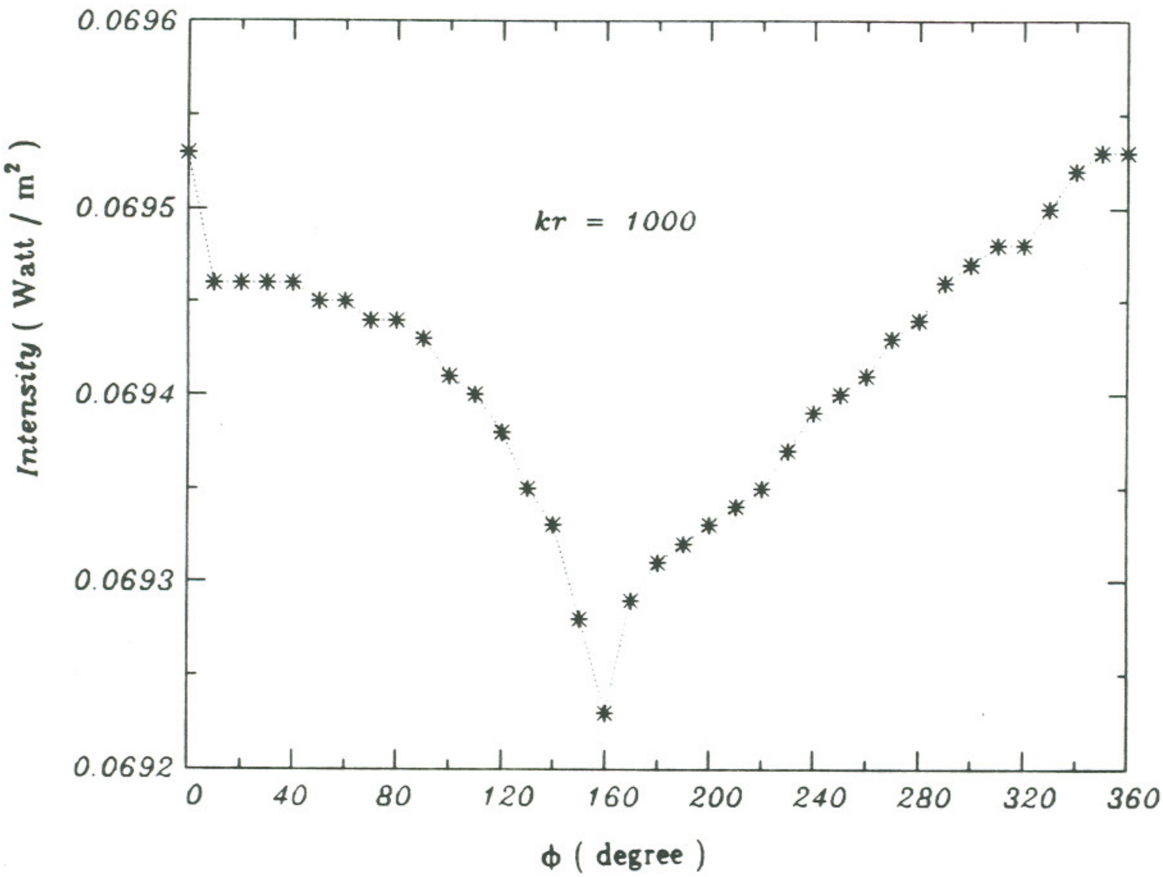

Figure 4.8(d) The far field intensity distribution (kr = 1000)

4.5 A Simple Comparison

We would like to compare our results for the sphere tipped cone with the results for a plane wave scattering from a sphere. Since for the sphere size is small, we should get similar results.

It well known that an incident plane electromagnetic wave can be expressed as[13]:

$$\mathbf{E_i}(\mathbf{r})=\mathbf{E_0}(\mathbf{r})e^{-jky} \tag{4.21}$$

We assume that the incident field is **z** polarized and propagating along the **y** axis. So in spherical coordinates, it is:

$$\mathbf{E_i}(r,\theta,\phi)=E_0(\cos\theta\,\mathbf{r_0}-\sin\theta\,\boldsymbol{\theta}_0)e^{-jky} \tag{4.22}$$

In Chapter 3, from equations (3.25) -- (3.30), we know that the components of an electromagnetic field are related to the Hertz Potentials Π and Π^*. Considering our small sphere, in spherical coordinates, if we choose the origin to be at the center of the sphere, then Π and Π^* can be expanded as:

For the incident field,

$$\Pi_i=\sum_{l}^{\infty}\sum_{m}A_{lm}\ r\ j_l(kr)P_l^{m}(\cos\theta)e^{jm\phi} \tag{4.23}$$

$$\Pi_i^* = \sum_{l}^{\infty}\sum_{m} B_{lm}\ r\ j_l(Kr) P_l^m(\cos\theta) e^{jm\phi} \tag{4.24}$$

For the scattered field,

$$\Pi_s = \sum_{l}^{\infty}\sum_{m} a_{lm}\ r\ h_l^{(2)}(kr) P_l^m(\cos\theta) e^{jm\phi} \tag{4.25}$$

$$\Pi_s^* = \sum_{l}^{\infty}\sum_{m} b_{lm}\ r\ h_l^{(2)}(kr) P_l^m(\cos\theta) e^{jm\phi} \tag{4.26}$$

The boundary conditions require that the tangential components of the electric field to be zero on the surface of the sphere[140] so that

$$[E_\theta = E_\phi]_{r=a} = 0 \tag{4.27}$$

Substituting equations (4.23) -- (4.26) and use the boundary conditions in equations (3.25) -- (3.30) in Chapter 3, we get the results for the field scattered by a conducting sphere:

$$E_r = \frac{\cos\phi}{(kr)^2}\sum_{l}^{\infty}\frac{2l+1}{l(l+1)}\left[A_l\ r\ j_l(kr) + a_l\ r\ h_l^{(2)}(kr)\right]P_l(\cos\theta) \tag{4.28}$$

$$E_\theta = \frac{\cos\phi}{kr}\sum_{l}^{\infty}\frac{2l+1}{l(l+1)}\left\{\left[A_l kr j_l'(kr) + a_l kr h_l^{(2)'}(kr)\right]\sin\theta\frac{dP_l(\cos\theta)}{d\theta}\right.$$
$$\left. -j\left[B_l r j_l(kr) + b_l r h_l^{(2)}(kr)\right]\frac{P_l(\cos\theta)}{\sin\theta}\right\} \tag{4.29}$$

$$E_\phi = -\frac{\sin\phi}{kr}\sum_l \frac{2l+1}{l(l+1)}\left\{\left[A_l krj_l'(kr) + a_l krh_l^{(2)'}(kr)\right]\frac{P_l(\cos\theta)}{\sin\theta}\right.$$
$$\left. -j\left[B_l rj_l(kr)+b_l rh_l^{(2)}(kr)\right]\sin\theta\frac{dP_l(\cos\theta)}{d\theta}\right\} \quad (4.30)$$

Several coefficients were generated by numerical computation. They are listed in Table 4.9 .

We can get the total field magnitude from (4.28) -- (4.30) and using

$$|E|_{total} = \sqrt{E_r^2+E_\theta^2+E_\phi^2} \quad (4.31)$$

Figure 4.9 shows the electric field enhancement versus r for both problems. Near the surface of the sphere, the field enhancement of the plane wave is almost identical to that the focused laser beam, cone-sphere case. But in the range of 0.1 μ m $< r <$ 0.4 μ m , the results are somewhat different. Of course far from the sphere or tip, the enhancement is unity for both problems. i.e., there is no enhancement.

Table4.9

Electric Field Coefficients of Plane Wave

(s- Polarization)

l	A_l	B_l	a_l	b_l
1	-0.209d+03	0.249d+04	0.478d-02	-0.289d+01
2	-0.527d+01	-0.288d+02	0.958d-03	0.919d+00
3	-0.285d+00	0.796d+01	0.221d-03	-0.316d-01
4	-0.134d-01	-0.135d+00	0.979d-04	0.516d-03

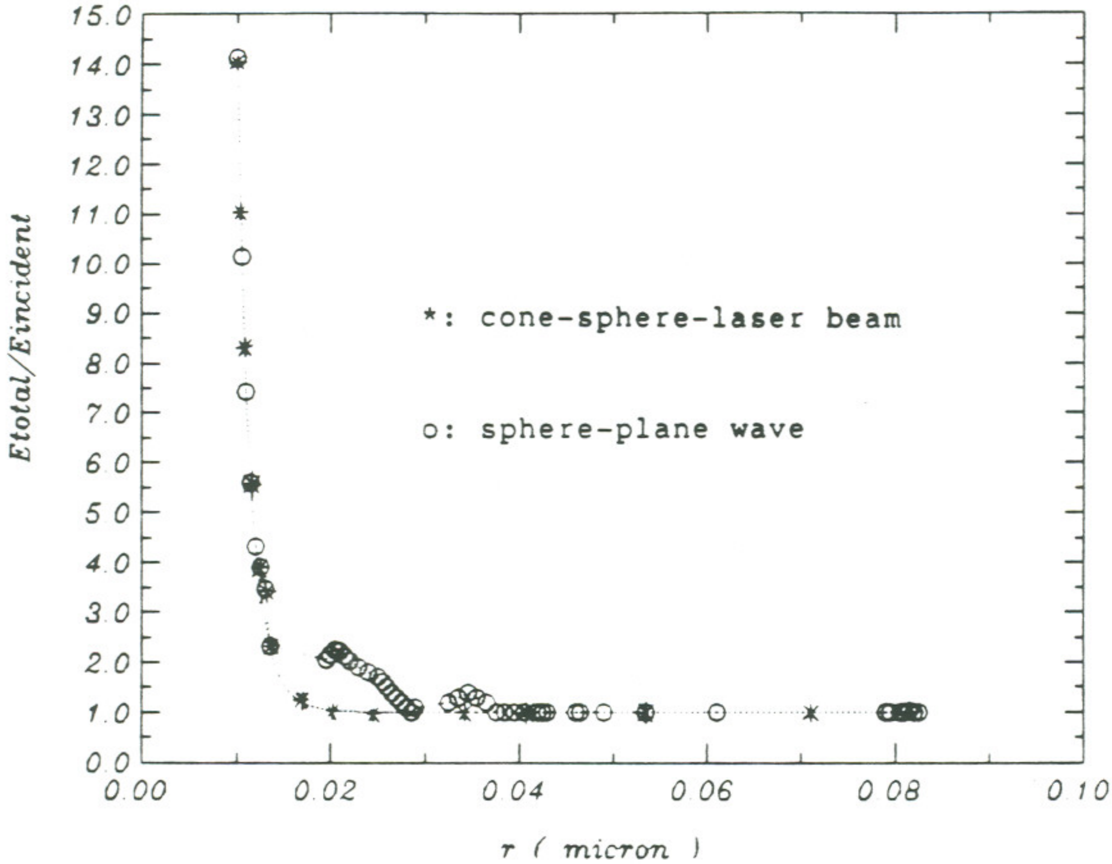

Fig 4.9 The near field enhancement

($\theta = 0.1^\circ$, $\phi = 0^\circ$)

Figure 4.10, shows the total electric field as a function of θ for $\phi = 0^0$. The beam wave and plane wave cases show difference. The scattered plane wave has some oscillations that the scattered beam wave does not.

In the far field, because the sphere is quite a bit smaller that the wavelength, the plane wave result will not be effected by the sphere. However, the cone is large with respect to the wavelength and the far field pattern for the beam wave case will be strongly effected by the sphere tipped cone. Consequently, the field pattern for the two cases are not comparable.

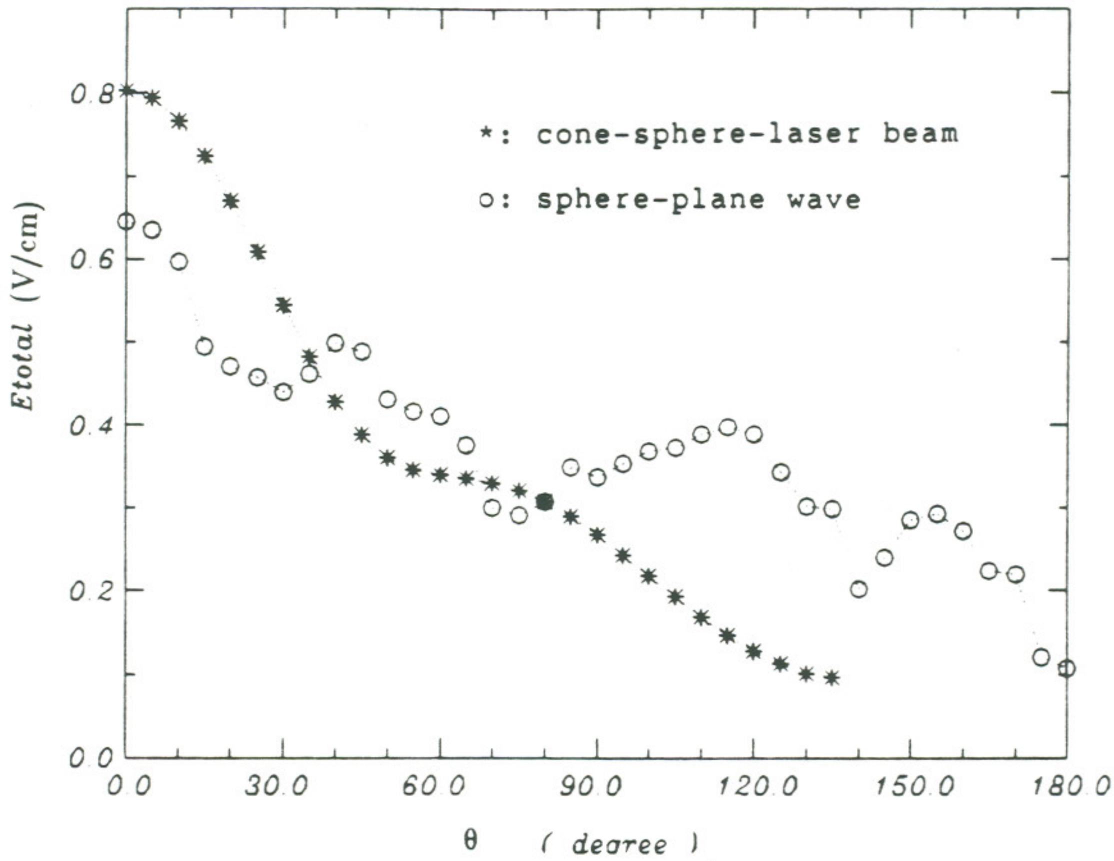

Fig 4.10 The near field enhancement along θ

($r = 0.01\ \mu m$, $\phi = 0°$)

Chapter 5. EXPERIMENTAL APPROACH

5.1 Introduction

Experimental work was done to measure the far field intensity distribution and compare it to the theory. A liquid metal ion source (LMIS) was used to approximate the sphere tipped cone in our experiment. The experimental set up and procedures which measure the far field pattern are explained in detail. Finally, this chapter ends by showing the experimental results i.e., the interaction between the incident laser and LMIS, which can be observed from the distribution of the laser beam intensity in its far field pattern.

5.2 The Laser Optical System

An Argon laser, Coherent Innova 70, with wavelength of about 0.5 μm was used in the experiments. The optical alignment system for focusing the laser beam into the tip is shown in Figure 5.1 . After passing through a small aperture with the radius of 1.5 mm, the laser beam is then expanded up to 15 mm by a 10X beam expander. The collimated beam was then focused to a final spot by an achromatic lens which was mounted on an XYZ optical

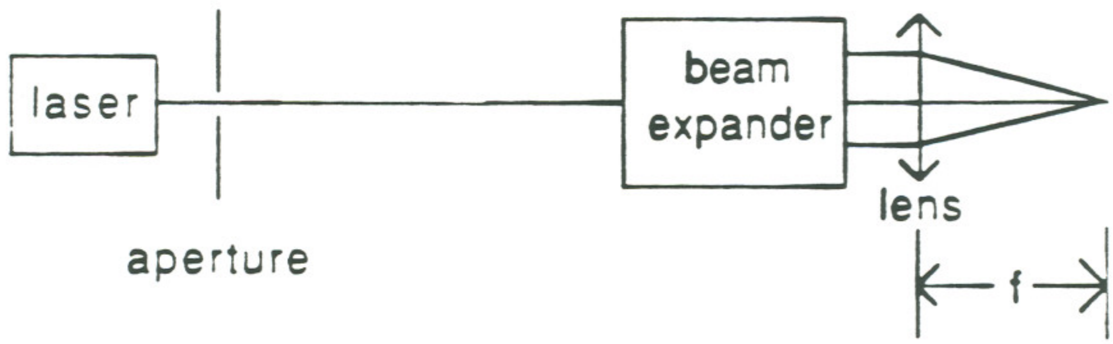

Figure 5.1 Optical alignment system of the laser beam

positioner. The adjustable positioner allowed us to adjust the location of the focused spot with respect to the tip position.

The spot size of a collimated Gaussian laser beam can be theoretically estimated as[122]

$$\omega_0 = \frac{f\,\lambda}{\pi\,\omega} \tag{5.17}$$

where the f is the focal length of the lens, ω is the collimated radius (e^{-2}) of the input laser beam and λ is the wavelength of the laser beam as shown in Figure 5.2 . We assumed that the lens of diameter ω which contains about 85 % of the focused energy and the edge of which the focused intensity is already down to $1/\,e^2 \approx 14$ % of its peak value. Combining these criteria then gives equation (5.17). In our experiment, using the traditional knife edge method, [122] we measured the minimum spot size which was about 8 μm . This value is a little bigger than the theoretical value. The aberrations of the lenses in the optical system is the main reason for the discrepancy.

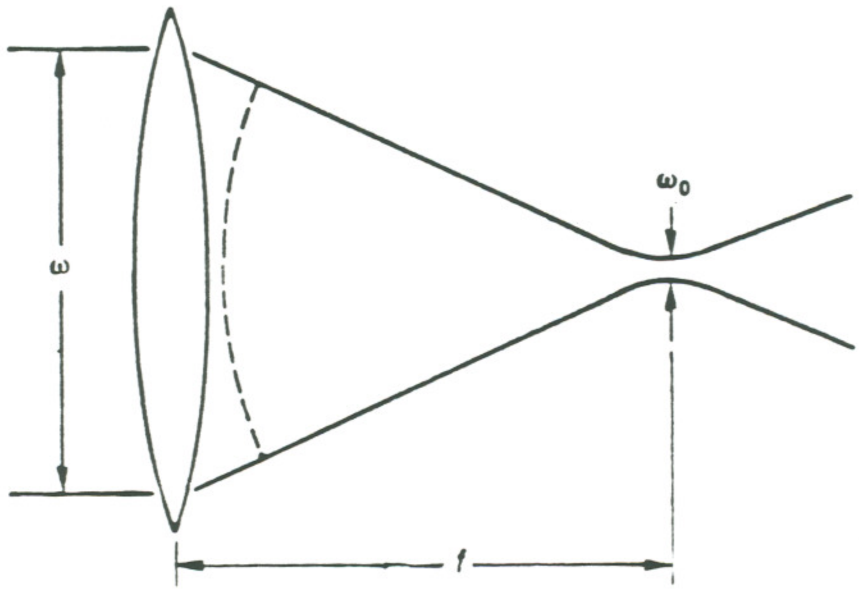

Figure 5.2 Focusing of a Gaussian beam to a small spot size

5.3 The Mechanism of the Liquid Metal Ion Source (LMIS)

5.3.1 Taylor Cone Theory

The principles of operation of LMIS have been studied by several investigators since 1960. The investigation subsequent to 1964 were all based upon Taylor's work in which he considered whether a stable equilibrium could exist for a liquid in an electric field. Taylor also concluded that the electrostatic force f_e can balance the surface tension f_s on the liquid surface only when a cone-shaped structure existed. The balance between the electric force and the surface tension can be written as:

$$\gamma(\frac{1}{r_1} + \frac{1}{r_2}) = \frac{1}{2}\epsilon_0 F^2 \tag{5.18}$$

where γ is the surface tension of the liquid, r_1 and r_2 the principle radii of curvature, F the electric field strength and ϵ_0 the vacuum dielectric constant. Taylor showed that equation (5.18) could be satisfied by an simple and well known form electric potential as:

$$V = V_0 + AR^{1/2}P_{1/2}(\cos\theta) \tag{5.19}$$

where R is the radius vector in spherical polar coordinates, θ is measured from the axis of the cone and $P_{1/2}(\cos\theta)$ the Legendre function of order 1/2 . This is satisfied for $\theta = 130.7^0$ which gives a half angle α of the cone equal to 49.3^0 . This is illustrated in Figure 5.3 .

5.3.2 Gallium Liquid Metal Ion Source

The LMIS consists of a low volatility liquid metal film flowing to the apex of a solid needle support structure whose apex radius is $\approx$ 1-5 micro[29]. The application of an electric field of sufficient strength will deform the liquid film on the needle apex into a conical protrusion as shown in Figure 5.4 for a Bi LMIS that was solidified during operation and photographed in a SEM. Our experiment, the material Tungsten was used for the needle and was coated with a layer of Gallium. When the positive high voltage was applied to the Tungsten, the ions of Gallium would flow to the tip and take the shape of a cone. As shown by Taylor[18], the cone is stabilized by the static balance between the surface tension and electrostatic forces when the cone half-angle is 49.3^0 .

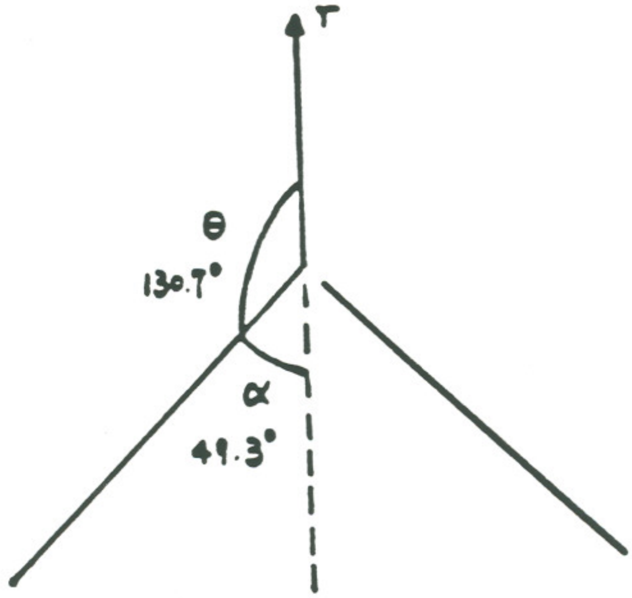

Figure 5.3 The spherical polar coordinate used by Taylor to solve the balance equation (5.18) to obtain the critical cone angle 49.3^0

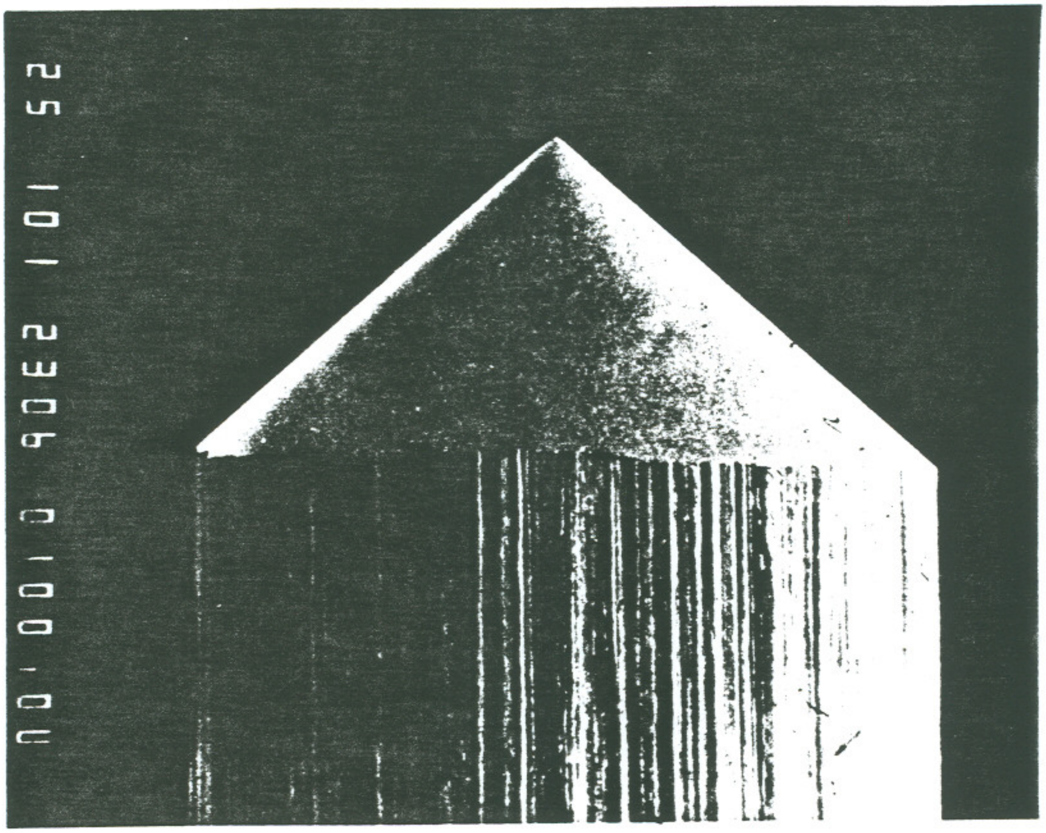

Figure 5.4 SEM photo of a "frozen" Bi Taylor cone

The use of Focused Ion Beams (FIB) employing LMIS as a micromachining manufacturing tool has proved to be a very promising technique in microfabrication. However, neither group has attempted to use a focused laser beam to that micromachining process. Jousten, Holmes and Orloff[141] demonstrated that high frequency modulation of the emission source current of LMIS can be achieved by focusing amplitude modulated laser beam onto the very end of the LMIS tip apex. In preliminary experiments conducted by them the laser beam was focused to a 10 micro spot size and the LMIS response time was found to be 1.5 micro seconds. They also further theoretically predicted that, with a smaller laser spot size, a response time of the LMIS as short as a few tens of nanosecond could be achievable.

Our LMIS was a commercially available Ga source from FEI company, consisting of a tungsten needle substrate with diameter of 180 μm , electrochemically etched to a paraboloidal shape of 35^0 half angle and ending with a radius of 7 μm, spot welded on a loop supporting the Ga-reservoir. The needle was coated with Ga liquid metal which could be heated by direct ohmic heating of the supporting wire. A 6 mm diameter extractor electrode was located 1 mm in front of the emitter. By applying a potential of several kilovolts to the source relative to the extractor electrode, the liquid metal at the needle apex will be distorted to form a Taylor cone and the Ga atoms will be field evaporated from the source and ionized. In our experiment, a 7-8 kV

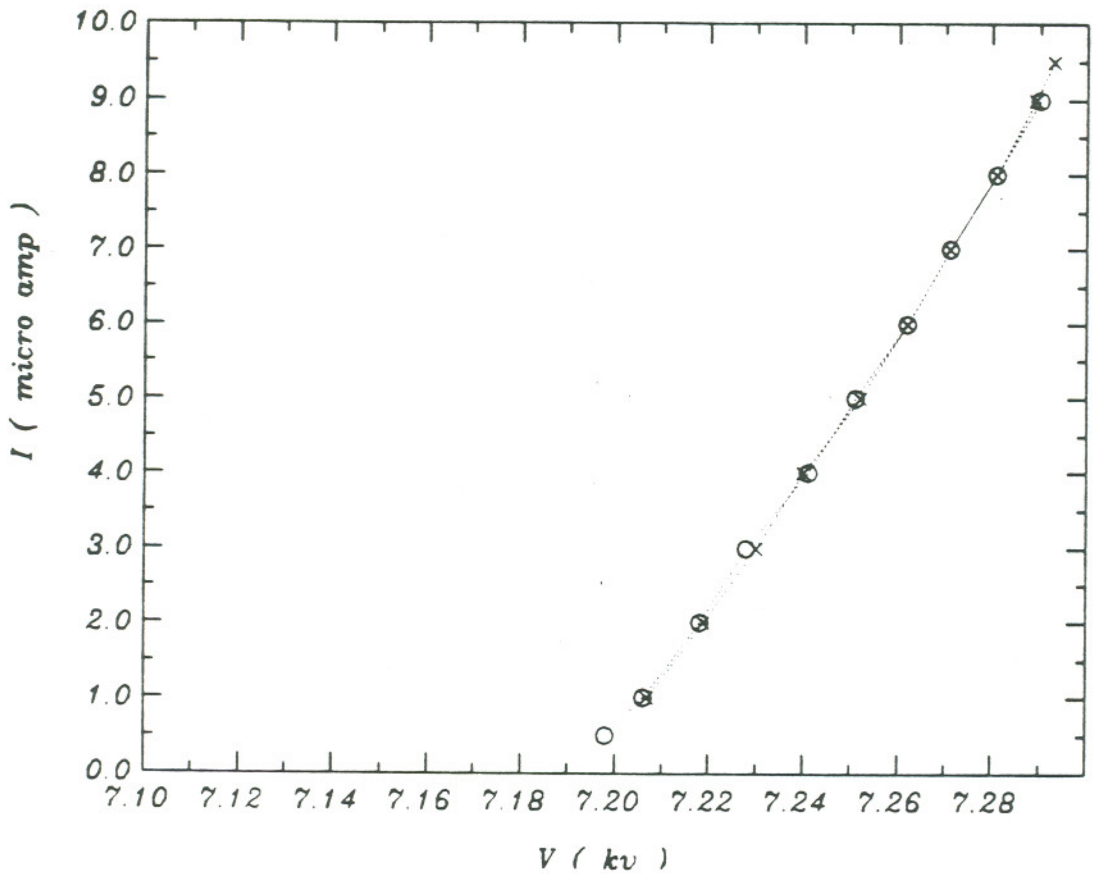

Figure 5.5 The emitted current versus the applied voltage

high voltage was used which leads to a 5 μA emission current. Figure 5.5 shows the current versus voltage response for the LMIS.

There are two windows on the vacuum chamber (See Figures 5.6 - 5.8): one was made of a high quality optical glass which allowed the laser beam to enter the chamber without distortion. Another let the laser beam to exit the chamber after hitting the tip so that the tip shadow image could be observed on a screen placed outside the chamber and the far field pattern can be measured. Figure 5.6 and 5.7 show the equipment that was used in the experiment. Inside the chamber, a 10^{-8} torr vacuum pressure was achieved using an ion pump. The detailed experimental set up will be discussed in the next section.

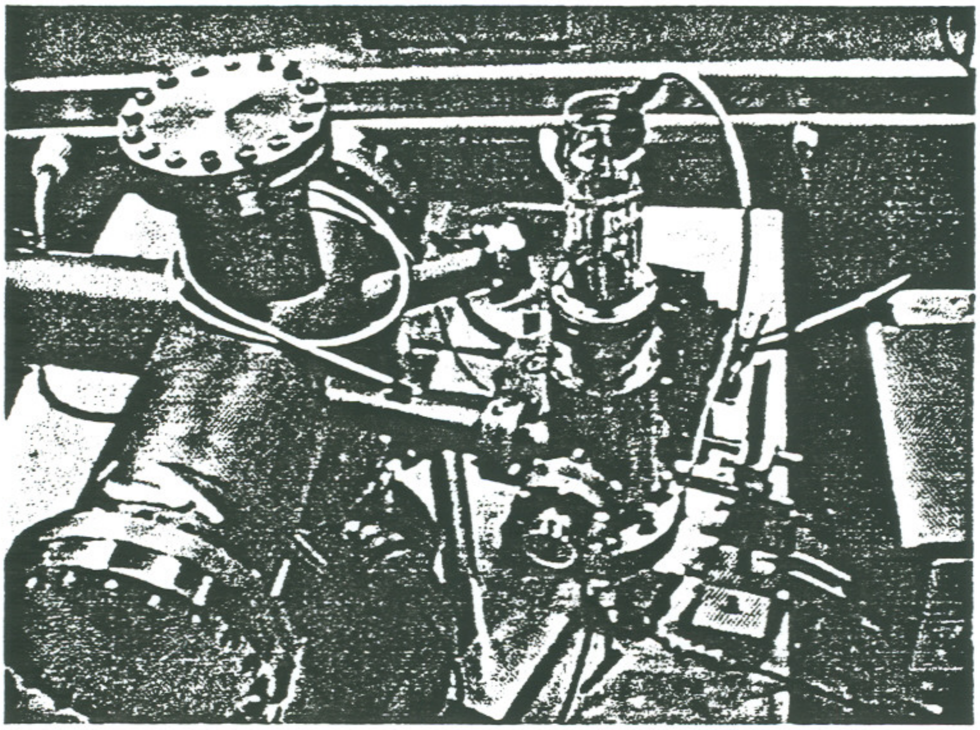

Figure 5.6 The vacuum system with high voltage 7-8 kV

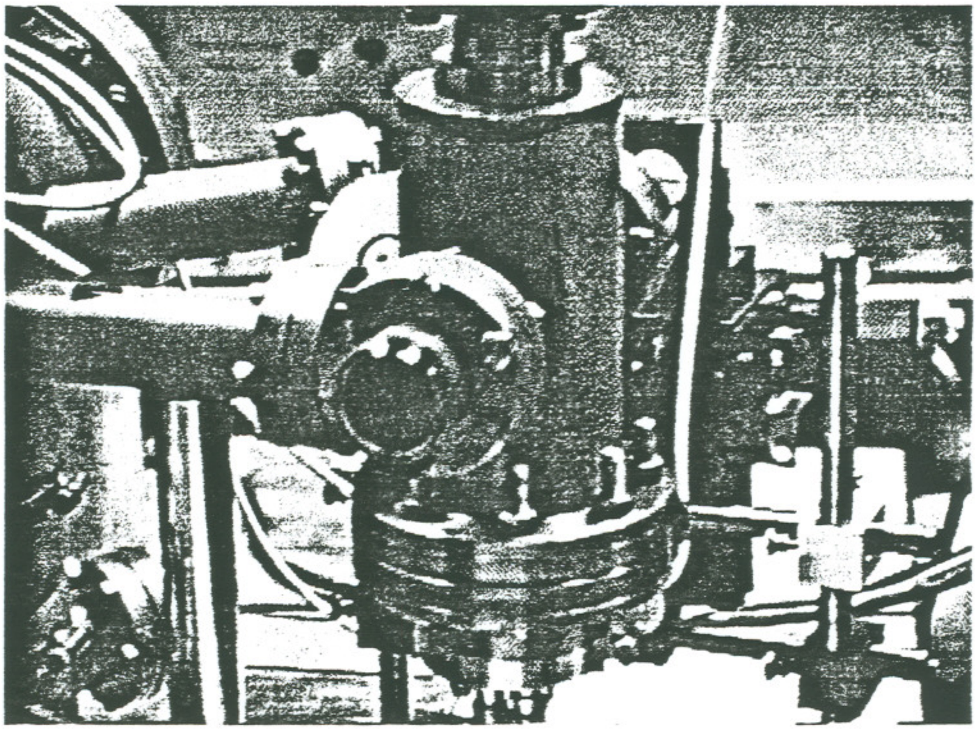

Figure 5.7 The output window where the image can be taken

5.4 Experimental Setup

This section describes the experimental setup used for measuring the far field intensity pattern of the laser focused onto the LMIS tip. Figure 5.8 shows the relevant equipment associated with the measurements. Using a collimated laser beam and a focusing lens, the "XYZ Translation Stage" can be adjusted to focus the laser beam onto the tip of the LMIS. The far field pattern is then observed on the screen. The distance from the tip to the screen satisfies the Fraunhofer condition i.e.,

$$d >> \frac{\pi a^2}{\lambda} \tag{5.25}$$

where d is the distance from the lasing aperture to the measurement plane and a is the half width of the emitting aperture. For this experimental setup, a is 10 μm , the wavelength is 0.5 μ m and d was chosen from 300 to 500 mm so the Fraunhofer condition is considered to be satisfied.

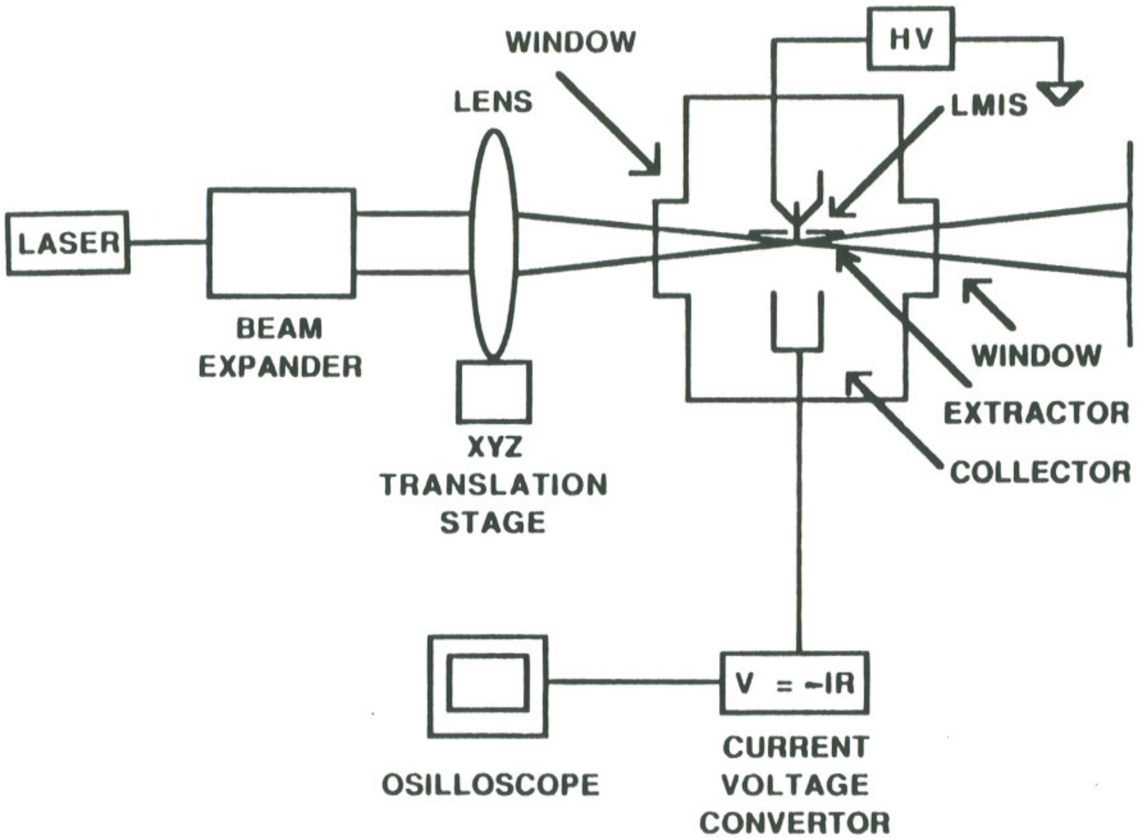

Figure 5.8 The schematic of the whole equipment for the experiment

As shown in Figure 5.9, the far field is then imaged by a high sensitivity, high resolution CCD camera (Panasonic, AG400P). This camera uses a 8.8 mm $\times$ 6.6 mm CCD solid state image sensor. No lenses were used to image the far field. Meanwhile the image was recorded with a commercial video cassette recorder (VCR). As seen in Figure 5.10, putting the video tape inside the VCR (Panasonic AG-6200), which is connected to a color video monitor (Panasonic BT-S1900N, Television) we can frame grab the image on the television screen which has a resolution of 600 $\times$ 480 pixels. A program is then used on the computer to choose a partion of the far field pattern to be stored. The program records the optical intensity over the window for each pixel and stores the pixel number vs intensity in a file. This file was transferred to the microvax by a work station (Tektronix, PEP 301). Analysis work was done on the microvax. In the next section, we will give the results of the measurements.

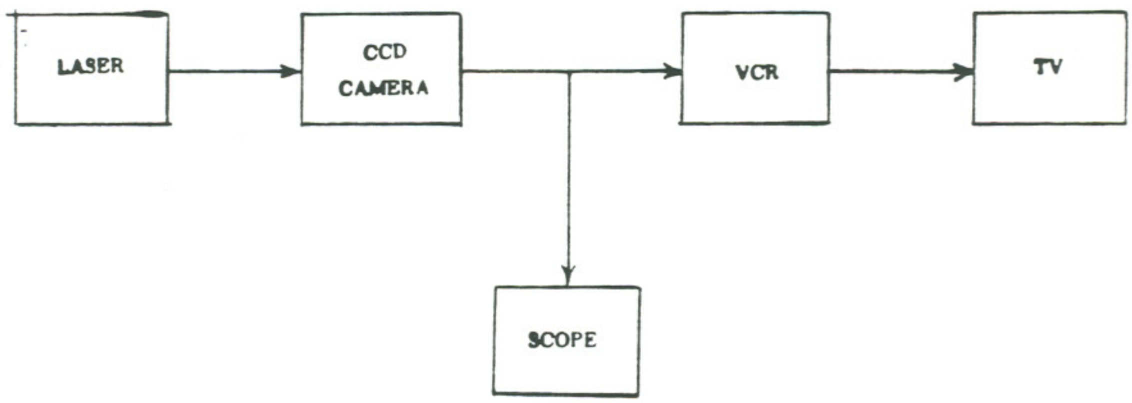

Figure 5.9 The schematic of the experimental set up to measure

the far field pattern of a focused laser beam

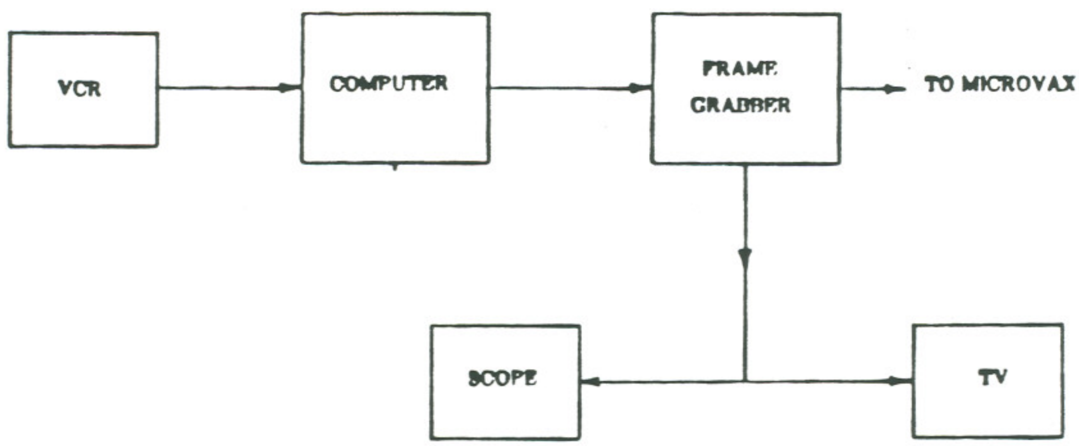

Figure 5.10 The schematic of the experimental set up to

transfer the frame grabbed data to the microvax

5.5 The Specifications of the Focused Laser Beam Distribution in Far Field Pattern

In the experiment we were carefully to focus the laser beam precisely onto the tip of the LMIS. This can be accomplished by adjusting the 'XYZ Translation Stage' in Figure 5.8. Fortunately, since we can see the shadow image of the LMIS tip on the screen outside of the vacuum chamber, proper adjustment can be accomplished. Figure 5.11 is a picture of the image when the laser is focused beyond the tip. When the image on the screen disappears like is shown in Figure 5.12, the laser beam is focused onto the tip of the LMIS. The light and dark splotches in Figures 5.11 and 5.12 are caused by laser speckle.

After the laser beam has been focused, the far field pattern can be measured. The CCD camera recorded various images on video tape.

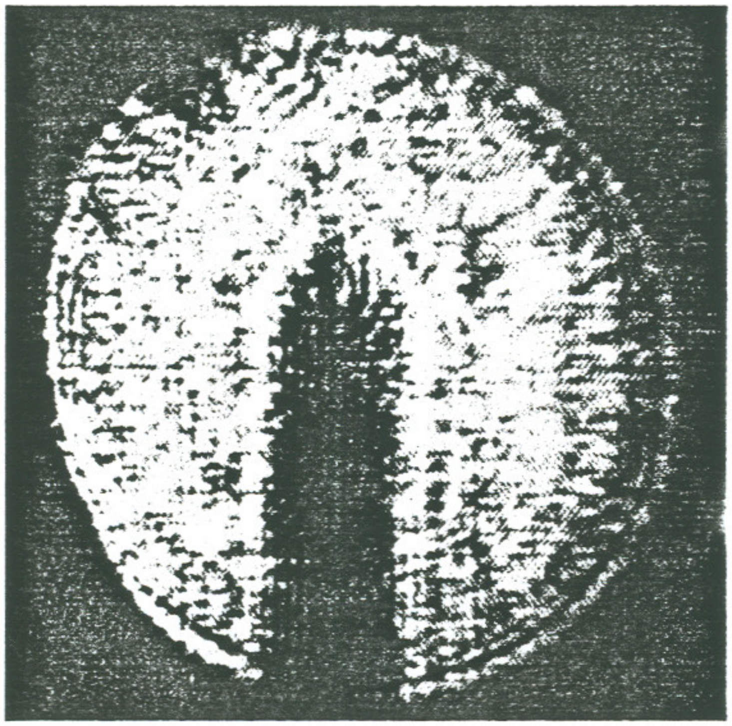

Figure 5.11 The image of the LMIS when the laser beam

is not focused on its tip

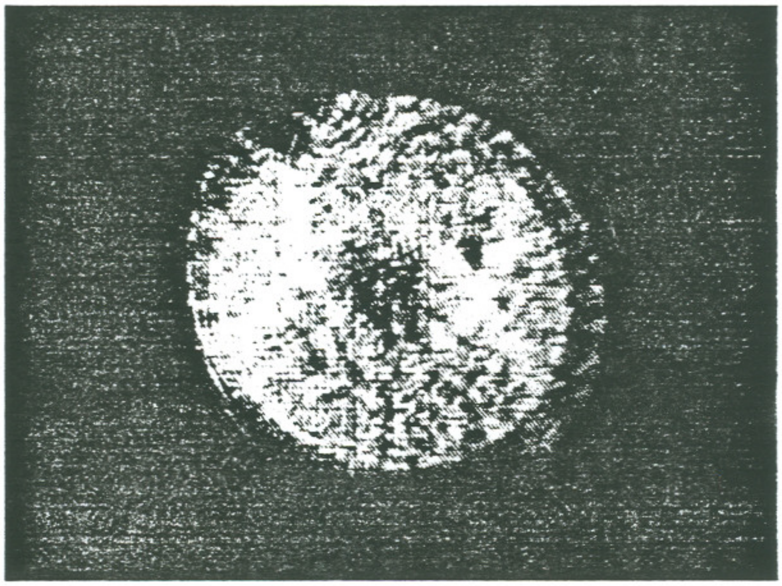

Figure 5.12 The image of the LMIS when the laser beam

is focused on its tip

The coordinate system used for selecting intensity data from the image on the screen is shown in Figure 5.13 . The far field patterns along the **z** direction and **y** direction relative to the shadow pattern of the cone tip are shown for the slightly defocused case in Figures 5.14 - 5.16 . The bumps in the curves are due to laser speckle.

The far field pattern for the case when the laser is precisely focused onto the tip is shown in Figures 5.17(a) and (b) for tip screen distances of 300 mm and 500 mm respectively. Where $\alpha = \phi - 90^0$. The results are qualitatively comparable to the numerical results shown in Figure 4.8(c). The bumps are again caused by laser speckle.

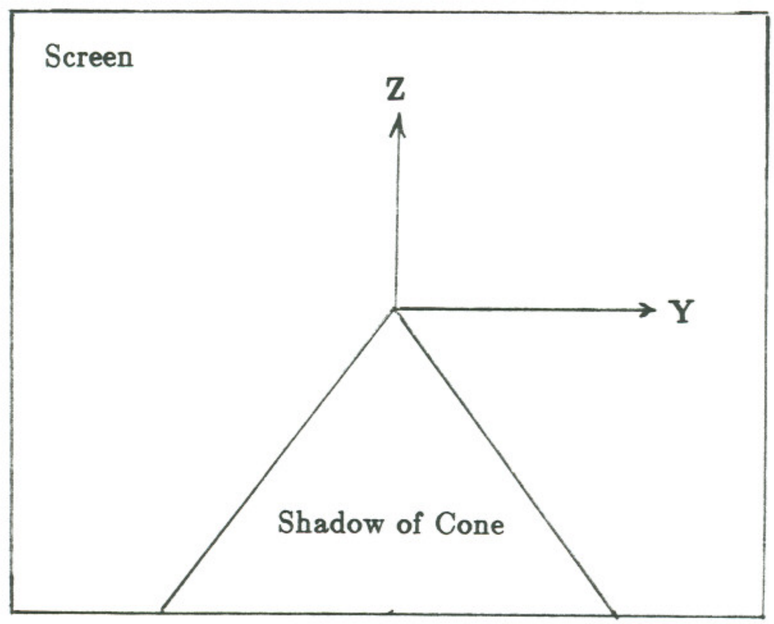

Figure 5.13 Coordinate system on the screen

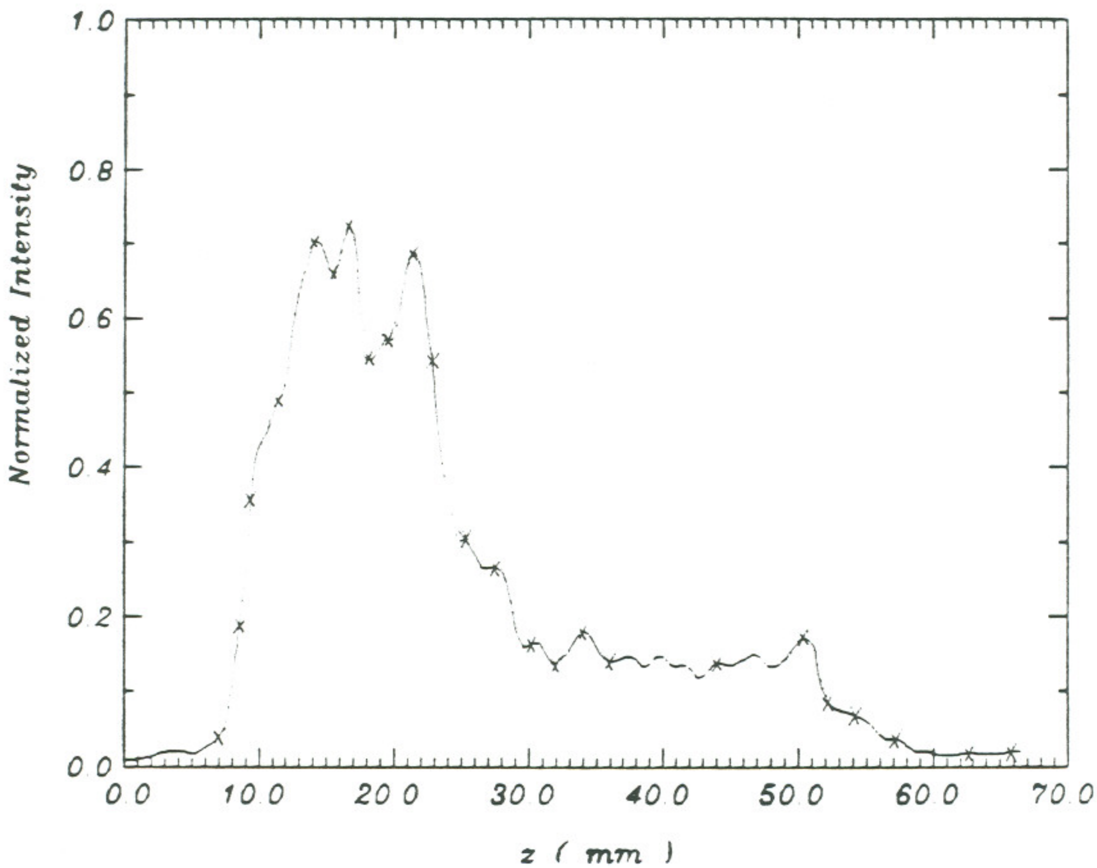

Figure 5.14 The distribution of the far field pattern

along **z** axis ($\theta=0^0$, $\phi=0^0$)

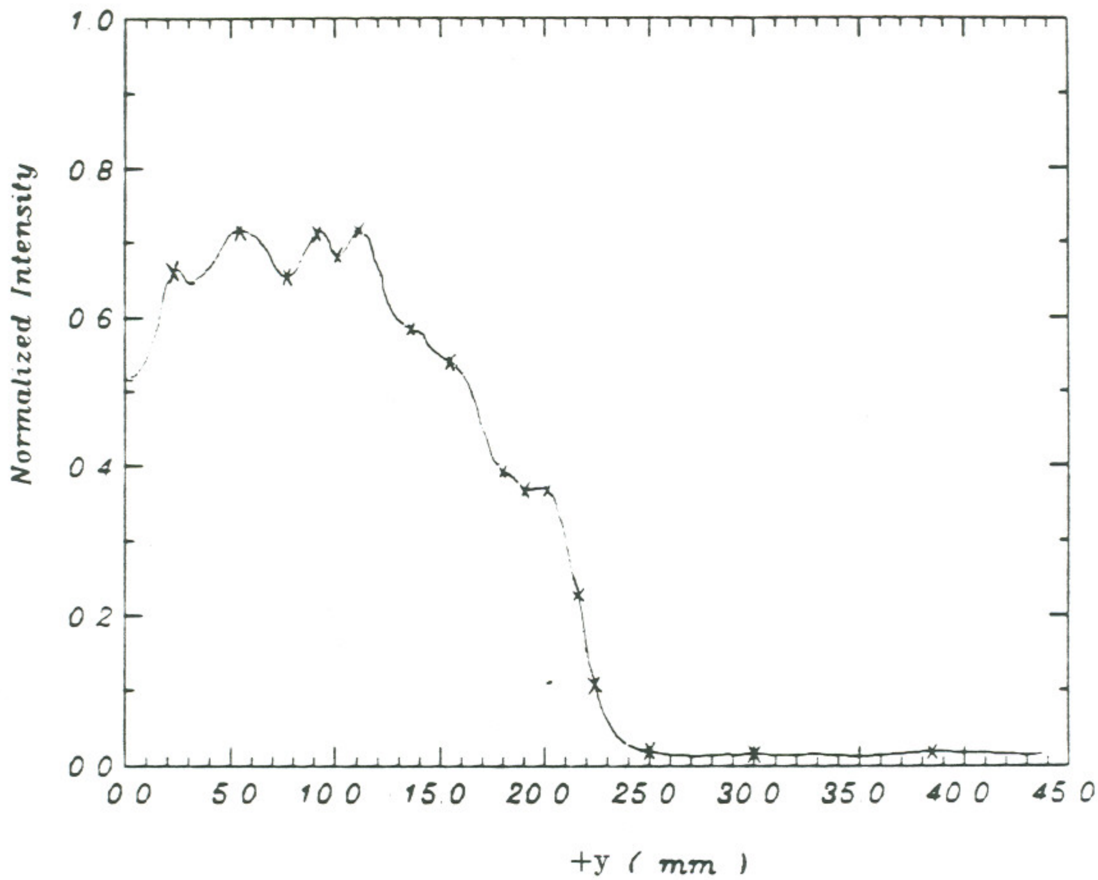

Figure 5.15 The distribution of the far field pattern

along +y axis ($\theta = 0^0$, $\phi = 90^0$)

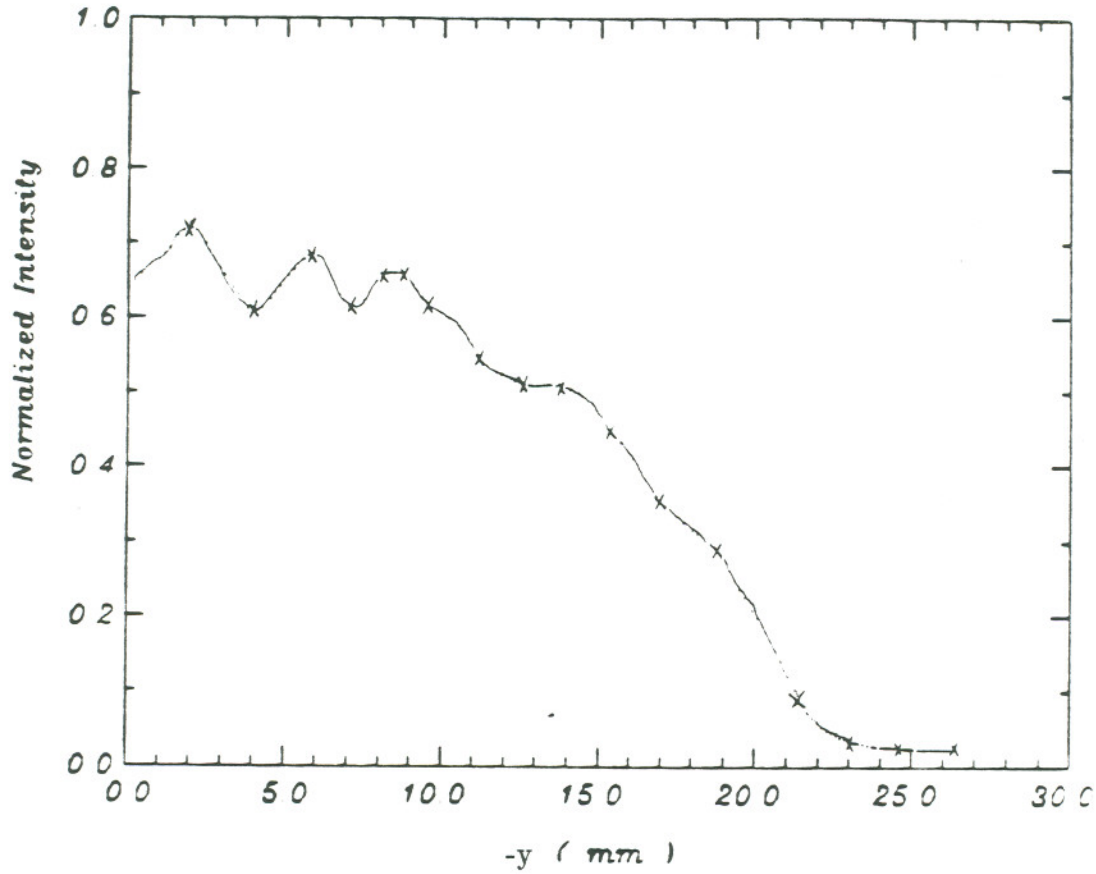

Figure 5.16 The distribution of the far field pattern

along $-\mathbf{y}$ axis ($\theta=0^0$, $\phi=270^0$)

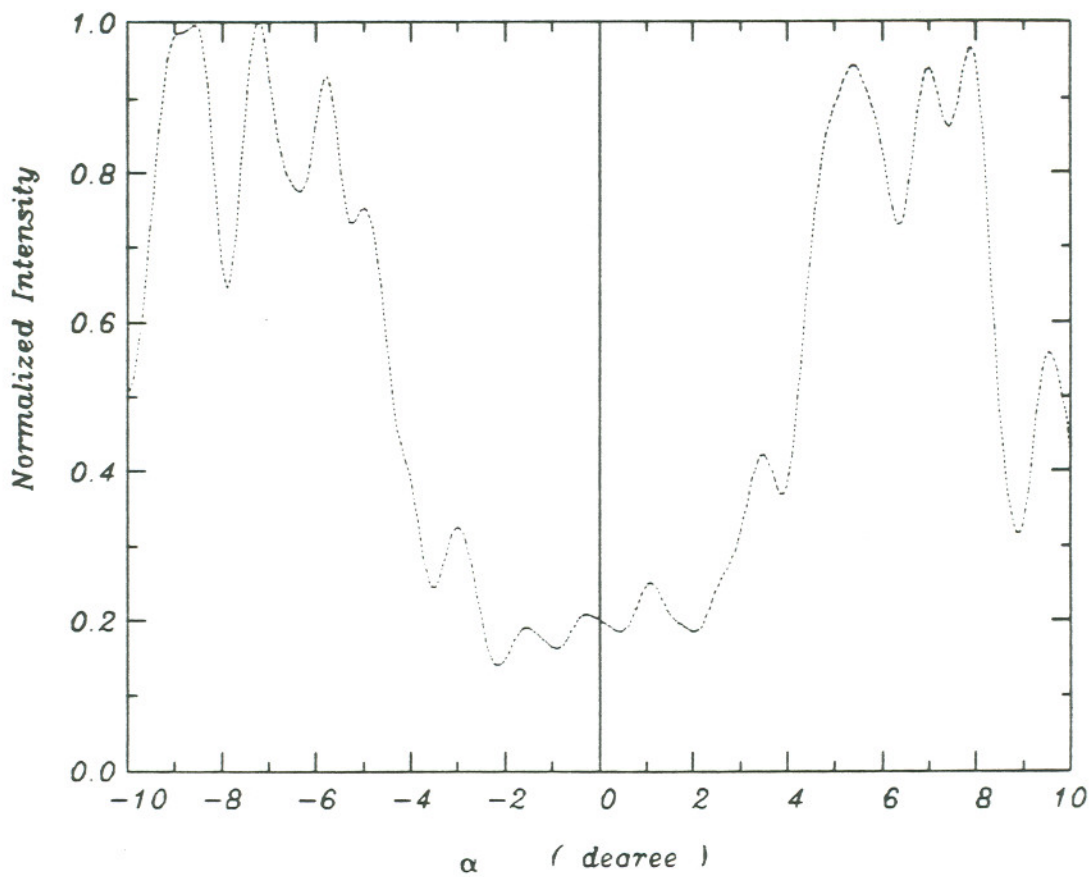

Figure 5.20(a) The field intensity changes with α (d = 300 mm)

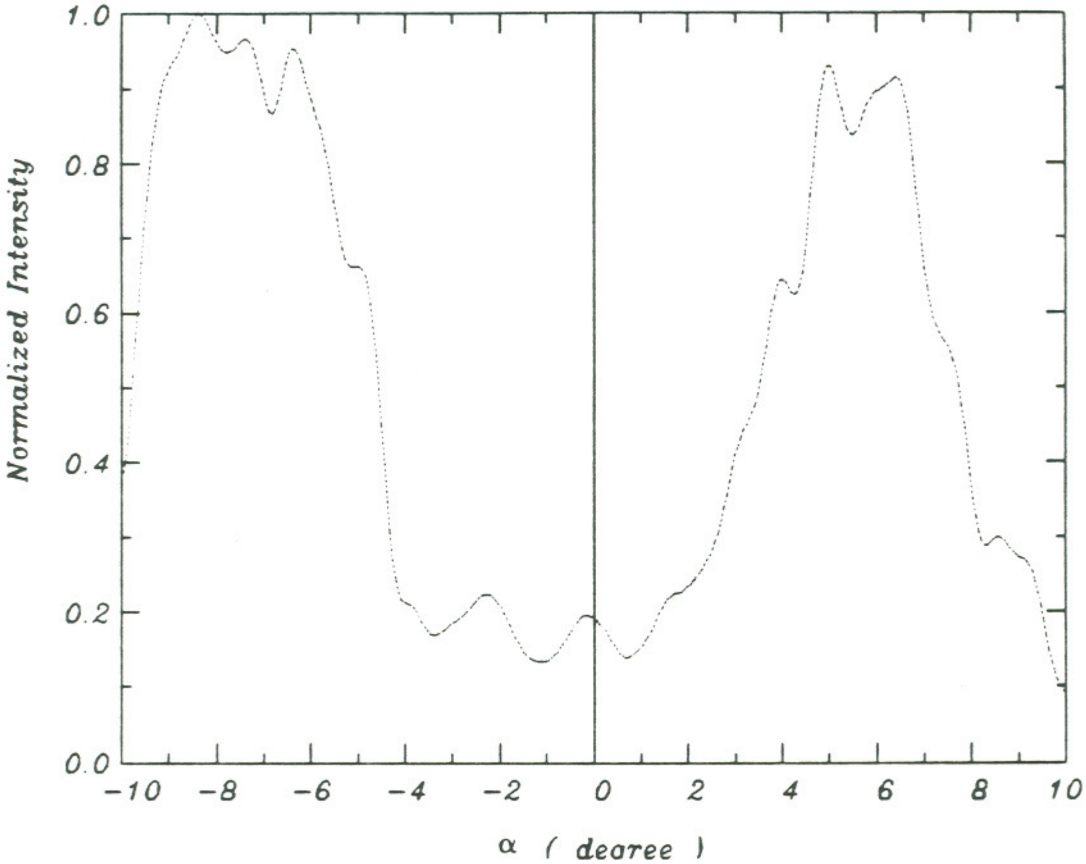

Figure 5.20(b) The field intensity changes with α (d = 500 mm)

CHAPTER 6. CONCLUSIONS

6.1 Conclusions

In the present dissertation we discussed the interaction between a focused laser beam and a liquid metal ion source. Our conclusions can be summaried in two respects. Theoretically, the Hertz potentials in spherical coordinates can be used to generate a solution for the electric and magnetic fields which valid everywhere. In experiment part, a sphere tipped cone is a reasonable model for a liquid metal ion source.

6.2 Future Work

We would like to use the results of this work to predict the effect of a focused laser beam on an electron field emitter.

References

1. L. B. Felsen, "Alternative Field Representations in Regions Bounded by Sphere, Cones, and Planes," *IRE Trans. Antennas and Propagation*, vol. 5 , 1957.
2. K. K. Chan and L. B. Felsen, "Transient And Time-Harmonic Diffraction by a Semi-Infinite Cone," *IEEE Trans. Antennas and Propg.*, vol. AP-25, No. 6, p. 236, Nov, 1977.
3. K. K. Chan, L. B. Felsen, A. Hessel and J. Shmoys, "Creeping Waves on a Perfectly Conducting Cone," *IEEE Trans. Antennas and Propg.*, vol. AP-25, No. 6, p. 245, Nov, 1977.
4. K. K. Chan and L. B. Felsen, "Transient And Time-Harmonic Dyadic Green's Function for a Perfectly Conducting Cone," *IEEE Trans. Antennas and Propg.*, vol. AP-27, No. 1, Jan 1979.
5. L. B. Felsen, "Plane-Wave Scattering by Small-Angle Cones," *IRE Trans. Antennas And Propagation*, vol. 5, 1957.
6. Youn H. Choung, "Sum and tracking radiation patterns of a conical horn," *IEEE Transaction on antennas and propagation*, vol. AP-32, No. 12, pp. 1288-1291, Dec, 1984.
7. L. B. Felsen and P. Marcuvitz, *Radiation and Scattering of waves*, 1968.
8. L. W. Swanson and D. R. Kingham, "On the mechanism of liquid metal ion sources," *Appl. Phys.*, vol. A 41, pp. 223-232, 1986.
9. Melvin Lax, W. H. Louisell and W. B. McKnight, "From Maxwell to Paraxial Wave Optics," *Physics Review*, vol. 11, No. 4, p. 1365, Apr. 1975.
10. J. B. Barton, D. R. Alexander and S. A. Schaub, "Internal and Near-Surface Electromagnetic Fields for a Spherical Particle Irradiated by a Focused Laser Beam," *J. Appl. Phys.*, vol. 64 (4), 15 Aug, 1988.
11. P. W. Dusel, M. Kerker, and D. D. Cooke, "Distribution of Absorption Centers within Irradiated Spheres," *Opt. Soc. Am.*, vol. 69, No. 1, Jan 1979.
12. W. M. Green, R. E. Spjut, E. Bar-Ziv, A. F. Sarmfim and J. P. Longwell, "Photophoresis of Irradiated Spheres: Absorption Centers," *J. Opt. Soc. Am.*, vol. B2 , p. 998, 1985.

13. N. Morita, T. Tanaka, T. Yamasaki and Y. Nakanishi, "Long wave scattered by a homogeneous sphere," *IEEE Trans. Antennas and Propag.*, vol. AP-16, p. 724, 1968.

14. W. C. Tsai and R. J. Pogorzelski, "Far field scattering of the Gaussian beam on a homogeneous sphere," *J. Opt. Soc. Am.*, vol. 65, p. 1457, 1975.

15. W. G. Tam and R. Corriveiu, "The Distribution of the far field around a spherical particle," *Opt. Am.*, vol. 68, p. 763, 1978.

16. J. S. Kim and S. S. Lee, "Scattering of laser beams and the optical potential well for a homogeneous sphere," *Opt. Am.*, vol. 73, p. 303, 1983.

17. G. Gouesbet, G. Greham and B. Maheu, "Electromagnetic fields in the presence of ideally conducting conical structure," *Opt. (Paris)*, vol. 16, p. 83, 1985.

18. G. I. Taylor, "Disintegration of water drops in an electric field," *Proc. Roy. Soc.*, vol. A280, p. 383, 1964.

19. J. F. Mahoney, A. T. Yahiku, H. L. Daley, R. D. Moore, and J. Perel, "Electrohydrodynamic ion source," *Appl. Phys.*, vol. 40(13), pp. 5101-5106, 1969.

20. V. E. Krohn and G. R. Ringo, "Ion source of high brightness using liquid metal," *Appl. Phys. Lett.*, vol. 27, p. 479, 1975.

21. J. Orloff and L. W. Swanson, "An asymmetric electrostatic lens for field-emission microprobe applications," *J. Appl. Phys.*, vol. 50(4), pp. 2494-2501, 1979.

22. J. Orloff and L. W. Swanson, "Study of a field-ionization source for microprobe applications," *J. Vac. Sci. Technol.*, vol. 12(6), pp. 1209-1213, 1975.

23. J. Orloff and L. W. Swanson, "Fine-Focus ion beams with field Ionization," *J. Vac. Sci. Technol.*, vol. 50, p. 6026, 1979.

24. J. Orloff and L. W. Swanson, "A study of some electrostatic gun lenses for field emission," *Scanning Electron Microscopy*, vol. I, p. 39, SEM Inc., O'Hare, Ill, 1979.

25. J. Orloff and L. W. Swanson, "Angular intensity of a gas-phase field ionization source," *J. Appl. Phys.*, vol. 50(9), pp. 6026-6027, 1979.

26. R. L. Seliger and W. P. Fleming, "Focused ion beam in microfabrication," *J. Vac. Sci. Technol.*, vol. 10(6), p. 1127, 1973.

27. J. Orloff, *A scanning ion microscope with a field ionization source*, 1976. Ph.D Dissertation

28. L. W. Swanson, "Recent advances in liquid metal ion sources," *Micro Circuit Engineering*, vol. 80, pp. 267-281, Delft University Press, 1981. Edited by R. P. Kramer

29. L. W. Swanson and G. A. Schwind, "Electron emission from a liquid metal," *J. Appl. Phys.*, vol. 49(11), pp. 5655-5662, 1978.

30. L. W. Swanson, G. A. Schwind and A. E. Bell, "Emission chacteristics of a liquid metal ion source," *Scanning Electron Microscopy*, p. 45, SEM Inc., O'Hare, Ill, 1979.

31. A. Wagner, "Liquid gold ion source," *J. Vac. Sci. Thchnol.*, vol. 16(6), pp. 1871-1874, 1979.

32. Eizo Miyauchi, Hiroshi Arimoto, Hisao Hashimoto, and Takao Utsumi, "Selective Si and Bi implantation in GaAs using a 100 kv mass-separating focused ion beam system with an Au-Si-Be liquid metal ion source," *J. Vac. Sci. Technol.*, vol. B 1(4), pp. 1113-1116, 1983.

33. C. D'Cruz, K. Pourrezaei, and A. Wagner, "Ion cluster emission and deposition from liquid gold ion sources," *J. Appl. Phys.*, vol. 58(7), pp. 2724-2730, 1985.

34. H. Arimoto, A. Takamori, E. Miyauchi, and H. Hashimoto, "Formation of submicron isolation in GaAs by implanting a focused boron ion beam emitted from a Pd-Ni-Si-Be-B LM ion soource," *J. Vac. Sci. Technol.*, vol. B 3(1), pp. 54-57, 1985.

35. D. L. Barr, "Gallium clusters from a liquid metal ion source," *J. Vac. Sci. Technol.*, vol. A 5(5), pp. 2907-2811, 1987.

36. M. J. Bozack, L. W. Swanson, and A. E. Bell, "Surface phenomena in liquid metal alloys of arsenic: vapor pressure reduction and wetting to refractory metals," *J. Materials Research*, vol. 4(1), pp. 85-93, 1989.

37. S. Rao, A. E. Bell, G. A. Schwind, and L. W. Swanson, "The angular dependence of the emission characteristics for a Pd_2 As liquid-alloy ion source," *J. Vac. Sci. Technol.*, vol. B 8(6), pp. 1932-1936, 1990.

38. U. Kreissig, A. Kahn, F. G. Ruedenauer, and W. Steiger, "Mass and

energy analysis of an AuSi liquid metal ion source," *J. Phys. D: Appl. Phys*, vol. 23, pp. 959-963, 1990.

39. T. Ishitani, K. Umemura, and T. Aida, "Movable needle type of liquid-metal-ion source for boron and phosphorus ions," *J. Vac. Sci. Technol.*, vol. A 5(5), pp. 2907-2911, 1987.

40. Y. Ochiai, E. Nomura, Y. Kojima, and S. Matsui, "Flourine field ion source using flurine-helium gas mixture," *J. Vac. Sci. Technol.*, vol. A 9(1), pp. 51-56, 1991.

41. J. van de Walle and P. Joyes, "Remarkable periodicity of Ge_n^p ions (n/p $\leq$ 25, 1, = p $\leq$ 4) formed by the liquid-metal ion-source technique," *Phys. Review B*, vol. 32(12), pp. 8381-8383, 1985.

42. S. Rao, A. E. Bell, G. A. Schwind, and S. L. Swanson, "Angular distribution of ion from an AuSi liquid metal ion source," *J. Vac. Sci. Technol.*, vol. A 8(3), pp. 2258-2264, 1990.

43. M. Francois, K. Pourrezaei, A. Bahasadri, and D. Nayak, "Investigation of the liquid metal ion source cluster beam constituents and their role in the properties of the deposited film," *J. Vac. Sci. Technol.*, vol. B 5(1), pp. 178-183, 1987.

44. T. Ishitani, K. Umemura, and Y. Kawanami, "Favorable source material in liquid-metal-ion sources for focused beam application," *J. Vac. Sci. Technol.*, vol. B 6(3), pp. 931-935. 1988

45. A. L. Pregenzer, K. W. Bieg, and R. E. Olson, "Ion production from LiF-coated field emitter tips," *J. Appl. Phys.*, vol. 67(12), pp. 7556-7559, 1990.

46. K. Horiuchi, T. Itakura, and H. Ishikawa, "Emission chacteristics and stability of hellium field ion source," *J. Vac. Sci. Technol.*, vol. B 6(3), pp. 937-940, 1988.

47. T. Ishitani, K. Umemura, and Y. Kawanami, "Ion formation in alloy liquid-metal-ion sources," *J. Appl. Phys.*, vol. 61(2), pp. 748-755, 1987.

48. R. H. Higuchi-Rusli, K. C. Cadien, J. C. Corelli, and A. J. Steckl, "Development of boron liquid metal ion source for focused ion beam system," *Vac. Sci. Technol.*, vol. B 5(1), pp. 190-194, 1987.

49. V. Wang, J. W. Ward, and R. L. Seliger, "A mass-separating focused-ion-beam system for maskless ion implantation," *J. Vac. Sci. Technol.*,

vol. 19(4), pp. 1158-1163, 1981.

50. R. Levi-Setti and G. Crow, "High spatial resolution SIMS with the UC-HRL scanning ion microprobe," *J. De. Physique*, vol. C9, pp. 197-205, 1984.

51. J. Orloff and L. W. Swanson, "Optical column design with liquid metal ion sources," *J. Vac. Sci. Technol.*, vol. 19(4), pp. 1149-1152, 1981.

52. T. Ishitani, H. Tamura, and H. Todokoro, "Scanning microbeam using a liquid metal ion source," *J. Vac. Sci. Technol.*, vol. 20(1), pp. 80-83, 1982.

53. J. R. A. Cleaver and H. Ahmed, "A 100 kv ion probe microfabrication system with a tetrode gun," *J. Vac. Sci. Technol.*, vol. 19(4), pp. 1145-1148, 1981.

54. J. S. Huh, M. I. Shepard and J. Melngailis, "Focused ion beam lithography," *J. Vac. Sci. Technol.*, vol. B 9(1), pp. 173-175, 1991.

55. D. H. Narum and R. F. W. Pease, "A variable energy focused ion beam for in situ microfabrication," *J. Vac. Sci. Technol.*, vol. B 6(3), pp. 966-973, 1988.

56. J. Melngailis, "Focused ion beam technology and applications," *J. Vac. Sci. Technol.*, vol. B 5(2), pp. 469-495, 1987.

57. J. R. A. Cleaver and J. Ahmed, "A combined electron and ion beam lithography system," *J. Vac. Sci. Technol.*, vol. B 3(1), pp. 144-147, 1985.

58. H. Kasahara, H. Sawaragi, R. Aihara, K. Gamo, S. Namba, and M. H. Shearer, "A 0-30 kev low-energy focused ion beam system," *J. Vac. Sci. Technol.*, vol. B 6(3), pp. 974-976, 1988.

59. J. C. Corelli, R. Higuchi-Rusli, S. Balakrishnan, and L. Liebmann, "Summary abstract : liquid metal ion source and applications in focused ion beam system," *J. Vac. Sci. Technol.*, vol. B 6(3), p. 936, 1988.

60. L. Zhou and J. Orloff, "Design of a high resolution focused ion beam system using liquid metal ion source," *J. Vac. Sci. Technol.*, vol. B 8(6), pp. 1721-1724, 1990.

61. Y. Kawanami, T. Ohnishi, and T. Ishitani, "Design of a high current-density focused-ion-beam optical system with the aid of chromatic aberration formula," *J. Vac. Sci. Technol.*, vol. B 8(6), pp. 1673-1675, 1990.

62. H. Sawaragi, H. Kasahara, R. Aihara, and M. H. Shearer, "Development od a focused ion beam system: Current status and future prospects," *J. Vac. Sci. Technol.*, vol. B 6(3), pp. 962-965, 1988.

63. L. R. Harriott, "A second generation focused ion beam micromachining system," *Proc. of the SPIE Symposium on Electron-Beam, X-Ray and Ion-Beam Lithographies*, vol. 773, pp. 190-194, 1987.

64. J. Orloff and P. Sudraud, "Design of a 100kv high resolution focused ion beam column with a liquid metal ion source," *Microelectronic Engineering*, vol. 3, pp. 161-165, North-Holland, 1985.

65. H. N. Slingerland, J. E. Barth, E. Koets, J. Kramer, and K. D. van der Mast, "Proposal for a second generation IBPG (in beam pattern generator)," *Microcircuit Engineering*, vol. 84, pp. 381-387, Academic Press, London, 1984.

66. R. K. DeFreez, J. Puretz, R. A. Elliott, G. A. Crow, H. Ximen, D. J. Bossert, G. A. Wilson and J. Orloff, "Focused-ion-beam micromachined diode laser mirrors," *Proc. of the SPIE Symposium on laser Diode Technology and applications*, vol. 1043, pp. 25-35, 1989.

67. L. R. Harriot, R. E. Scotti, K. D. Cummings and A. F. Ambrose, "Micromachining of integrated optical structures," *Appl. Phys. Lett.*, vol. 48(25), pp. 1704-1706, 1986.

68. R. A. Elliott, R. K. DeFreez, J. Puretz, J. Orloff and G. A. Crow, "Focused ion beam micromachining of diode laser mirrors," *Proc. of the SPIE Symposium on Communication Networking in Dense Electromagnetic Enviroments*, vol. 876, pp. 114-120, Jan 1988.

69. G. Crow, J. Pureta, J. Orlff, R. K. DeFreez, and R. A. Elliott, "The use of vector scanning for producting arbitrary surface contours with a focused ion beam," *J. Vac. Sci. Technol.*, vol. B 6(5), pp. 1605-1607, 1988.

70. J. M. Chabala, R. Levi-Setti, and Y. L. Wang , "Imaging microanalysis of surfaces with a focused gallium probe," *J. Vac. Sci. Technol.*, vol. B 6(3), pp. 910-914, 1988.

71. H. Morimoto, Y. Sasaki, Y. Watakable, and T. Kato, "Chacteristics of submicron patterns fabricated by gallium focused-ion-beam sputtering," *J. Appl. Phys.*, vol. 57(1), pp. 159-160, 1985.

72. J. G. Pellerin, D. P. Griffis, and P. E. Russell, "Focused ion beam machining of Si, GaAs amf InP," *J. Vac. Sci. Technol.*, vol. B 8(6), pp. 1945-1950, 1990.

73. M. Ando and J. J. Muray, "Spatial resolution limit for focused ion beam lithography from secondary electron energy measurements," *J. Vac. Sci. Technol.*, vol. B 6(3), pp. 986-988, 1988.

74. H. Ximen, ***A study of focused ion beam micromachining by development of a 3-D computer simulation and a 3-D digital scan strategy***, 1990. Ph.D Dissertation

75. H. Ximen, R. K. Defreez, J. Orloff, and R. A. Elliott, "Focused ion beam micromachined three-dimensional features by means of digital scan," *Vac. Sci. Technol.*, vol. B 8(6), pp. 1111-1114, 1990.

76. S. T. Davis and D. K. Bowen, "An apparatus for batch fabrication of micromechanical elements by ion beam machining," *J. Vac. Sci. Technol.*, vol. B 5(1), pp. 337-341, 1987.

77. G. A. Garfunkel and M. B. Weissman, "Fabrication techniques for nanometer scale resistors: A poor man's nanolithography," *J. Vac. Sci. Technol.*, p. B 8(5), 1087-1092, 1990.

78. D. B. Rensch, J. Y. Chen, W. M. Clark, Jr., and M. D. Courtney, "Submicrometer FET gate fabrication using resistless and focused ion beam techniques," *J. Vac. Sci. Technol.*, vol. B 3(1), pp. 286-289, 1985.

79. L. R. Harriott, H. Temkin, Y. L. Wang, R. A. Hamm, and J. S. Weiner, "Vacuum lithography for three-dimensional fabrication using finely focused ion beams," *J. Vac. Sci. Technol.*, vol. B 8(6), pp. 1380-1384, 1990.

80. S. Matsui, Y. Ochiai, Y. Kojima, H. Tsuge, N. Takado, K. Asakawa, H. Matsutera, J. Fujita, T. Yoshitake, and Y. Kubo, "Focused ion beam process for high T_c superconductors," *J. Vac. Sci. Technol.*, vol. B 6(3), pp. 900-905, 1988.

81. J. R. A. Cleaver, E. C. G. Kirk, R. J. Young, and H. Ahmed, "Scanning ion beam techniques for the examination of microelectronic devices," *J. Vac. Sci. Technol.*, vol. B 6(3), pp. 1026-1029, 1988.

82. J. E. Murguia, C. R. Musil, M. I. Shepard, H. Lezec, D. A. Antonoadis, and J. Melngailis, "Merging focused ion beam patterning and optical lithography in device and circuit fabrication," *J. Vac. Sci. Technol.*, vol.

B 8(6), pp. 1374-1379, 1990.

83. R. L. Kubena, R. J. Joyce, J. W. Ward, H. L. Garvin, F. P. Stratton, and R. G. Brault, "Dot lithography for zero-dimensional quantum wells using focused ion beams," *Appl. Phys. Lett.*, vol. 50(22), pp. 1589-1591, 1987.

84. T. Shiokawa, P. H. Kim, K. Toyoda, S. Namba, M. Suzuki, and S. Matsui, "Focused ion beam exposure charteristics of Langmuir-Blodgett films," *J. Vac. Sci. Technol.*, vol. B 6(3), pp. 993-995, 1988.

85. N. Koshida, Y. Ichinose, K. Ohtaka, M. Komuro, and N. Atoda, "Microlithographic behavior of transition metal oxide resists exposed to focused ion beam," *J. Vac. Sci. Technol.*, vol. B 8(5), pp. 1093-1096, 1990.

86. K. Gamo, H. Hamauzu, Zheng Xu, and Susumu Namba, "In situ development of ion bombarded poly(methylmethacrylate) resist in a reactive gas ambient," *J. Vac. Sci. Technol.*, vol. B 6(3), pp. 989-992, 1988.

87. K. Saitoh, H. Onoda, H. Morimoto, T. Katayama, Y. Watakabe, and T. Kato, "Practical results of photomask repair using focused ion beam technology," *J. Vac. Sci. Technol.*, vol. B 6(3), pp. 1032-1034, 1988.

88. O. W. Holland, C. W. White, M. K. El-Ghor, and J. D. Budai, "MeV, self-ion implantation in Si at liquid nitrogen temperature; a study of damage morphology and its anomoalous annealing behavior," *J. Appl. Phys.*, vol. 68(5), pp. 2081-2986, 1990.

89. C-M. Lin, A. J. Steckl, and T. P. Chow, "Thin-layer p-n junction fabrication using Ga and In focused ion beam implantation," *J. Vac. Sci. Technol.*, vol. B 6(3), pp. 977-981, 1988.

90. C-M. Lin, A. J. Steckl, and T. P. Chow, "Si p^+ -n shallow junction fabrication using on axis$-Ga^+$ implantation," *Appl. Phys. Lett.*, vol. 52(24), pp. 2049-2051, 1988.

91. C-M. Lin, A. J. Steckl and T. P. Chow, "Electrical properties of Ga implanted Si p^+ -n shallow junction fabricated by low-temperature rapid thermal annealing," *IEEE electron device lett.*, vol. 9(11), pp. 594-597, 1988.

92. Y. Hirayama and H. Okamoto, "GaAs/AlGaAs material modifications induced by focused Ga ion beam implantation," *J. Vac. Sci. Technol.*, vol. B 6(3), pp. 1018-1021, 1988.

93. H. Miyake, Y. Yuba, K. Gamo, S. Namba, and T. Shiokawa, "Defects induced by focused ion beam implantation in GaAs," *J. Vac. Sci. Technol.*, vol. B 6(3), pp. 1001-1005, 1988.

94. A. J. Steckl, H. C. Mogul, and S. M. Mogren, "Ultrashallow Si p^+ -n junction fabrication by low energy Ga^+ focused ion beam implantation," *J. Vac. Sci. Technol.*, vol. B 8(6), pp. 1973-1940, 1990.

95. T. Kanayama, H. Hiroshima, and M. Komuro, "Mini-ature hall sensor fabricated with maskless ion implantation," *J. Vac. Sci. Technol.*, vol. B 6(3), pp. 1010-1013, 1988.

96. M. Tamura, S. Shukuri, and Y. Madokoro, "Two-dimensional distribution of secondary defects in focused ion beam implantation into Si," *J. Vac. Sci. Technol.*, vol. B 6(3), pp. 996-1000, 1988.

97. K. B. Kahen, D. L. Peterson, and G. Rajeswaran, "Effects of ion implantation does on the interdiffusion of GaAs-AlGaAs interfaces," *J. Appl. Phys.*, vol. 68(50), pp. 2087-2090, 1990.

98. J. Melngailis, T. O. Herndon, M. Shepard and H. Lezec, "Planar vias through Si_3N_4 fabricated by focused ion beam implantation," *J. Vac. Sci. Technol.*, vol. B 6(3), pp. 1022-1025, 1988.

99. T. Hiramoto, K. Hirakawa, and T. Ikoma, "Fabrication of one-dimensional GaAs wires by focused ion beam implantation," *J. Vac. Sci. Technol.*, vol. B 6(3), pp. 1014-1017, 1988.

100. W. M. Clark, Jr., M. W. Utlaut, R. H. Reuss, and D. Koury, "High-gain lateral pnp biopolar transistors made using focused ion beam implantation," *J. Vac. Sci. Technol.*, vol. B 6(3), pp. 1006-1009, 1988.

101. A. Fujiwara, "Calculation of thickness distribution for ion beam sputter deposition," *J. Vac. Sci. Technol.*, vol. A 9(1), pp. 141-144, 1991.

102. T. Tao, W. Wilkinson, and J. Melngailis, "Focused ion beam induced deposition of platinum for repair processes," *J. Vac. Sci. Technol.*, vol. B 9(1), pp. 162-164, 1991.

103. A. Gandhi and J. Orlff, "Parametric modeling of focused ion beam induced etching," *J. Vac. Sci. Technol.*, vol. B 8(6), pp. 1814-1819, 1990.

104. J. S. Ro, D. Dubner, C. V. Thompson, and J. Melngailis, "Summary Abstract: ion induced deposition of gold films," *J. Vac. Sci. Technol.*, vol. B 6(3), p. 1043, 1988.

105. L. R. Harriott, K. D. Cummings, M. E. Gross, W. L. Brown, J. Linnros, and H. O. Funsten, "Fine line patterning by focused ion beam induced redeposition of palladium aetate films," *Mat. Res. Soc. Symp. Proc.*, vol. 75, pp. 99-105, 1987.

106. Y. Ochiai, K. Gamo, and S. Namba, "Pressure and irradiation angle dependence of maskless ion beam assisted etching of GaAs and Si," *J. Vac. Sci. Technol.*, vol. B 3(1), pp. 67-70, 1985.

107. K. Gamo and S. Namba, "Ion beam assisted etching and deposition," *J. Vac. Sci. Technol.*, vol. B 8(6), pp. 1927-1931, 1990.

108. Z. Xu, K. Gamo, and S. Namba, "Ion beam assisted etching of SiO_2 and Si_3N_4," *J. Vac. Sci. Technol.*, vol. B 6(3), pp. 1039-1042, 1988.

109. T. Tao, J. Ro, J. Melngailis, Z. Xue, and H. D. Kaesez, "Focused ion beam induced deposition of platinum," *J. Vac. Sci. Technol.*, vol. B 8(6), pp. 1826-1829, 1990.

110. D. G. Lishan and E. L. Hu, "Chlorine and HCl radical beam etching of III-V semiconductors," *J. Vac. Sci. Technol.*, vol. B 8(6), pp. 1951-1955, 1990.

111. Z. Nakagawa, S. Sasaki, M. Sato, J. Glanville, and M. Yamamoto, "Summary abstract: recent progress on etching technology with focused ion beam in photomask repair," *J. Vac. Sci. Technol.*, vol. B 6(3), pp. 1030-1031, 1988.

112. G. C. Chi, F. W. Ostermayer, Jr., K. D. Cummings, and L. R. Harriott, "Ion beam damage-induced masking for photoelectrochemical etching of III-V semiconductors," *J. Appl. Phys*, vol. 60(11) 4012-4014, 1986.

113. L. R. Harriott and M. J. Vasile, "Focused ion beam induced deposition of opaque carbon films," *J. Vac. Sci. Technol.*, vol. B 6(3) 1035-1038, 1988.

114. B. Chu, *Laser Light Scattering,* Academic Press, New York, San francisco and London, 1974.

115. N. K. Kang and L. W. Swanson, "Computer simulation of liquid metal ion source optics," *Appl. Phys.*, vol. A 30, pp. 95-104, 1983.

116. D. R. Kingham and L. W. Swanson, "Theoretical investigation of liquid metal ion source: field and temperature dependence of ion emission," *Appl. Phys.*, vol. A 41, pp. 157-169, 1986.

117. L. Zhou, Jr., F. Holmes, and J. Orloff, *Energy distribution measurement of a Ga liquid metal ion source at high frequency by a focused laser beam.* In Press

118. J. D. Jackson, *Classical Electrodynamics,* John Wiley & Sons Inc, New York and London, 1986.

119. W. R. Smythe, *Static And Dynamic Electricity,* McGraw-Hill Book Company, Ner York, St. Louis, San Francisco, Toronto, London and Sydney, 1968.

120. R. E. Collin, *Field Theory of Guided Waves,* McGraw-Hill Book Company, New York, Toronto and London, 1960.

121. G. Arfken, *Mathematical Methods for Physicists,* Academic Press Inc, Orlando, San Diego, New York et al, 1985.

122. A. E. Siegman, *Lasers,* University Science Books, Mill Valley, California, 1986.

123. M. Born and E. Wolf, *Principles of Optics,* Pergamon Press, 1983.

124. G. N. Watson, *A Treatise on The Theory of Bessel Functions,* Cambridge at The University Press, New York, 1966.

125. W. Magnus and F. Oberhettinger, *Formnlas And Theorems for The Functions of Mathematical Physics,* Chelsea Publishing Company, New York, 1949.

126. P. M. Morse and H. Feshbach, *Methods of Theoretical Physics,* McGraw-Hill Book company, New York, Toronto and London, 1953.

127. K. N. Ghia and A. G. Mikhail, "Axisymmetric Stokes flow past cones including the case of the needle," *J. Applied Mechanics,* pp. 569-574, Sep, 1975.

128. U. Ghia, R. T. Davis, and A. G. Mikhail, "Displacement thickness effects on inviscid flow past cones," *J. Applied Mechanics,* pp. 912-918, Dec, 1974.

129. A. Hadidi, *Eigenvalues of dielectric-coated conical structures,* Winnipeg, Manitoba, Canada, 1985. Ph.D Thesis

130. A. Hadidi and M. Hamid, "Electric and dyadic Green's function of boumded regions," *Canadian J. of Phys,* vol. 66, No 3, pp. 249-257, Mar, 1988.

131. A. Hadidi, "Eigenvalues of a dielectric-coated conducting cone," *IEEE Transactions on antennas and propagation*, vol. AP-35, No 3, pp. 299-304, Mar, 1987.

132. A. Hadidi and M. Hamid, "Analysis of a cylindrical cavity resonator with absorbing wall," *Int. J. Electron*, vol. 63, No. 3, pp. 435-442, Sep, 1987.

133. R. D. Amado, K. Stricker-Bauer, and D. A. Sparrow, "Semiclassical method and the summation of the scattering partial wave series," *Phys. Review C*, vol. 32, No.1, pp. 329-332, Jul, 1985.

134. Viktor Szalay, "The overlap integral of associated Legendre functions," *J. of Phys. A*, vol. 23, No. 12, pp. 2689-2694, Jun, 1990.

135. M. L. Laursen and K. Mita, "Some integrals involving associated Legendre functions and Gegenbauer polynomials," *J. of Phys. A*, vol. 14, No. 5, pp. 1065-1068, Mar, 1981.

136. L. D. Salem and H. S. Wio, "Some integrals involving Legendre polynomials and associated Legendre functions," *J. of Phys. A*, vol. 22, No. 20, pp. 4331-4338, Oct, 1989.

137. J. Mathews and R. L. Walker, *Mathematical Method of Phys.,* W. A. Benjamin, New York, 1964.

138. W. D. Ross, "Computation of Bessel Functions in Light Scattering Studies," *Applied Optics*, vol. 11 No. 9, p. 1919, Sep, 1972.

139. W. H. Press, B. P. Flannery, S. A. Teukolsky and W. T. Vetterling, *Numerical Recipes,* Cambridge University Press, Cambridge, 1986.

140. P. J. Wyatt, "Scattering of Electromagnetic Plane Waves from Inhomogeneous Spherically Symmetric Objects," *Physical Review*, vol. 127, No. 5, pp. 1837-1843, Sep. 1962.

141. K. Jousten, J. F. Holmes and J. Orloff, *High Frequency Modulation of A Gallium Liquid Metal Ion Source Using A Laser Beam And Thermal Effects*, 1990.

APPENDIX A THE DERIVATION OF INCIDENT LASER FIELDS

The L. W. Davis' procedure[1] is used for the following work. His method is considerably easier than that of others. If the electromagnetic vector potential is linearly polarized along one axis, then the nonvanishing component of **A** obeys a scalar wave equation. In the Lorentz gauge, the vector potential equation is:

$$\nabla^2\mathbf{A}+k^2\mathbf{A}=-\mu_0\mathbf{J} \tag{A.1}$$

where $k = \dfrac{2\pi}{\lambda}$. Since the scalar potential is given in terms of the vector potential via the Lorentz condition ,

$$\Phi=\frac{jc}{k}\nabla\cdot\mathbf{A} \tag{A.2}$$

The fields **B** and **E** may be expressed in terms of **A** alone. i.e.,

$$\mathbf{B}=\nabla\times\mathbf{A} \tag{A.3}$$

and

$$\mathbf{E} = -\nabla\Phi - jck\mathbf{A}$$

$$= -\frac{jc}{k}\nabla(\nabla\cdot\mathbf{A}) - jck\mathbf{A} \tag{A.4}$$

1) x direction polarization and y- direction propagating

To describe the laser beam, we assume that **A** is polarized along the **x** axis and the beam propagates along the **y** axis. Using a Cartesian coordinate system, equation (A.1) reduces in empty space to the scalar relation

$$\nabla^2 A + k^2 A = 0 \tag{A.5}$$

where we understand that $A = A_x$ and $A_y = A_z = 0$. Anticipating that the waves are nearly plane, we take

$$A(\mathbf{r}) = \Psi(\mathbf{r})e^{-jky} \tag{A.6}$$

where Ψ is a slowly varying function. Inserting (A.6) into (A.5) gives

$$\nabla^2\Psi - 2jk\frac{\partial\Psi}{\partial y} = 0 \tag{A.7}$$

A Gaussian beam has a width parameter ω_0 at the waist. Consequently the dimensionless variables $x = \omega_0\xi$ and $z = \omega_0\eta$ will be used. There is also a characteristic diffraction or spreading length $l = k\,\omega_0^2$, so we let $y = l\,\zeta$. With these new variables, equation (A.7) becomes:

$$\left(\frac{\partial^2}{\partial\xi^2} + \frac{\partial^2}{\partial\eta^2}\right)\Psi - 2j\frac{\partial\Psi}{\partial\zeta} + s^2\frac{\partial^2\Psi}{\partial\zeta^2} \tag{A.8}$$

where

$$s = \frac{\omega_0}{l} = \frac{1}{k\omega_0} \tag{A.9}$$

Note that so long as the beam waist parameter ω_0 is large compared to λ, then s is small compared to unity. Consequently it is natural to seek a solution of equation (A.8) of the form

$$\Psi = \Psi_0 + s^2\Psi_2 + s^4\Psi_4 + \cdots \tag{A.10}$$

It is seen that the lowest order function Ψ_0 obeys

$$(\frac{\partial^2}{\partial\xi^2}+\frac{\partial^2}{\partial\eta^2})\Psi_0-2j\frac{\partial\Psi_0}{\partial\zeta}=0 \tag{A.11}$$

Equation (A.11) is the starting point of traditional Gaussian beam theory. The fundamental mode solution is well known to be[21] :

$$\Psi_0 = f\ e^{[-j(P+Q\rho^2)]} \tag{A.12}$$

where $Q = 1 / (j + 2 \zeta)$, $j P = - \ln j Q$, $\rho^2=\xi^2+\eta^2$ and f is a arbitrary constant related to the total power in the beam. In the work that follows, we will let $f = 1$ and then adjust it later for arbitrary power.

Now we consider the electric field of the incident laser beam. Since $\mathbf{A}=A\mathbf{i}_0$, one obtains

$$\mathbf{E}=-\frac{jc}{k}\nabla(\frac{\partial A}{\partial x})-jckA\mathbf{i}_0$$

$$=(-\frac{jc}{k}\frac{\partial^2 A}{\partial x^2}-jckA)\mathbf{i}_0-\frac{jc}{k}\frac{\partial^2 A}{\partial y\partial x}\mathbf{j}_0-\frac{jc}{k}\frac{\partial^2 A}{\partial z\partial x}\mathbf{k}_0 \tag{A.13}$$

In terms of the dimensionless variables (ξ,η,ζ), it becomes:

$$\mathbf{E}=-jck\left[(s^2\frac{\partial^2 A}{\partial\xi^2}+A)\mathbf{i}_0+(s^3\frac{\partial^2 A}{\partial\zeta\partial\xi})\mathbf{j}_0+(s^2\frac{\partial^2 A}{\partial\eta\partial\xi})\mathbf{k}_0\right] \tag{A.14}$$

From equation (A.6), i.e.,

$$A(\mathbf{r})=\Psi(\mathbf{r})e^{-jky} \tag{A.15}$$

and

$$\Psi=\Psi_0+s^2\Psi_2+\cdots \tag{A.16}$$

Substituting (A.15) and (A.16) into (A.14), we get:

$$\mathbf{E}=-jcke^{-jky}\left\{\left[\Psi_0+s^2\Psi_2+s^2\frac{\partial^2\Psi_0}{\partial\xi^2}+\cdots\right]\mathbf{i}_0\right.$$

$$\left.+\left[s^3\frac{\partial^2\Psi_0}{\partial\zeta\partial\xi}-js\frac{\partial\Psi_0}{\partial\xi}+\cdots\right]\mathbf{j}_0+s^2\left(\frac{\partial^2\Psi_0}{\partial\eta\partial\xi}+\ldots\right)\mathbf{k}_0\right\} \tag{A.17}$$

Now, taking the lowest orders of s, the components of $\mathbf{E}$ are:

$$E_x=-jk\Psi_0e^{-jky} \tag{A.18}$$

$$E_y=-\frac{2Qx}{l}E_x \tag{A.19}$$

$$E_z=0 \tag{A.20}$$

Now, let us go back to equation (A.3)

$$\mathbf{B}=\nabla\times\mathbf{A} \tag{A.21}$$

The magnetic fields of the incident laser can be derivated from it. Since

$$\mathbf{B}=\nabla\times\mathbf{A}$$

$$=\left(\frac{\partial A_z}{\partial y}-\frac{\partial A_y}{\partial z}\right)\mathbf{i}_0-\left(\frac{\partial A_z}{\partial x}-\frac{\partial A_x}{\partial z}\right)\mathbf{j}_0+\left(\frac{\partial A_y}{\partial x}-\frac{\partial A_x}{\partial y}\right)\mathbf{k}_0 \tag{A.22}$$

Since we assumed that $A = A_x$, $A_y=A_z=0$, equation (A.22) is:

$$\mathbf{B}=\frac{\partial A_x}{\partial z}\mathbf{j}_0-\frac{\partial A_x}{\partial y}\mathbf{k}_0 \tag{A.23}$$

It means that:

$$B_x=0 \tag{A.24}$$

$$B_y=\frac{\partial A_x}{\partial z} \tag{A.25}$$

and

$$B_z=-\frac{\partial A_x}{\partial y} \tag{A.26}$$

According to (A.15), $A = \Psi e^{-jky}$ and (A.16) $\Psi=\Psi_0+s^2\Psi_2 + \ldots$, Substituting them into equation (A.25) and (A.26), yield:

$$B_y = \frac{\partial}{\partial z}\left[(\Psi_0 + s^2\Psi_2 + \cdots)e^{-jky}\right] \tag{A.27}$$

$$B_z = -\frac{\partial}{\partial y}\left[(\Psi_0 + s^2\Psi_2 + \cdots)e^{-jky}\right] \tag{A.28}$$

Taking the lowest term of s , we have:

$$B_y = \frac{\partial}{\partial z}\Psi_0 e^{-jky} \tag{A.29}$$

$$B_z = -\frac{\partial}{\partial y}\Psi_0 e^{-jky} \tag{A.30}$$

Since we have had:

$$\Psi_0 = e^{-j(P+Q\rho^2)} \tag{A.31}$$

Substituting Ψ_0 into (A.29) and (A.30), we get:

$$B_y = \frac{1}{\omega_0}\frac{\partial}{\partial \eta}\left[e^{-j(P+Q\rho^2)}e^{-jky}\right]$$

$$= -\frac{2Qz}{l}jk\Psi_0 e^{-jky} \tag{A.32}$$

$$B_z = -\frac{1}{l}\frac{\partial}{\partial \zeta}\left[e^{-j(P+Q\rho^2)}e^{-jky}\right]$$

$$=\frac{j}{l}\Psi_0 e^{-jky}(\frac{dP}{d\zeta}+\frac{dQ}{d\zeta}\rho^2+kl) \tag{A.33}$$

Since our approximation is only concerned about the s^0 so that we know that both $\frac{dP}{d\zeta}$ and $\frac{dQ}{d\zeta}$ can be neglected. Thus, we have:

$$B_z=jk\Psi_0 e^{-jky} \tag{A.34}$$

Considering $B = \mu H$ and $c = (\epsilon\mu)^{-1/2}$, equations (A.24), (A.33) and (A.34) can be expressed as:

$$H_x=0 \tag{A.35}$$

$$H_y=-\frac{2Qz}{l}H_z \tag{A.36}$$

$$H_z=\sqrt{\epsilon/\mu}E_x \tag{A.37}$$

2) z- direction polarization and y- direction propagating

If we assume that the **A** is along the **z** direction, i.e., $A = A_z$ and $A_x=A_y=0$, taking the plane wave expression (A.6) again, we get

$$\nabla^2\Psi-2jk\frac{\partial\Psi}{\partial y}=0 \qquad (A.38)$$

Let $x = \omega_0\xi$, $z= \omega_0\eta$ and $y=l\zeta$, with these new variables, equation (A.38) becomes :

$$(\frac{\partial^2}{\partial\xi^2}+\frac{\partial^2}{\partial\eta^2})\Psi-2j\frac{\partial\Psi}{\partial\zeta}+s^2\frac{\partial^2\Psi}{\partial\partial\zeta^2}=0 \qquad (A.39)$$

The lowest order function Ψ_0 also obeys:

$$(\frac{\partial^2}{\partial\xi^2}+\frac{\partial^2}{\partial\eta^2})\Psi_0-2j\frac{\partial\Psi_0}{\partial\zeta}=0 \qquad (A.40)$$

Considering the electrical field of the incident laser beam, since $\mathbf{A}=A\mathbf{k_0}$, we get:

$$\mathbf{E}=-jck\left[\frac{1}{k^2}\frac{\partial^2 A}{\partial x\partial z}\mathbf{i_0}+\frac{1}{k^2}\frac{\partial^2 A}{\partial y\partial x}\mathbf{j_0}+(\frac{1}{k^2}\frac{\partial^2 A}{\partial z^2}+A)\mathbf{k_0}\right] \qquad (A.41)$$

In terms of the dimensionless variables (ξ,η,ζ), it becomes:

$$\mathbf{E}=-jck\left[(s^2\frac{\partial^2 A}{\partial\xi\partial\eta})\mathbf{i_0}+(s^3\frac{\partial^2 A}{\partial\zeta\partial\xi})\mathbf{j_0}+(s^2\frac{\partial^2 A}{\partial\eta^2}+A)\mathbf{k_0}\right] \qquad (A.42)$$

Substituting $A(\mathbf{r})=\Psi(\mathbf{r})e^{-jky}$ and $\Psi=\Psi_0+s^2\Psi_2+\cdots$ into (A.42), one obtains:

$$\mathbf{E}=-jcke^{-jky}\left[(s^2\frac{\partial^2\Psi_0}{\partial\xi\partial\eta}+\cdots)\mathbf{i}_0+(s^3\frac{\partial^2\Psi_0}{\partial\zeta\partial\xi}-js\frac{\partial\Psi_0}{\partial\xi}+\cdots)\mathbf{j}_0\right.$$
$$\left.+(\Psi_0+s^2\Psi_2+s^2\frac{\partial^2\Psi_0}{\partial\eta^2}+\cdots)\mathbf{k}_0\right] \tag{A.43}$$

Again taking the lowest orders of s, the components of $\mathbf{E}$ are:

$$E_x=0 \tag{A.44}$$

$$E_y=-\frac{2Qz}{l}E_z \tag{A.45}$$

$$E_z=-jk\Psi_0e^{-iky} \tag{A.46}$$

Using equation (A.22), we can derivate the magnetic fields in this situation. i.e.,

$$\mathbf{B}=\frac{\partial A_z}{\partial y}\mathbf{i}_0-\frac{\partial A_z}{\partial x}\mathbf{j}_0 \tag{A.47}$$

It means that:

$$B_x = \frac{\partial A_z}{\partial y} \tag{A.48}$$

$$B_y = -\frac{\partial A_z}{\partial x} \tag{A.49}$$

and

$$B_z = 0 \tag{A.50}$$

Putting equations (A.15) and (A.16) into (A.48) and (A.49), we get:

$$B_x = \frac{\partial}{\partial y}\Psi_0 e^{-jky} \tag{A.51}$$

$$B_y = -\frac{\partial}{\partial x}\Psi_0 e^{-jky} \tag{A.52}$$

Since we have known Ψ_0 from equation (A.12), substitute it into (A.51) and (A.52) so that

$$B_x = \frac{1}{l}\frac{\partial}{\partial \zeta}\left[e^{-j(P+Q\rho^2)}e^{-jkl\zeta}\right]$$

$$= -j\Psi_0 k e^{-jky} \tag{A.53}$$

$$B_y = \frac{1}{\omega}\frac{\partial}{\partial \xi}\left[e^{-j(P+Q\rho^2)}e^{-jkl\zeta}\right]$$

$$=-\frac{2Qx}{l}jk\Psi_0 e^{-jky} \tag{A.54}$$

Considering $B = \mu H$ and $c = (\epsilon\mu)^{-1/2}$, the equations (A.53), (A.54) and (A.50) can be written as:

$$H_x=\sqrt{\epsilon/\mu}E_z \tag{A.55}$$

$$H_y=-\frac{2Qx}{l}H_x \tag{A.56}$$

$$H_z=0 \tag{A.57}$$

3) Relation to total laser power

In order for the equation for the beam wave fields to be useful, they should be in terms of the total power in the laser beam. As was proposed earlier,

this can be accomplished by adjusting the constant in front of Ψ_0 . For the **z** polarization case,

$$E_x=0 \tag{A.58}$$

$$H_z=0 \tag{A.59}$$

The total power in the beam wave is then given by

$$TP=\iint_{surface}\mathbf{S}\cdot\hat{\mathbf{n}}da \tag{A.60}$$

where **S** is the Poynting vector given by

$$\mathbf{S}=\frac{1}{2}\mathrm{Re}(\mathbf{E}\times\mathbf{H}^*) \tag{A.61}$$

The surface that we will use for the integration is the X-Z plane and $\hat{n}$ $= \mathbf{j_0}$.

Therefor,

$$\mathbf{S}\cdot\hat{\mathbf{n}}=\mathbf{S}\cdot\mathbf{j}_0=E_zH_x^*=(\epsilon/\mu)^{1/2}E_zE_z^* \tag{A.62}$$

Using equations (A.46) and (A.55) in (A.62) and since y = 0

$$\mathbf{S}\cdot\hat{\mathbf{n}}=(\epsilon/\mu)^{1/2}c^2k^2f^2e^{-\frac{2(x^2+z^2)}{\omega_0^2}} \tag{A.63}$$

where the arbitrary constant f has been selected to account for arbitrary laser power. The total power then is given by:

$$\begin{aligned}TP&=\frac{c^2k^2f^2}{z_0}\int_{-\infty}^{\infty}\int_{-\infty}^{\infty}dxdze^{-\frac{2(x^2+z^2)}{\omega_0^2}}\\&=\frac{\pi c^2k^2f^2\omega_0^2}{4z_0}\end{aligned} \tag{A.64}$$

where the characteristic impedance of the medium z_0 is given by

$$z_0 = (\mu/\epsilon)^{1/2} \tag{A.65}$$

For a vacuum, $z_0 = 377$ ohms.

We want f to be chosen such that TP = the total power P in the laser beam. S_0 setting equation (A.64) equal to P, f is given by:

$$f = \frac{2\sqrt{z_0 P}}{ck\omega_0\sqrt{\pi}} \tag{A.66}$$

Consequently, E_z may be expressed as:

$$E_z = -j\frac{2\sqrt{z_0 P}}{\omega_0\sqrt{\pi}}\Psi_0 e^{-jky} \tag{A.67}$$

for the **z** polarized case.

For the **x** polarized case, a similar analysis yields:

$$E_x = -j\frac{2\sqrt{z_0 P}}{\omega_0\sqrt{\pi}}\Psi_0 e^{-jky} \tag{A.68}$$

The rest of the field equations are as derived earlier.

APPENDIX B MAGNETIC FIELD EQUATIONS

In Section "III Theory", we used the incident and scattered electric fields of the laser beam as given by equations (3.48) - (3.53). We would like now to formulate the incident and scattered magnetic fields for the laser beam.

Following the steps in Section III, substituting equations (3.44) -- (3.47) into (3.38), (3.39) and (3.40), we get:

the incident magnetic fields of the laser beam:

$$H_{i,r} = \frac{\partial^2(r\Pi_i^*)}{\partial r^2} + k^2 r\Pi_i^*$$

$$= \frac{1}{r}\sum_q \sum_{n=0}^{\infty} \left[q(q+1)B_{qn} j_q(kr) P_q^n(\cos\theta) e^{jn\phi} \right] \tag{B.1}$$

$$H_{i,\theta} = \frac{j\omega\epsilon}{r\sin\theta}\frac{\partial(r\Pi_i)}{\partial\phi} + \frac{1}{r}\frac{\partial^2(r\Pi_i^*)}{\partial r\partial\theta}$$

$$= -\frac{\omega\epsilon}{r\sin\theta}\sum_p \sum_{m=0}^{\infty} mA_{pm}\ r\ j_p(kr) P_p^m(\cos\theta) e^{jm\phi} +$$

$$\frac{1}{r}\sum_q \sum_{n=0}^{\infty} B_{qn}\left[j_q(kr) + kr j_q'(kr) \right] \frac{dP_q^n(\cos\theta)}{d\theta} e^{jn\phi} \tag{B.2}$$

$$H_{i,\phi}=-\frac{j\omega\epsilon}{r}\frac{\partial(r\Pi_i)}{\partial\theta}+\frac{1}{r\sin\theta}\frac{\partial^2(r\Pi_i^*)}{\partial r\partial\phi}$$

$$=-\frac{j\omega\epsilon}{r}\sum_p\sum_{m=0}^{\infty}A_{pm}\ r\ j_p(kr)\frac{dP_p^m(\cos\theta)}{d\theta}e^{jm\phi}$$

$$+\frac{j}{r}\sum_q\sum_{n=0}^{\infty}nB_{qn}\left[j_q(kr)+krj_q^{'}(kr)\right]\frac{P_q^n(\cos\theta)}{\sin\theta}e^{jn\phi} \tag{B.3}$$

the scattered magnetic fields of laser beam:

$$H_{s,r}=\frac{\partial^2(r\Pi_s^*)}{\partial r^2}+k^2r\Pi_s^*$$

$$=\frac{1}{r}\sum_q\sum_{n=0}^{\infty}\left[q(q+1)b_{qn}h_q^{(2)}(kr)P_q^n(\cos\theta)e^{jn\phi}\right] \tag{B.4}$$

$$H_{s,\theta}=\frac{j\omega\epsilon}{r\sin\theta}\frac{\partial(r\Pi_s)}{\partial\phi}+\frac{1}{r}\frac{\partial^2(r\Pi_s^*)}{\partial r\partial\theta}$$

$$=-\frac{\epsilon\omega}{r\sin\theta}\sum_p\sum_{m=0}^{\infty}ma_{pm}\ r\ h_p^{(2)}(kr)P_p^m(\cos\theta)e^{jm\phi}+$$

$$\frac{1}{r}\sum_q\sum_{n=0}^{\infty}b_{qn}\left[h_q^{(2)}(kr)+krh_q^{(2)'}(kr)\right]\frac{dP_q^n(\cos\theta)}{d\theta}e^{jn\phi} \tag{B.5}$$

$$H_{s,\phi}=-\frac{j\omega\epsilon}{r}\frac{\partial(r\Pi_s)}{\partial\theta}+\frac{1}{r\sin\theta}\frac{\partial^2(r\Pi_s^*)}{\partial r\partial\phi}$$

$$=-\frac{j\omega\epsilon}{r}\sum_{p}\sum_{m=0}^{\infty}a_{pm}\ r\ h_p^{(2)}(kr)\frac{dP_p^m(\cos\theta)}{d\theta}e^{jm\phi}+$$

$$\frac{j}{r}\sum_{q}\sum_{n=0}^{\infty}nb_{qn}\left[h_q^{(2)}(kr)+krh_q^{(2)'}(kr)\right]\frac{P_q^n(\cos\theta)}{\sin\theta}e^{jn\phi} \qquad (B.6)$$

APPENDIX C THE FIELD EXPANSION AND FINAL SOLUTIONS

In this section we will discuss two parts of our work. First we would like to show that the spherical harmonic expansion of the incident laser field matches the original field distribution. Secondly we will verify that our final solutions satisfy the boundary conditions.

1) The Expansion of the Incident Laser Field

Considering we have the incident laser field which is propagating along the y axis and with the electrical field polarized in the **x** direction, the electric fields are given by:

$$E_x = -jk\Psi_0 e^{-jky} \tag{C.1}$$

$$E_y = -\frac{2Qx}{l} E_x \tag{C.2}$$

$$E_z = 0 \tag{C.3}$$

where $Q = 1/(j + 2\zeta)$; $\zeta = y/l$; $\Psi_0 = j\,Q\,\exp(-j\,Q\,\rho^2)$; $\rho^2 = (x^2+z^2)/\omega_0^2$; ω_0 is the waist of the beam, k is the wave number and $l = k\,\omega_0^2$.

Theoretically, the incident laser field is:

$$\mathbf{E}_{i,1}=E_x\mathbf{i}+E_y\mathbf{j}+\mathbf{E}_z\mathbf{k} \tag{C.4}$$

or

$$|\mathbf{E}_{i,1}|=\sqrt{E_x^2+E_y^2+E_z^2} \tag{C.5}$$

In Chapter 3, we have expanded and expressed the incident laser field in spherical coordinate system as:

$$E_r=\frac{1}{r}\sum_p\sum_{m=0}^{\infty}\left[p(p+1)A_{pm}j_p(kr)P_p^m(\cos\theta)e^{jm\phi}\right] \tag{C.6}$$

$$E_\theta=\frac{1}{r}\sum_p\sum_{m=0}^{\infty}A_{pm}\left[j_p(kr)+krj_p^{'}(kr)\right]\frac{dP_p^m(\cos\theta)}{d\theta}e^{jm\phi}$$

$$+\frac{1}{r}\sum_q\sum_{n=0}^{\infty}\frac{n\omega\mu}{\sin\theta}B_{qn}\ r\ j_q(kr)P_q^n(\cos\theta)e^{jn\phi} \tag{C.7}$$

and

$$E_\phi=\frac{1}{r}\sum_p\sum_{m=0}^{\infty}jmA_{pm}\left[j_p(kr)+krj_p^{'}(kr)\right]\frac{P_p^m(\cos\theta)}{\sin\theta}e^{jm\phi}$$

$$+\frac{1}{r}\sum_q\sum_{n=0}^{\infty}j\omega\mu B_{qn}\ r\ j_q(kr)\frac{dP_q^n(\cos\theta)}{d\theta}e^{jn\phi} \tag{C.8}$$

So we have

$$\mathbf{E}_{i,2}=E_r\mathbf{r}_0+E_\theta\boldsymbol{\theta}_0+E_\phi\boldsymbol{\phi}_0 \tag{C.9}$$

And

$$|\mathbf{E}_{i,2}|=\sqrt{E_r^2+E_\theta^2+E_\phi^2} \tag{C.10}$$

For the purpose of proving that the harmonic approximate expansion $E_{i,2}$ has the same value as its theoretical one $E_{i,1}$, we only need to substitute appropriate values into equations (C.5) and (C.10) then compute them numerically to get the distribution of the fields and compare their va

According to equations (C.5) and (C.10) and using the parameters in Table C.1 , we computed the incident fields (Figure C.1) following.

From equation (C.5), we have:

$$|\mathbf{E}_{i,1}|=\sqrt{E_x^2+E_y^2+E_z^2}$$

$$=E_x\times\sqrt{1+(2Qx/l)^2}$$

$$=k^2\Psi_0\Psi_0^*\times\sqrt{1+4x^2\ Q\ Q^*/l^2}$$

$$=k^2e^{-2\rho^2}\times\sqrt{1+4x^2/k^2\omega_0^4}$$

Table C.1

Parameters used in numerical evaluation of the field

the half angle of the cone	$\alpha = 45^{\circ}$
the diameter of the sphere	$a = 0.02$ micron
the wavelength of the laser beam	$\lambda = 0.5$ micron
the waist of the focused laser beam	$\omega_0 = 2$ micron
$\theta = 90^{\circ}$;	$\phi = 0^{\circ}$ and 180°

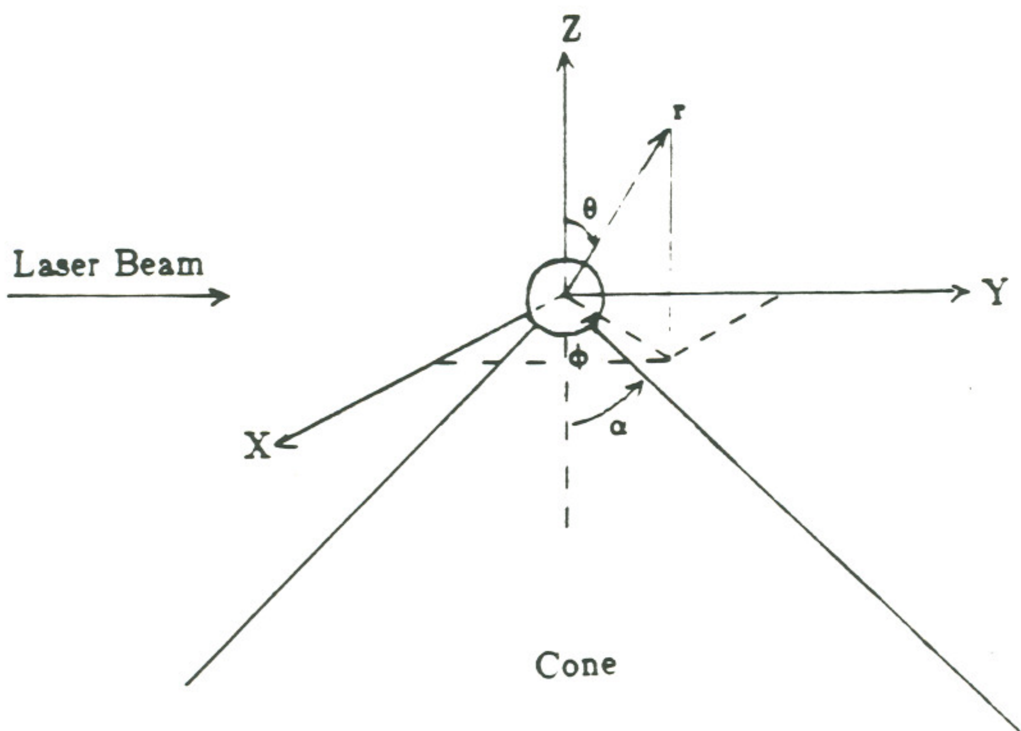

$$=\frac{4\pi}{\lambda^2\omega_0}\sqrt{\pi^2\omega_0^2+\lambda^2x^2}\,\exp[-\frac{2(x^2+z^2)}{\omega_0^2}] \tag{C.11}$$

This is a Gaussian function and its values versus distance are illustrated in Table C.2 .

From equation (C.10), we have:

$$|\mathbf{E}_{i,2}| = \sqrt{E_r^2+E_\theta^2+E_\phi^2} \tag{C.12}$$

Substituting (C.6), (C.7) and (C.8) into (C.12), as computed in Chapter 4, taking enough p's and m's, we can numerically get it result. The changed values of $E_{i,2}$ versus distance r are listed in Table C.3 .

According to Table C.2 and C.3, we drew a graph which described the relations between the incident field E_i and distance r. In this graph (Figure C.2), we can see that the expanded incident field matches its theoretical one very well. It means that our expanding work is successful.

Table C.2

The Changes of Two Fields along Distances

Theory		Approximation	
r (μ m)	$E_{i,1}$ (V/ μ m)	r (μ m)	$E_{i,2}$ (V/ μ m)
-2.0	0.289	-2.0	0.207
-1.8	0.423	-1.8	0.422
-1.6	0.594	-1.6	0.505
-1.4	0.802	-1.4	0.801
-1.2	1.040	-1.2	1.032
-1.0	1.296	-1.0	1.250
-0.8	1.552	-0.8	1.552
-0.6	1.785	-0.6	1.773
-0.4	1.973	-0.4	1.973
-0.2	2.095	-0.2	2.066
0.0	2.173	0.0	2.173
+0.2	2.095	+0.2	2.066
+0.4	1.973	+0.4	1.973
+0.6	1.785	+0.6	1.773
+0.8	1.552	+0.8	1.552
+1.0	1.296	+1.0	1.250
+1.2	1.040	+1.2	1.032
+1.4	0.802	+1.4	0.801
+1.6	0.594	+1.6	0.505
+1.8	0.423	+1.8	0.422
+2.0	0.289	+2.0	0.207

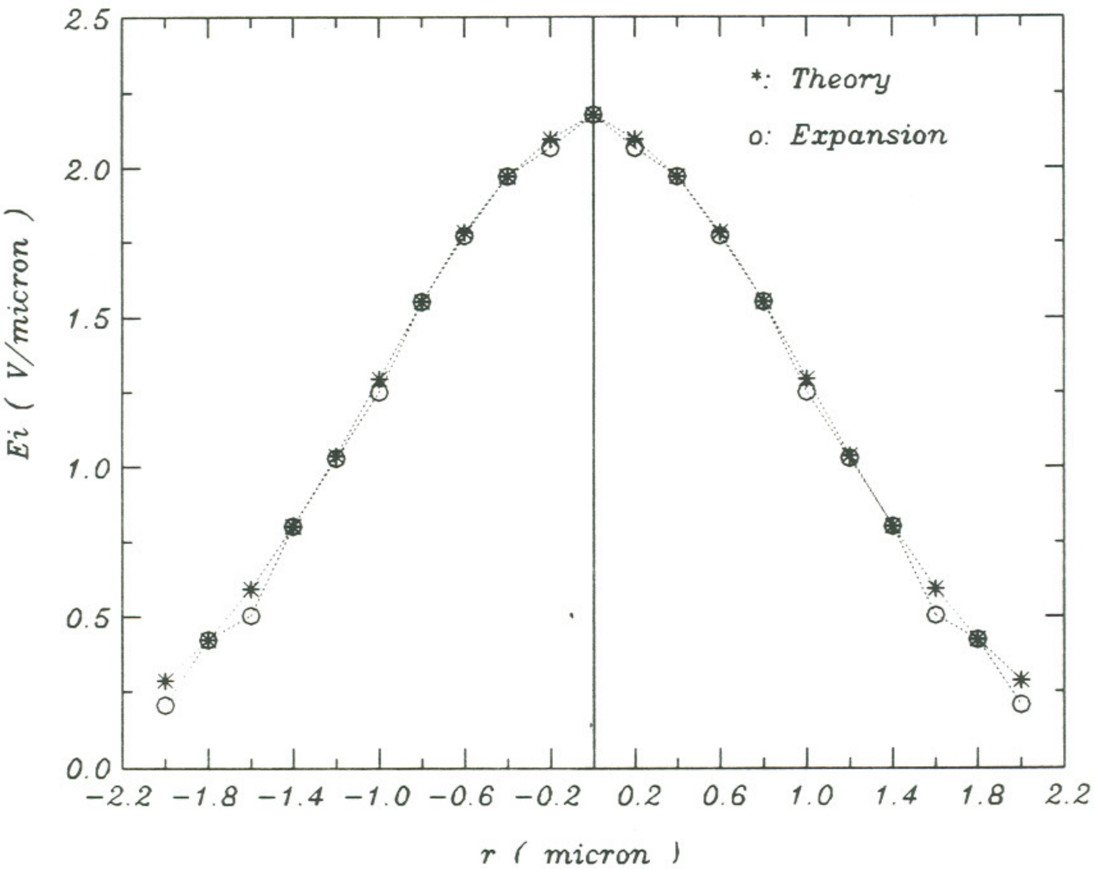

Figure C.2 The distribution of the incident laser fields

both theory and approximation

2) The Final Solutions Satisfy the boundary conditions

We would like to verify that our final solutions are satisfying the boundary conditions. In Chapter 3, we gave the boundary conditions in equations (3.44), (3.45), (3.46) and (3.47). They are:

$$\Pi\,|_{\theta=\theta_0}=0 \tag{C.13}$$

$$\frac{\partial}{\partial r}(r\Pi)\,|_{r=a}=0 \tag{C.14}$$

$$\Pi^*\,|_{r=a}=0 \tag{C.15}$$

$$\frac{\partial \Pi^*}{\partial \theta}\,|_{\theta=\theta_0}=0 \tag{C.16}$$

where

$$\Pi=\sum_{p}\sum_{m=0}^{\infty}\left[A_{pm}j_p(kr)+a_{pm}h_p^{(2)}(kr)\right]P_p^m(\cos\theta)e^{jm\phi} \tag{C.17}$$

and

$$\Pi^*=\sum_{q}\sum_{n=0}^{\infty}\left[B_{qn}j_q(kr)+b_{qn}h_q^{(2)}(kr)\right]P_q^n(\cos\theta)e^{jn\phi} \tag{C.18}$$

The final solutions were given in equations (4.7), (4.8) and (4.9) in Chapter 4. They are:

$$E_r = E_{i,r} + E_{s,r}$$

$$= \frac{1}{r}\sum_{p_k} p_k(p_k+1)\sum_{m}\left[A_{p_k m} j_{p_k}(kr) + a_{p_k m} h_{p_k}^{(2)}(kr)\right] P_{p_k}^{m}(\cos\theta) e^{jm\phi} \qquad (C.19)$$

$$E_\theta = E_{i,\theta} + E_{s,\theta}$$

$$= \frac{1}{r}\sum_{p_k}\sum_{m}\left\{A_{p_k m}\left[j_{p_k}(kr) + kr j_{p_k}'(kr)\right] + a_{p_k m}\left[h_{p_k}^{(2)}(kr) + kr h_{p_k}^{(2)'}(kr)\right]\right\}\frac{dP_{p_k}^{m}(\cos\theta)}{d\theta} e^{jm\phi}$$

$$+\sum_{q_k}\sum_{n}\frac{n\omega\mu}{\sin\theta}\left[B_{q_k n} j_{q_k n}(kr) + b_{q_k n} h_{q_n}^{(2)}(kr)\right] P_{q_k}^{n}(\cos\theta) e^{jn\phi} \qquad (C.20)$$

$$E_\phi = E_{i,\phi} + E_{s,\phi}$$

$$= \frac{j}{r}\sum_{p_k}\sum_{m} m\left\{A_{p_k m}\left[j_{p_k}(kr) + kr j_{p_k}'(kr)\right] + a_{p_k m}\left[h_{p_k}^{(2)}(kr) + kr h_{p_k}^{(2)'}(kr)\right]\right\}\frac{P_{p_k}^{m}(\cos\theta)}{\sin\theta} e^{jm\phi}$$

$$+ j\omega\mu\sum_{q_k}\sum_{n}\left[B_{q_k n} j_{q_k}(kr) + b_{q_k n} h_{q_k}^{(2)'}(kr)\right]\frac{dP_{q_k}^{n}(\cos\theta)}{d\theta} e^{jn\phi} \qquad (C.21)$$

From equation (C.13) and (C.17), if $\Pi|_{\theta=\theta_0} = 0$, it means that

$$\sum_{p}\sum_{m=0}^{\infty}\left[A_{pm} j_p(kr) + a_{pm} h_p^{(2)}(kr)\right] P_p^{m}(\cos\theta) e^{jm\phi} = 0 \qquad (C.22)$$

Comparing it with (C.19), we get

$$E_r \mid_{\theta=\theta_0} = \Big[E_{i,r} + E_{s,r}\Big]_{\theta=\theta_0} = 0 \tag{C.23}$$

From equation (C.14) and (C.17), if $\frac{\partial}{\partial r}$ (r Π) $\mid_{r=a} = 0$, it leads to

$$\sum_p \sum_m \left\{ A_{pm}\Big[j_p(ka) + ka j_p'(ka)\Big] + a_{pm}\Big[h_p^{(2)}(ka) + ka h_p^{(2)'}(ka)\Big]\right\} \times$$

$$P_p^m(\cos\theta)e^{jm\phi} = 0 \tag{C.24}$$

and in (C.15), the $\Pi^* \mid_{r=a} = 0$ means

$$\sum_q \sum_n \Big[B_{qn} j_q(ka) + b_{qn} h_q^{(2)}(ka)\Big] P_q^n(\cos\theta)e^{jn\phi} = 0 \tag{C.25}$$

Comparing (C.24) and (C.25) with (C.20), we can tell that

$$E_\theta \mid_{r=a} = \Big[E_{i,\theta} + E_{s,\theta}\Big]_{r=a} = 0 \tag{C.26}$$

Finally, from (C.16) and (C.18), since $\frac{\partial \Pi^*}{\partial \theta} \mid_{\theta=\theta_0} = 0$, we can know that

$$-\sin\theta_0\sum_q\sum_n\left[B_{qn}j_q(kr)+b_{qn}h_q^{(2)}(kr)\right]\frac{dP_q^n(\cos\theta_0)}{d\theta}e^{jn\phi}=0 \tag{C.27}$$

Comparing (C.24) and (C.27) with (C.21), we have

$$E_\phi\,|_{\,r=a,\theta=\theta_0}=\left[E_{i,\phi}+E_{s,\phi}\right]_{r=a,\theta=\theta_0}=0 \tag{C.28}$$

The results of equations (C.23), (C.26) and (C.28) proved that our final solutions (C.19), (C.20) and (C.21) are satisfying the boundary conditions.

APPENDIX D THE COMPUTATION OF THE ASSOCIATED LEGENDRE FUNCTION

The associated Legendre function $P_p^m(\cos\theta)$, when p is real and m is a positive integer, can be expressed for $-1<\cos\theta\leq 1$ as[2]:

$$P_p^m(\cos\theta)=H_p^m \sin^m\theta \, F\left(m-p,p+m+1;1+m;\frac{1-\cos\theta}{2}\right) \tag{D.1}$$

where the factor H_p^m is a constant depending on the type of normalization chosen. [3] Here we choose that the normalizing factor for $m = 0$ is $H_p^m = 1$ and for $m\neq 0$ is

$$H_p^m=\frac{\sqrt{2}}{2^m m!}\left[\frac{(p+m)!}{(p-m)!}\right]^{1/2} \tag{D.2}$$

where (p + m)! and (p - m) ! are the factorial functions.

In equation (D.1), F is the hypergeometric function:

$$F(\alpha,\beta;\gamma;x)=1+\frac{\alpha\beta}{1\cdot\gamma}x+\frac{\alpha(\alpha+1)\beta(\beta+1)}{1\cdot 2\cdot\gamma(\gamma+1)}x^2+\cdots \tag{D.3}$$

For the purpose of computing the associated Legendre function $P_p^m(\cos\theta)$, we need to generate the hypergeometric function. Before proceeding, the convergence of this function should be considered. The hypergeometric function F given by (D.3) converges, but not very fast. From this point of view, recursive methods[4] should be used to compute it. In this way, we may easily evaluate the Legendre polynomials. This can be clearly seen in equation (D.4). The bigger the k, the more accurate is $P_p^m(\cos\theta)$ is. So the series can be truncated at any desired degree of accuracy, such as that governed by the word size of the computer.

Using the series expression and recursive methods, the associated Legendre function can be written as[3]:

$$P_p^m(\cos\theta)=\sum_{k=0}^{\infty} A_k(m,p)\left(\frac{1-\cos\theta}{2}\right)^k \tag{D.4}$$

and

$$A_0(m,p)=H_p^m \sin^m\theta \tag{D.5}$$

when for $k > 0$,

$$A_k(m,p)=\frac{(k+m-1)(k+m)-p(p-1)}{k(k+m)}A_{k-1}(m,p) \tag{D.6}$$

By differentiating equation (D.4), we easily get an expression for the derivative of the associated Legendre function:

$$\frac{dP_p^m(\cos\theta)}{d\theta} = \sum_{k=0}^{\infty} A_k(m,p)\left(\frac{1-\cos\theta}{2}\right)^k \left(m\cot\theta + k\cot\frac{\theta}{2}\right) \qquad \text{(D.7)}$$

APPENDIX E

THE DERIVATION OF $\frac{\partial P_p^m(\cos\theta)}{\partial p}$

Expressions for the coefficients $A_{p_k m}$ and $B_{q_k n}$ are given in equations (3.84) and (3.87). Here we would like to derive $\frac{\partial P_p^m(\cos\theta)}{\partial p}$ which can be computed by recursive method.

From Haines' paper[3], we have:

$$P_p^m(\cos\theta)=\sum_{k=0}^{\infty} A_k(m,p)\left(\frac{1-\cos\theta}{2}\right)^k \tag{E.1}$$

where

$$A_0(m,p)=\frac{\sqrt{2}\sin^m\theta}{2^m m!}\left[\frac{(p+m)!}{(p-m)!}\right]^{1/2} \tag{E.2}$$

and

$$A_k(m,p)=\left[\frac{k+m-1}{k}-\frac{p(p+1)}{k(k+m)}\right]A_{k-1} \tag{E.3}$$

so that we can easily tell that

$$\frac{\partial P_p^m(\cos\theta)}{\partial p}=\sum_{k=0}^{\infty}\left(\frac{1-\cos\theta}{2}\right)^k\frac{\partial A_k(m,p)}{\partial p} \tag{E.4}$$

where

$$\frac{\partial A_k(m,p)}{\partial p} = \left[\frac{(k+m-1)}{k} - \frac{p(p+1)}{k(k+m)}\right]\frac{\partial A_{k-1}(m,p)}{\partial p} -$$

$$\frac{2p+1}{k(k+m)} A_{k-1}(m,p) \tag{E.5}$$

Therefore,

$$\frac{\partial A_1}{\partial p} = [m - \frac{p(p+1)}{(1+m)}]\frac{\partial A_0}{\partial p} - \frac{2p+1}{1+m} A_0 \tag{E.6}$$

where, A_0 is given in equation (E.2).

And

$$\frac{\partial A_0}{\partial p} = \frac{1}{2}\frac{\sqrt{2}\sin^m\theta}{2^m m!}\left[\frac{(p-m)!}{(p+m)!}\right]^{½} \times$$

$$\frac{(p-m)!\frac{\partial}{\partial p}[(p+m)!] - (p+m)!\frac{\partial}{\partial p}[(p-m)!]}{[(p-m)!]^2} \tag{E.7}$$

We know that

$$(p \pm m)! = \Gamma(p \pm m + 1) \tag{E.8}$$

and the Γ function has an integral representation

$$\Gamma(z)=\int_0^\infty e^{-t}t^{z-1}dt \tag{E.9}$$

Consequently,

$$\frac{\partial}{\partial p}[(p\pm m)!]=\frac{\partial}{\partial p}\Gamma(p\pm m+1)$$

$$=\frac{\partial}{\partial p}\int_0^\infty e^{-t}t^{p\pm m}dt$$

$$=\int_0^\infty e^{-t}t^{\pm m}\frac{\partial}{\partial p}t^{p}dt$$

$$=\int_0^\infty e^{-t}\ \log(t)\ t^{p\pm m}dt \tag{E.10}$$

This integral can be computed numerically.

Using the above work, $\frac{\partial P_p^m(\cos\theta)}{\partial p}$ and $P_p^m(\cos\theta)$ can be evaluated recursively. That is to say, A_0 and $\frac{\partial A_0}{\partial p}$ can be evaluated using equation (E.2) and (E.7). They can then be used in equation (E.3) with $k = 1$ and (E.6) to determine A_1 and $\frac{\partial A_1}{\partial p}$, which can then be used in equation (E.3) and (E.5) with $k = 2$ to find A_2 and $\frac{\partial A_2}{\partial p}$ etc.

References

1. L. W. Davis, "Theory of Electromagnetic Beams," *Phys Rev.*, vol. A19, p. 1177, 1979.
2. E. W. Hobson, *The Theory of Spherical And Ellipsoidal Harmonics,* Cambridge University Press, New York, 1931.
3. G. V. Haines, "Spherical Cap Harmonic Analysis," *Journal of Geophysical Research,* vol. 90, pp. 2583-2591, American Geophysical Union, Feb 28, 1985.
4. H. M. Macdonald, "Zeroes of The Spherical Harmonics $P_n^m(\mu)$ Considered as a Function of n," *Proc. London Math. Soc.*, vol. 31, pp. 264-278, 1900.

VITA

The author was born in the sixties of the twentieth century, Tianjin, China. She is the daughter of Jun Gao and Zhongmin Li. In 1979, she attended the Department of Physics, Nankai University, China and received the Bachelor Degree in Physics in 1983. After she graduated from Nankai University, she worked in The Optical Instrument Factory No.2, Tianjin, China as an assistant engineer. In 1985, the author was admitted as a graduate student by The Research Institute of Electrical Materials, Tianjin and got her Master Degree in EE in 1987.

The author began her graduate study at the Department of Applied Physics and Electrical Engineering, Oregon Graduate Institute of Science and Technology in September 1987 and completed all requirements for the degree of Ph.D in Physics in October 1991.

She has been married since March 1990 to Ming Li.